On the influence of background including neutrals on the dynamics of 3D scrape-off layer filaments in fusion devices

David Schwörer

A dissertation submitted in fulfilment of the
requirements for the award of
Doctor of Philosophy (Ph.D.)

presented to the

School of Physical Sciences
Faculty of Science and Health
Dublin City University

Supervisors:
Dr. Huw Leggate
Prof. Dr. Miles M. Turner
Prof. Dr. Turlough Downes
Prof. Dr. Fulvio Militello (CCFE, UK)

September 2020

Declaration

I hereby certify that this material, which I now submit for assessment on the programme of study leading to the award of Doctor of Philosophy is entirely my own work, that I have exercised reasonable care to ensure that the work is original, and does not to the best of my knowledge breach any law of copyright, and has not been taken from the work of others save and to the extent that such work has been cited and acknowledged within the text of my work.

Signed

David Schwörer

Student ID: 15210921

Date: September 10, 2020

Contents

List of Figures

List of Symbols

a	aspect ration R/r
A_α	advection contribution for quantity *alpha*
$A_\alpha^{\parallel}$	parallel advection contribution for quantity *alpha*
$A_\alpha^{\perp}$	perpendicular advection contribution for quantity *alpha*
α_{m_n}	neutrals' momentum diffusion
β	ratio between magnetic pressure and plasma pressure
$B = B_0$	magnitude of the magnetic field
B_n	density diffusion
B_α	diffusion for quantity $\alpha = n, \omega, V, \ldots$
B_ϕ	magnetic field contribution in ϕ-direction
B_θ	magnetic field contribution in θ-direction
B_θ	poloidal magnetic field

C_α	curvature drive terms for quantity $\alpha = n, \omega, V, \ldots$
c_s	speed of sound
D^0	diffusion limiter
Δt	time step
δ^*	critical filament size
δ	filament size
δ_n	density perturbation
δ_p	pressure perturbation
$\delta_\perp$	perpendicular filament with
δ_x	filament width in x-direction
δ_y	filament width in y-direction
δ_z	filament length in z-direction
e	electron charge
$e_{i,j}$	i, j-th base vector
ϵ_0	vacuum permetivity
ϵ_{pot}	potential energy
e	electron charge
E	electric field
F	force
F_α	friction contribution
f_l	neutrals loss fraction
f_R	reycling fraction
f_T	plasma target flux
f_{GW}	Greenwald fraction
g	"gravitation" constant
Γ^{CX}	charge exchange rate

Γ^{ion}	ionisation rate
Γ^{rec}	recombination rate
$J = n(V - U)$	current density
J_ω	current contribution in the ω equation
$J_\parallel$	parallel current
$\kappa_\perp$	perpendicular heat transport coefficient
Λ	Coulomb logarithm
λ_D	Debye length
Λ_{div}	divertor collisionality
λ_n	density fallof length
λ_q	power fallof length
$L_\parallel = L$	connection length
L_R	Recycling falloff length
L_x	radial domain size
L_y	binormal domain size
L_z	parallel domain size
m_e	electron mass
m_i	ion mass
m_n	neutrals' momentum
μ_α	diffusion coefficient for quantity α
$\mu = m_i/m_e$	ion-electron mass ratio
μ_{n_n}	neutral diffusion coefficient
μ_ω	viscosity (viscosity diffusion rate)
$\mu_\parallel$	parallel diffusion rate
n_0	upstream, background density
N_α	neutral contribution for quantity α
N_D	plasma parameter

n_n	neutral density
N_n	neutral contribution to plasma density equation
n_p	plasma density
$n = n_e$	electron density
N_ω	neutral contribution to vorticity equation
n_{cut}	cutoff density
$\nu_\parallel$	parallel ion-electron resistivity
n_x	number of grid cells in x-direction
n_y	number of grid cells in y-direction
n_z	number of grid cells in z-direction
ω	vorticity
Ω_i	ion cyclotron frequency
ω_p	plasma frequency
$P_0 = n_0 T_0$	upstream, background plasma pressure
$P_e = T_e \cdot n$	electron pressure
ϕ	electro static potential
Φ_α	electro static potential contribution for quantity α
$\phi_s = -V_f T$	electro static potential at the sheath
P_p	plasma pressure
q	safety factor
$q_\parallel$	parallel heat conductivity
Q_T	heat conductivity contribution to the temperature T equation
r	minor radius
R	major radius

R_c	radius of curvature
ρ	gyro radius
R^{imp}	impurity radiation
σ	cross section
S_R	particle source from recycling
t	time
T	temperature
T_0	upstream, background temperature
T_α	temperature contribution for quantity α
τ	drain time
τ_c	collision time
τ_E	energy confinement time
T_e	electron temperature
T_i	ion temperature
T_n	neutral temperature
T_t	target temperature
t_{peak}	time where the filament reaches peak velocity
U	ion velocit
V	electron velocity
v_E	$E \times B$ velocity
V_f	floating potential
v_n	neutrals' velocity
v_r	radial velocity
$v_{th} = \sqrt{\frac{T}{m}}$	thermal velocity
v_x	velocity in x-direction
v_y	velocity in y-direction
x	radial direction

y	bi-normal direction
z	parallel direction
Z	charge of ion
ζ	parallel decay length of filament perturbation

Vectors are denoted by $\vec{f}$, while the magnitude is denoted by $|\vec{f}| = f$ and its direction $\hat{f}$, such that the quantity itself is $\hat{f}f = \vec{f}$.

Further temperatures are measured in units of energy, such as electron volts (eV). That means that $k = 1$ and will be omitted, i.e. the pressure of plasma is $nkT = nT$.

List of Tables

Acknowledgements

This thesis would not have been possible without the support I have received over the last five years from a vast number of individuals within the fusion community. Primarily I wish to express my gratitude to my supervisors Nick Walkden and Huw Leggate as well as Fulvio Militello, Turlough Downes and Miles M Turner for their enthusiasm, guidance, and for always making time for me. Further I want to thank Benjamin D Dudson for his valuable feedback.

This work has been carried out within the framework of the EUROfusion Consortium and has received funding from the Euratom research and training programme 2014-2018 under grant agreement No 633053 and from the RCUK Energy Programme [grant number EP/P012450/1]. To obtain further information on the data and models underlying this paper please contact PublicationsManager@ukaea.uk. The views and opinions expressed herein do not necessarily reflect those of the European Commission. Simulations in this paper made use of EUROfusion High Performance Computer

(Marconi-Fusion) through EUROfusion as well as the ARCHER UK National Supercomputing service (www.archer.ac.uk) under the Plasma HEC Consortium EPSRC grant number EP/L000237/1 and the Irish Supercomputing service FIONN, operated by ICHEC (ichec.ie).

Lastly I wish to thank my co-students Aoife Sommers and Adam Dempsey for their help and the fruitful discussions we had.

Publications

Peer reviewed publications

Parts of this thesis have been previously published. The following peer reviewed publications are based on the work in this thesis:

- Based on parts of chapter 5: D. Schwörer, N.R. Walkden, H. Leggate, B.D. Dudson, F. Militello, T. Downes, and M.M. Turner. Influence of plasma background including neutrals on scrape-off layer filaments using 3D simulations. *Nuclear Materials and Energy*, 12: 825 – 830, 2017. DOI: 10.1016/J.NME.2017.02.016. `http://www.sciencedirect.com/science/article/pii/S2352179116301648`.

- Based on chapter 5 D. Schwörer, N.R. Walkden, H. Leggate, B.D. Dudson, F. Militello, T. Downes, and M.M. Turner. Influence of plasma background on 3D scrape-off layer filaments. *Plasma Physics and Controlled Fusion*, 61(2):025008, December 2018. DOI: 10.1088/1361-6587/AAE8FE. `https://doi.org/10.1088/1361-6587/aae8fe`.

- Based on chapter 6: D. Schwörer, N.R. Walkden, H. Leggate, B.D. Dudson, F. Militello, T. Downes, and M.M. Turner. On the dynamics of 3D scrape-off layer filaments in detached conditions. *Nuclear Fusion*, submitted

- X. Litaudon et al. . Overview of the JET results in support to ITER. *Nuclear Fusion*, 57(10):102001, 2017. URL `http://stacks.iop.org/0029-5515/57/i=10/a=102001`.

Oral contributions

The following oral contributions have been presented as part of this thesis:

- D. Schwörer et al. "Influence of plasma backgrounds including neutrals on SOL filaments using 3D simulations" at the DPG spring meeting 2017 in Bremen, Germany.

- D. Schwörer et al. "Influence of plasma backgrounds including neutrals on SOL filaments using 3D simulations" at the DPG spring meeting 2018 in Erlangen, Germany.

- D. Schwörer et al. "Filament dynamics with STORM in attached and detached conditions" at the BOUT++ workshop 2018 in York, UK.

- D. Schwörer "import boutcore — BOUT++'s python interface" at the BOUT++ workshop 2018 in York, UK.

- D. Schwörer et al. "Vorticity analysis with boutcore" at the BOUT++ workshop 2019 in Abingdon, UK.

Poster contributions

The following poster have been presented at conferences:

- D. Schwörer et al. "Simulations of 3D SOL filaments in detached conditions" at the DPG spring meeting 2019 in Munich, Germany.
- D. Schwörer et al. "3D scrape-off layer filaments in detached conditions" at the 27$^{\text{th}}$ IAEA FEC conference 2018 in Gandhinagar, India.
- D. Schwörer et al. "Influence of plasma backgrounds including neutrals on SOL filaments using 3D simulations" at the EPS 2017 in Belfast, UK.
- D. Schwörer et al. "Influence of Neutrals on Filaments" at the IOP 2017 in Oxford, UK.
- D. Schwörer et al. "Influence of plasma background including neutrals on 3D scrape-off layer filaments" at the PSI 2016 in Rome, Italy.
- D. Schwörer et al. "Influence of neutral-plasma interactions on 3D scrape-off layer filaments" at the DPG spring meeting 2016 in Hannover, Germany.

Abstract

On the influence of background including neutrals on the dynamics of 3D scrape-off layer filaments in fusion devices

David Schwörer

This thesis investigates the influence of background profiles and neutrals on scrape-off layer (SOL) filaments in fusion devices using 3D simulations. This was achieved by seeding filaments on steady-state background profiles including neutrals. In terms of the filament motion, both direct and indirect interaction between the neutrals and filaments have been studied.

The simulations have been carried out using the STORM module, which is implemented using the BOUT++ library. STORM has been extended to include neutrals, using a new neutrals C++-API which also uses BOUT++. Filaments have been seeded on top of plasma backgrounds with changing plasma density and temperatures. The profiles have been generated by running a reduced set of equations to steady state. The backgrounds cover different regimes, namely low-recycling regime, high recycling as well as detached plasma conditions.

In the attached conditions, the filament's radial velocity increased with increasing target temperature, suggesting that sheath currents and plasma viscosity significantly influence the studied filaments. Interaction with the neutrals reduced the filament's radial velocity, especially in the high temperature and high density conditions.

As detachment was reached, the filament's velocity increased temporarily, as sheath currents were strongly suppressed by the high resistivity, caused by a highly dense, cold plasma in front of the target, before the general decreasing trend is recovered for higher densities. In detached conditions the neutrals had an increased impact on the filament dynamics, and partially replaced sheath currents by friction in the detachment front.

CHAPTER 1

Introduction

1.1 Why Fusion?

One of today's major challenges is the climate crisis of global warming. Global warming may have severe consequences for the future [1–3]. By today, our need for energy is mainly supplied by fossil fuels [4]. Greenhouse gases are the main cause of the current climate crisis. There is a need to produce energy without the by-product of greenhouse gases. One possibility to achieve this is fusion, the process which powers the sun and supplies us with light and heat. If it would be possible to reproduce this reaction on earth in a controlled environment, the energy produced could replace fossil fuels [5].

Alternatives to produce energy without greenhouse gases are fission or renewable energies. However renewable energies are limited. The avail-

ability of renewable energies such as solar or wind cannot be controlled by humans. It would require energy storage, which are challenging to be provide in an economically viable fashion at scale [6].

Solar power, one of the renewable energy sources which deployment strongly increasing in the recent years, uses the surface that is radiated by the sun. While solar panels can be installed on roofs, and otherwise "unused" space, these spaces are limited. Beyond that, solar panels compete with crops or farmland in general.

Fission on the other hand, has additional to the unsolved problem of the long lived, highly active radio active waste, the risk of catastrophic events like the one in Fukushima or Chernobyl [7, 8]. This is not a risk in fusion reactors, as there are only a few grams of fuel in the reactor, unlike in fission reactor where tons of uranium are used [9].

Wide spread use of fission also increases the general availability of enriched uranium. While for an energy producing reaction less enriched uranium is needed, the general availability of enriching technologies and enriching plants will make it easier to produce, and harder to control the production of weapons grade enriched uranium.

Fusion has the potential, assuming that appropriate materials for the irradiated regions are chosen, no long lived radio active waste is produced. Further, fusion requires relatively little space compared to other renewable energy sources, and is thus an attractive energy source for the ever growing energy demand for the ever growing metropolises as well as for industry.

1.2 What is Fusion?

Fusion is the nuclear process where particles fuse and the process results in a heavier particle. The fusion process in the sun fuses 4 hydrogen H^+ ions to a helium He^{2+} ion. The fused ion is in a lower energy state, i.e. the process releases energy, and is the process that heats the sun.

Heavier hydrogen isotopes are easier to fuse, compared to "normal" hydrogen ^1H. The easiest reaction is between deuterium D - a hydrogen isotope with one proton and one neutron, and Tritium T, a hydrogen isotope with one proton and two neutrons. The fusion process of Deuterium and Tritium is

$$D + T \rightarrow {}^4He + n \tag{1.1}$$

which has relatively large cross section at 10 keV [5]. A cross section describes the area orthogonal to the direction of movement of two particle, that they need to be in, in order to undergo fusion. In other words, the area describes how likely it is, for the reaction to happen. The reaction is highly exothermic, releasing 17.59 MeV [10]. Hydrogenic nuclei have, compared to heavier elements, only a single charged proton. Heavier elements have a higher Coulomb repulsion, which requires higher temperatures to overcome this barrier [5]. Compared to conventional fuels such as coal, the energy density is much higher. The energy density of coal is 39.3 kJ/g [11], whereas the energy density of deuterium tritium fuel is

$$\frac{17.59\,\mathrm{MeV}}{(2+3)m_p} = 337\,\mathrm{TJ/g} \tag{1.2}$$

Achieving D-T fusion is relatively straight forward, accelerating one

species in a linear accelerator and shooting them into a gas of the other species results in a few reactions. In order to produce energy, this is not a viable approach, as the energy required to accelerate is higher than the released energy, as the fusion cross section is rather small, thus making fusion reaction unlikely. Thus the goal of fusion research is not to achieve fusion by itself, but to do so in a manner that yields more energy than is needed for heating the matter in the first place.

Since the 1950s, the goal of fusion research is to confine the hot matter sufficiently such that the matter is mostly heated by the energy from the fusion process, which is called ignition [12]. The Lawson criteria describes the requirement for ignition as a product of confinement time τ_E and plasma density n and is further a function of temperature T [13]. For temperatures in the range of 10 to 20 keV this can be approximated by $n\tau_E T > 5 \cdot 10^{21}\,\mathrm{m^{-3}\,s\,keV}$, which is in this form also called the triple product. This simple criteria has been extended, but is still used to measure the progress of fusion research towards ignition [12]. As the triple product is approaching the Lawson criteria, most of the energy loss is replaced by the nuclear fusion process, and the plasma can burn without significant external heating [10].

As matter at the required temperatures is mostly ionised, magnetic fields are used to confine the plasma. As there are no magnetic monopoles, confining the plasma in a spherical shape is not possible, and thus the next most preferable geometry is a torus. There by two concepts are now in the focus of research. The tokamak, from the Russian word Токамáк, confines the plasma in a torus, and at the same time a strong current is driven in the plasma, which significantly improves confinement, compared to the purely toroidal field, as the current produces a poloidal field, which suppresses instabilities. The tokamak will be introduced in more detailed in sec. 1.4.

Another fusion device that is promising is the stellarator [14, 15]. A stellarator, has like the tokamak, a toroidal magnet field that is produced by external magnetic field coils. However, the poloidal field is also created by external magnetic field coils. This has the disadvantage that the field is inherently three dimensional. As no current drive is required, which is in tokamaks, at least in parts, achieved by inducing a current by changing the current in a centre solenoid, the stellarator would allow for a continuous operation.

Due to the complicated 3D geometry, computational models are required to optimise the geometry for various transport mechanism, such as magnetohydrodynamics (MHD) instabilities or neo-classical transport [16, 17]. The tokamak was initially the preferred device, as it is rather straight forward to derive various properties for a tokamak with toroidal symmetry, than for the full 3D geometry of a stellarator. Also neo-classical transport is, due to the toroidal symmetry, lower in tokamaks than stellarators. While stellarators avoid the troublesome instabilities which are caused by the large currents in a tokamak, there has been less research in stellarators, as the initial designs had much larger losses, due to the lack of optimisations. For advanced stellarators, engineering constraints are also a major issue. To achieve the intended magnetic field with sufficient precision, precise construction and assembly of the magnetic coils is required. Both, stellarators and tokamaks, need an improved understanding of edge physics, if they are to be used in power plants [18].

However, harvesting these enormous energies is significantly harder than was anticipated in the early years of fusion research [12]. Since then physical understanding of the involved, non-linear, turbulent transport processes has significantly increased. Sufficiently high temperatures have been achieved

in many fusion devices [12]. During the D-T campaign in Joint European Torus (JET) a fusion power of 16.1 MW has been achieved [19]. The corresponding triple product was around $9 \cdot 10^{20}\,\mathrm{m^{-3}\,s\,keV}$.

1.3 Plasma

Plasma is often considered the fourth state of matter, after solid, fluid and the gas state. A plasma generally consists of three components: electrons, ions and non-ionised, neutral particles. Wesson requires that a plasma is to be almost neutral, as any significant charge separation would result in very large restoring force [10]. Chen defines a plasma as "a quasi neutral gas of charged and neutral particles which exhibits collective behaviour." [20]. The two parts that need to be further defined are the "quasi neutrality" as well as the "collective behaviour".

As the gas consists of charged species, on short length scales, the gas is not neutral. Due to the high conductance, on longer length scales the charge is compensated by the surrounding free charges. The Debye length λ_D is the length scale over which a charge is compensated

$$\lambda_D = \sqrt{\frac{\epsilon_0 T}{n e^2}} \tag{1.3}$$

with ϵ_0 the permittivity in vacuum, T is the temperature, n the density of charged particles and $-e$ the electric charge of an electron. For the gas to be quasi neutral, there need to be enough charged particles within a sphere of radius λ_D. This leads to the definition of the plasma parameter N_D

$$N_D = \frac{4\pi}{3} n \lambda_D^3 \tag{1.4}$$

which is the number of charged particles within a sphere of radius λ_D. With N_D quasi neutrality can be expressed as:

$$N_D \gg 1 \tag{1.5}$$

The collective behaviour is caused by the long-range interaction of charges. In contrast, in uncharged gas, collisions are dominating the behaviour, which are local. For electric forces to be dominating, two conditions must be met. First, the system needs to be large enough. For a system of length L, this can be expressed as:

$$L \gg \lambda_D \tag{1.6}$$

The other requirement is that the plasma frequency ω_p is larger than the inverse collision time τ_c

$$\omega_p \tau_c \gg 1 \tag{1.7}$$

as otherwise local collisions are dominating, and the gas is reasonably well described by gas equations.

Thus the state of a plasma is not only dependent on local quantities such as temperature and density, but also on the system size L. As there is also no phase transition between the gas state and the plasma state, as with increasing temperature, the ionisation degree continuously increases, and dependent on the system size, at some point the above criteria are fulfilled. This means that the plasma state is not really a fourth state of matter, but rather a special case of gas, where electro-dynamic forces are dominating the behaviour, rather than collisions. This does however not

change the fact that plasmas are chaotic in nature, and thus challenging to predict and control. Plasma cannot be modelled with the same set of equations that can be used for gases or fluids, due to the electromagnetic forces of the charged particles.

As plasmas, especially hot ones, are not collisional, i.e. collisions are not occurring often, the particle distribution in velocity space can be highly non-Maxwellian. Additionally, to a Maxwellian or thermal distribution, there can be a significant amount of faster particles, if the time scale over which they are accelerated is shorter than the collisional time scale.

The interaction for the charged species, namely ions and electrons, are consisting of long range electro static and electro dynamic forces, as well as collisions. For the interaction with neutrals, only short ranged collisions are possible. If an electron and ion collide, they can recombine, rather than scatter. For that reaction to become likely and thus to produce a neutral atom, both need to have sufficiently low energies. Neutrals can be ionised, if they collide with some particle, in the process producing an ion and electron. A third reaction that can happen is charge-exchange. Thereby an ion and a neutral collide, and the electron switches from the neutral to ion. As the ions can be much hotter than the neutrals, this can produce energetic neutrals, which are no further influenced by magnetic fields.

Due to the presence of charged particles, plasmas are good conductors. Thus they can easily balance any electrical fields within the plasma. Lightning is a natural example where a plasma is conducting a large current of several kA [21].

1.3.1 Magnetised Plasma

Plasmas are influenced by magnetic fields, due to the presence of charged particles. Without collisions, the charged particles perform a gyro-motion in the direction perpendicular to the magnetic field, while they can travel freely along the magnetic field lines. In this thesis the word perpendicular refers to perpendicular to the magnetic field, and parallel refers to parallel to the magnetic field, unless otherwise specified.

If a particle feels a force $\vec{f}$ in the perpendicular direction, ($\vec{f} \perp \vec{B}$) it gets accelerated in the direction of $\vec{f}$. As it gains velocity, the Lorentz force starts acting on the particle, and applies a force in $q\vec{v} \times \vec{B}$ direction, preventing a further acceleration in the direction of the applied force. Thus the total force is

$$\vec{F} = \vec{f} + q\vec{v} \times \vec{B} \tag{1.8}$$

This can be solved in a homogeneous magnetic field $\vec{B}$ by choosing a coordinate system, where without loss of generality the $\hat{z}$-axis is parallel to $\vec{B}$, then the above equation becomes:

$$F_x = qBv_y + f_x \tag{1.9}$$

$$F_y = -qBv_x + f_y \tag{1.10}$$

$$F_z = f_z \tag{1.11}$$

$$m\dot{v}_x = qBv_y + f_x \tag{1.12}$$

$$m\dot{v}_y = -qBv_x + f_y \tag{1.13}$$

$$m\dot{v}_z = f_z \tag{1.14}$$

where the solution for v_x (v_y) is the real (imaginary) part of

$$v_x + iv_y = C_0 e^{i\omega t} + \frac{if_x - f_y}{\omega} \tag{1.15}$$

with $\omega = \frac{qB}{m}$ the gyro frequency. The motion consists of a harmonic contribution, the gyro motion, and the second part of (1.15) represents a drift motion. A force in $\hat{x}$ direction results in a motion in $\hat{y}$ direction - or in general words the drift motion of a force $\vec{f}$ is given by the drift velocity

$$v_d = \frac{\vec{f} \times \vec{B}}{qB^2} \tag{1.16}$$

as mentioned before, the motion is perpendicular to the applied force. The solution is only valid for static forces, i.e. forces that change much slower than the gyro frequency. If we assume a strong magnetic field, we can neglect the gyro motion, and only retain the drift motion, which results in the model of drift-ordered plasma equations.

In the case of an electric field $\vec{E}$ the electro static force is $q\vec{E}$, and thus the associated drift is

$$v_E = \frac{q\vec{E} \times \vec{B}}{qB^2} = \frac{\vec{E} \times \vec{B}}{B^2} \tag{1.17}$$

and thus independent of the charge. This drift is called the $E \times B$ drift.

The radius of the gyro motion depends on the initial condition, and is a function of the velocity. For the thermal velocity $v_{th} = \sqrt{\frac{T}{m}}$ the gyro-radius is then $\rho = \frac{\sqrt{mT}}{eB}$.

For magnetised plasmas, a parameter that describes the ratio between the pressure of the magnetic field on the plasma, and the plasma pressure,

is called the plasma-β, or just β

$$\beta = \frac{P_p}{P_B} = \frac{nT}{\frac{B^2}{2\mu_0}} \tag{1.18}$$

In fusion research it is often preferable to achieve a high β in the core, as powerful magnets are expensive, and thus increasing the plasma pressure with respected to the applied magnetic fields, increases the produced power per magnetic field cost. In terms of plasma physics, β describes to what extend the plasma is able to influence the magnetic fields. In a low β plasma, the magnetic field can be assumed to be not influenced by the plasma, where as in higher magnetic fields, the plasma can influence the magnetic field.

In magnetised plasma often Bohm units are used [22, 23]. In Bohm units the lengths are normalised to the gyro radius $\rho = \frac{\sqrt{m_i T_0}}{eB_0}$, m_i being the ion mass and e the electron charge. T_0 and B_0 are the "typical" temperature T_0 and magnetic field B_0 of the system studied. Times are normalised to the inverse gyro frequency $\omega_i^{-1} = \frac{m_i}{eB_0}$. This leads to the normalisation of velocities by the speed of sound $c_s = \sqrt{\frac{T_0}{m_i}}$. Temperatures are normalised to the "typical" temperature T_0, potentials to T_0/e. Densities are normalised to a "typical" density n_0. While an appropriate choice of the typical quantities makes the handling of the numbers easier, and may be of advantage for numerical accuracy and efficiency, this does not restrict the general validity of the units to the respective ranges. These normalisations can be used if there are strong differences present in the system.

In the case of a strong magnetic field, it can be beneficial to use a field-aligned coordinate system. Thereby the coordinate system is chosen such that the magnetic field is always parallel to one of the base vectors, e.g.

$\vec{B} \parallel e_z$. Note that this can lead to complicated coordinate systems, if the magnetic field is not homogeneous.

1.3.2 Drift-ordered Plasmas

The drift ordered plasma equations are for magnetised, collisional plasmas. That means that enough collisions are occurring, to have a Maxwellian distribution, but not to many to be not further magnetised. This leads to the assumption that cross-field transport is well described by drifts (1.16).

In the case of a single ion species, it is, due to quasi neutrality, sufficient to evolve either the density of the electrons or the ions. As mentioned before, the charged species can flow freely in the parallel velocity, thus the parallel component of the velocities is evolved. While it is sufficient to evolve one density, both velocities must be evolved, as quasi neutrality does not prevent currents, only the divergence of the currents must vanish.

In the perpendicular direction, rather than evolving the velocities, the drifts are computed. In the above derivation, a single particle picture was used. While the result is still valid in the fluid picture, additional terms can arise, such as the diamagnetic drift, that is a drift in the fluid picture, where no single particle is performing a drift. The drift is of the form

$$v_d^D = -\frac{\nabla p \times \vec{B}}{qnB^2} \tag{1.19}$$

and is caused as there are, within a reference frame, more particles from the higher pressure side than from the lower pressure side.

Another term that is evolved in this model is the vorticity ω. It is used to calculate the electrostatic potential ϕ and is defined as $\omega = \nabla n \nabla_\perp \phi$, i.e. the potential is found by inversion of the vorticity. In the context of fusion

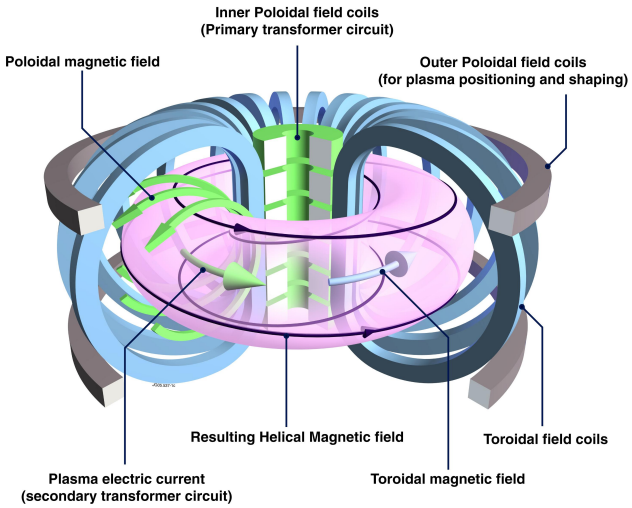

Figure 1.1: Schematic drawing of a tokamak [25, 26], reproduced from Li et al. [27].

devices, the $E \times B$ drift is often the most important drift, thus the vorticity is of especial importance for the cross-field transport in these magnetised plasmas.

As the inversion can be computationally demanding, often the so called Boussinesq approximation is used. Thereby the density dependence of the inversion is removed, i.e. $\omega = \nabla_\perp^2 \phi$.

1.4 Tokamak

A tokamak is a toroidal shaped fusion device that uses magnetic fields to confine plasma, as shown on fig. 1.1. The toroidal magnet field is created by magnetic field coils. Additional to the toroidal field, a weaker, poloidal magnetic field is created by an electric current in the plasma [24]. This twisting of flux tubes is required to achieve good magnetic confinement [10]. The twisting causes to connect region of bad curvature, where perturbations are accelerated outward, with regions of good curvature, where perturbations

are accelerated inward. This stabilises perturbations, and thus reduces radial transport. A tokamak is in first order approximation toroidally symmetric, thus can be solved using 2D domain, and assuming symmetry in the toroidal direction.

The minor radius is the distance from the inner most closed flux surface to the last closed flux surface. The major radius is the distance from the centre of the torus to the inner most closed flux surface [10]. The aspect-ratio a is the ratio of major to minor radius and is an important design parameter for tokamaks [10].

The plasma can be separated into two regions based on magnetic topology, one with closed field lines, and one with open field lines. In the region of closed field lines, the plasma is well confined, and does not interact with any surfaces. The open field lines are not closing on themself, but rather ending on surfaces, where the plasma can interact with the surfaces. The last closed flux surface (LCFS) is also called the separatrix, and is the boundary between the closed field lines and the open field lines [10].

The naïve approach to create the LCFS is to limit the plasma by a material surface, known as a limiter. This however causes to have the hot, confined plasma interact with a material surface. This leads to sputtering, and thus pollutes the plasma [10]. Better confinement is achieved by magnetically separating the hot core from the limiter by pulling out magnetic field lines, that then interact with the wall in a more controlled manner. This creates the LCFS by magnetic topology, rather than by inserting a limiter. This allows for the plasma to be cooled before it interacts with the plasma facing component, thus helps reducing sputtering and improving the life time of the plasma facing components [28].

The schematic cross-section of a tokamak with divertor configuration

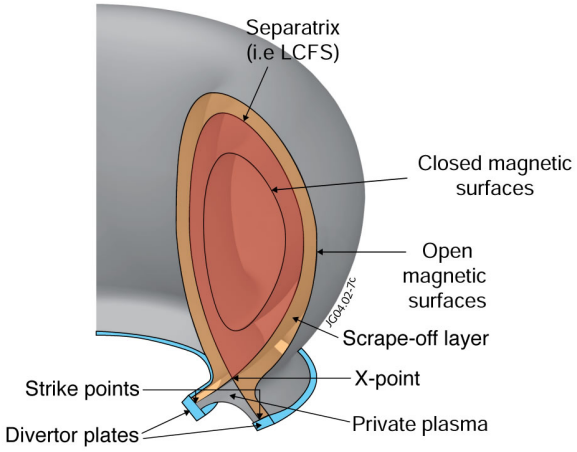

Figure 1.2: Drawing of the edge of a tokamak, reproduced with kind permission from EUROfusion.

is shown in fig. 1.2. In the centre are the closed magnetic flux surfaces, coloured in red. Further outwards follows the LCFS. Going further outward, the field lines end on material surfaces and are therefore called open magnetic field lines. The region outside of the LCFS is called scrape-off layer (SOL), which is discussed in more detail in sec. 1.5.

In the centre is where the fusion reaction is happening, and thus temperatures around 10 keV are required. The plasma at the edge of the confined region within the LCFS is already significantly colder, below 1 keV.

In this case the divertor is at the bottom, where the open magnetic field lines are pulled outwards, towards the divertor tiles. There the plasma interacts in a controlled manner with the plasma facing components. The divertor tiles of fusion devices are expected to handle high heat and particle loads. As the plasma flows from the LCFS towards the divertor tiles, the plasma can be cooled, e.g. by introducing additional neutral impurities to increase radiation of the plasma. A result of the pulled out, diverted magnetic field is the X-point. At the X-point the poloidal magnetic field

vanishes, and only a toroidal component remains. Below the X-point is the private plasma region, which is only fuelled by the SOL.

1.5 Scrape-off layer

As shown in fig. 1.2 the Scrape-off layer (SOL) is outside of the core plasma and is magnetically connected to the divertor. The SOL is fuelled and heated by cross field transport from the hot core plasma. On the outside is the first wall, which protects the vacuum vessel from the plasma. Most of the heat from the core is flowing from the separatrix towards the target.

In recent years the focus has been shifted towards the edge of the plasma. Not only is it necessary to reduce the heat fluxes onto the plasma facing components to extend their life times to reduce maintenance down times [29], but also the plasma material interaction is causing sputtering, which introduces unwanted impurities in the core [30]. These impurities dilute the fuel which reduces the fusion yield. Additionally, heavy elements such as tungsten can significantly cool the plasma through radiation, as such tungsten accumulation in the core can lead to radiation collapse of the plasma.

After the plasma crosses the LCFS and enters the SOL, the plasma flows along the magnetic field lines towards the target. As the plasma hits the target, the ions and electrons can recombine. Most of the ions are "recycled" as neutrals into the vessel. In addition to the parallel transport, along the magnetic fields, a part of the plasma is transported across the field lines. While the parallel transport along the magnetic field lines is much faster, the plasma facing components are much closer in the radial direction than in the parallel direction, thus the perpendicular transport

needs to be considered. A significant amount of the cross field transport in the SOL is caused by filamentary transport [31]. Filaments are magnetically aligned non-linear pressure perturbation, that are observed in most magnetised plasmas [32]. A detailed introduction to filaments is given in chapter 2. The cross field-transport is often approximated with a perpendicular diffusion constant [33]. This yields an exponential decaying profile, however measured profiles deviate from this trend [34, 35]. This is as the transport is non-diffusive and the SOL profiles are not purely exponentially, as described in sec. 2.1.2. Filamentary transport is proposed to explain this [36, 37].

1.5.1 Divertor

The divertor concept allows one to increase the control of the plasma-surface interaction. As the hot plasma is separated from the surface, the plasma can be cooled. Additionally, the separation can reduce the amount of impurities that are generated from sputtering that get into the confined plasma.

The reduced amount of impurities allowed the discovery of H-mode [38, 39]. H-mode is a regime of increased confinement, in contrast to L-mode. In H-mode a pedestal forms at the edge of the core region, which features strong temperature and strong density gradients, which is enabled by a reduction of turbulence as well as the presence of strong shear. The strong gradients enable higher pressure in the core, which thus allows an increased fusion gain, and is thus the envisioned operational regime of ITER (latin for "the way", previously International Thermonuclear Experimental Reactor). While not strictly necessary for H-mode, H-mode is often associated with the presence of a divertor configuration [40].

A divertor does allow a reduction of the heat flux that reaches the tar-

get. It also allows one to spread the heat flux. The expected fusion power of ITER is 500 MW, of which 400 MW will be leaving the plasma in the form of energetic neutrons, as they are neutral particles and thus not influenced by the magnetic field. The major radius of ITER is around $R \approx 6.2\,\mathrm{m}$. For a strike-line width of $\lambda \approx 6\,\mathrm{mm}$, [41] this makes $P/(4\pi R\lambda) \approx 200\,\mathrm{MW/m^2}$, while material limits are around $10\,\mathrm{MW/m^2}$. To reduce the heat flux, essentially two options are possible, either increase the surface, or decrease the power. The wetting area can be increased by expanding the magnetic field lines. To achieve lower power, a part of the power can be radiated. Neutrals can interact with the plasma, and radiate significant amounts of power. This will be discussed in the following sections.

The target tiles typically consist of tungsten or carbon. Tungsten has a low sputtering yield, as well as a high melting temperature. However, as a tungsten atom has $Z = 74$ electrons and the binding energy of the innermost electron roughly scales as Z^2, tungsten is even at temperatures around 10 keV an efficient radiator, and thus can significantly degrade the core confinement. The reason for this is that the bounded electrons can be excited by collisions, and as they relax to the ground state radiate the energy in the form of an photon, which can leave the confinement. This is less of an issue with carbon, as it has only 6 electrons, it is much easier to fully ionise, and thus less of an issue for the confinement. It also has a high thermal conductance, as well as low sputtering yield. It can however form chemical bonds with hydrogen, which thus can significantly increase tritium retention, which is the major reason the the divertor in ITER is made from tungsten [30].

As the plasma hits the target, various processes are happening on the microscopic scale, such as adsorption. Independent of the exact process,

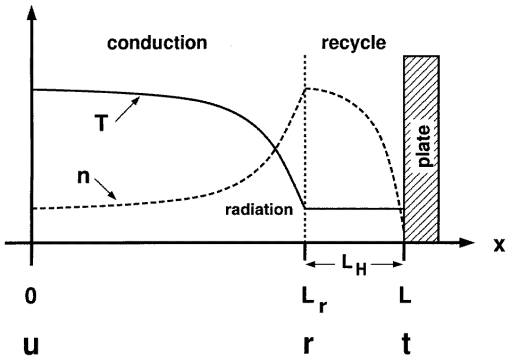

Figure 1.3: Schematic illustration of the two-point model. Taken from Pitcher and Stangeby [42].

most ions get neutralised and re-emitted, and are thus moving back into the plasma. This process is called recycling.

Two-point model

The two point model [42, 43] consists of three equations, that describe the relation between plasma values in the upstream SOL and the plasma conditions at the sheath. This analytical treatment assumes that energy and particles flow from the upstream area down towards the divertor. It includes sinks for particles, energy and momentum as the plasma flows along the magnetic field lines, but does not quantifies these sinks, i.e. they are input quantities in the two-point model. As shown in fig. 1.3, the two-point model separates the flux tube in two regions. The length of the recycling area is in reality significantly smaller than shown in the figure. The shown temperature is assuming equal ion and electron temperature $T_i = T_e$. The model assumes in the conduction region a Spitzer conductivity:

$$q = -\kappa_0 T^{2.5} \frac{\mathrm{d}T}{\mathrm{d}z} \tag{1.20}$$

where z is the length along the magnetic flux tube and

$$\kappa_0 = \frac{(4\pi\epsilon_0)^2}{m_e^{0.5} \ln \Lambda e^4 Z} \tag{1.21}$$

with ϵ_0 the permittivity of vacuum, m_e the mass of an electron, its charge e. $\ln \Lambda \approx 15$ is the Coulomb logarithm and Z is the effective charge, here assumed to be unity.

The two-point model assumes further that all the energy enters the SOL at the symmetry point. Equation (1.20) can then be integrated, to yield

$$T_u^{7/2} = T_r^{7/2} + \frac{7 q_u L_r}{2\kappa_0} \tag{1.22}$$

As the temperature is incorporated as to the power of $\frac{7}{2}$ the dependence on the length of the flux tube is only weak. Whether the energy actually all enters at a single point, or is extended has only a minor influence on this expression.

The heat-flux into the target is assumed to be

$$q_t = q_K + q_P = n_t c_{s,t} \gamma T_t + n_t c_{s,t} \epsilon_{\text{pot}} \tag{1.23}$$

where $\gamma \approx 7$, the sound speed at the target is $c_{s,t} = \sqrt{2T_t/m}$ and the potential hydrogenic energy $\epsilon_{\text{pot}} \approx 16$ eV.

The flow at the target is assumed to be sonic, resulting from the Bohm boundary conditions [44]. The static pressure at the target is roughly half the upstream pressure

$$2 n_t T_t = f_n n_u T_u \tag{1.24}$$

where $1 - f_n$ is the fraction loss of pressure due to friction, and is in the

range 0 to 1. In the case of $f_m \approx 1$ the neutral friction is negligible, and the neutrals can be neglected. In this case the system of equations (1.22), (1.23) and (1.24) can be solved analytically.

Two regimes are distinguished in this regime. The linear regime is the case if $T_u \approx T_t$, i.e. there is no significant drop in temperature towards the target. This regime is sometimes also called sheath-limited, but this might be confused with the sheath-limited regime of filaments, where the currents of filaments are mainly closed via the sheath. The other regime is called the high-recycling or conduction-limited regime. In this case the temperature is significantly reduced at the target compared to the upstream temperature. This can be achieved by moderately high plasma densities and not to high energy influxes upstream.

Shoulder formation

In order to maximise the fusion power, it is beneficial to have the plasma close to the vacuum vessel. Thus it is beneficial to be able to predict the radial profiles in the SOL, such that the first wall has a sufficient distance that the fluxes are low enough to prevent a fast degradation and prevent tritium retention. At the same time, it should also be as close as possible, to reduce the cost.

The SOL can be separated into two regions, the near-SOL, and the far-SOL. The near-SOL consists of the flux-surfaces near the LCFS. It is typically a few mm wide. Beyond that is the far-SOL, that extends all the way to the wall. In the near-SOL, the density decays quickly, and the fluctuations are of moderate level. In the far-SOL, the fall-of is much flatter, and the fluctuations are much stronger [45]. The two different exponential fall-off lengths are the main reason for the distinction between the two

regions in the SOL [36]. Filaments might be responsible for the observed SOL profiles. This will be discussed in more detail in sec. 2.1.2.

It has been observed that the density profiles become flatter across the whole SOL with increasing density. In addition to the flattened SOL, strong fluctuations in the near-SOL have been observed in high density cases [46]. While this has been known for L-mode plasmas, the situation for H-mode is less clear [34]. It has been observed that detachment onset is coinciding with the shoulder formation, however, not in all cases. Detachment describes the cooling of the plasma, before reaching the divertor, and is described in more detail in sec. 1.5.3. It has also been observed that an increased divertor collisionality Λ_{div} coincides with shoulder formation.

1.5.2 Neutrals

As mentioned in sec. 1.3, a plasma consists not only of the charged ions and non-bonded electrons, but also of the non-ionised background gas. The charged particles can interact via electro-magnetic forces, but the neutral interaction is limited to local collisions. Also, neutrals are not strongly influenced by the magnetic field, thus can move easily across field lines. If the plasma is mostly ionised, the neutrals can sometimes be neglected. In the core of tokamaks, the temperatures are sufficiently high that the neutrals can be mostly ignored. An exception is however neutral beam inject (NBI), where ions are accelerated, before they get neutralised, and the accelerated neutrals can then penetrate far into the core before they get ionised [47]. This is used to heat the plasma, as well as to drive a current, as the neutrals can deliver energy and momentum to the plasma. Another example where neutrals, even at low densities can be of importance in the core, is the creation of fast neutrals via charge exchange. If a hot ion under

goes charge exchange with a neutral particle, the process creates a hot, or rather a fast neutral that can leave the core and cause sputtering at the first wall.

Further outwards, in the edge, neutrals become more important, as more neutrals can penetrate into this region, and this can be used to fuel the plasma. Outside the LCFS, neutrals importance increases further, and are often included in transport codes, to capture the plasma physics sufficiently [48–53].

Neutrals can cool the plasma, as the ionisation requires energy. If the temperatures drop to low enough temperatures, in the order of a few eV, the neutrals are excited, rather than ionised, and thus further cooling via radiation is possible, which can provide an efficient mechanism to radiate energy. As already mentioned in the previous section 1.5.1, a significant amount of the power crossing the LCFS must be radiated, rather than reaching the divertor tiles to prevent a fast degradation.

Additional to the neutrals of the main plasma species, namely D for MAST, or D and T for a future fusion plasma, other neutrals can be present and influence the dynamics. These additional minority species can be either intrinsic, meaning they are unintentionally introduced, e.g. from sputtering, or they can be intentionally introduced, e.g. by gas puffing.

Depending on the atoms involved, radiative losses become already at higher temperatures an efficient mechanism, if the electrons are strongly bound, as is the case for high-Z impurities. Impurities are atoms (or molecules) that are not the main species of the plasma. In the case of fusion plasmas, this means any species but hydrogen isotopes. Nitrogen or Argon are for example used for cooling the plasma in the edge [54].

Neutrals are required for reaching sufficiently low temperatures at the

divertor, to prevent melting and to reduce sputtering [55]. This is especially prominent in detachment, which will be discussed in the next section 1.5.3.

As the neutrals are of significance to the design and operation of divertors, control and prediction of neutrals in the edge is of major interest. The main aspects in which neutrals contribute, is they act as an energy sink as well as a momentum sink. This can be included in a simple flux tube SOL model, as the two-point model. The two-point model does however not predict the rates. Getting however the actual rates for momentum sink and energy sink is more complicated, and often requires kinetic treatment of the neutrals [56]. Additional to atomic neutrals, modelling of molecules may be needed to reproduce experimental observations [57].

Compared to present day machines, future fusion devices will have an increased density in the divertor. This further increases the importance of understanding the influence of neutral plasma interactions in the SOL. Plasma wall interactions are a main issue, not only for the operation of ITER, but also for future fusion devices. Therefore increasing the understanding of filaments, one of the main transport mechanisms in the SOL is needed, especially in the presence of neutrals.

Plasma turbulence interactions with neutrals studies have recently been conducted [58–60]. Leddy et al. [58] show that the neutral interaction can be increased by resolving the fluctuations, compared to the mean field approach. Leddy et al. [58] used a fluid model for the neutral model. The neutral model evolved additionally to the neutral atomic hydrogen density the parallel velocity along the magnetic field and the neutral pressure. The decision to include the parallel velocity was motivated as that way it is possible to conserve momentum in the plasma neutral interactions. The cross-field transport was assumed to be diffusive. These simulations where

done in a full 3D geometry with drift ordered fluid equations for the plasma using the BOUT++ library [58, 61]. Bisai and Kaw show that neutrals can reduce electric fields, reduce fluctuations and increase pressure gradients in the SOL [59]. The model includes molecular gas and evolves only the neutrals density including diffusion. Bisai and Kaw state that the neutrals diffusion constant depends as $\mu^0_{n_n}/n_e$ on the electron density. In terms of filament neutral interaction, a recent study by Thrysøe et al. [62] showed that filaments can significantly increase the fuelling of the core by creating energetic neutrals. Thrysøe et al. [62] used a fluid model for the atomic hydrogen neutrals. The neutrals exist in two separate temperature states, a cold fluid at $T_n = 2\,\mathrm{eV}$ and a hot neutral fluid at $T_n = 50\,\mathrm{eV}$. The hot neutrals are born from charge exchange. Each of the fluids is evolved with a diffusion equation, where the diffusion constant depends on the temperature of that fluid [62].

1.5.3 Detachment

As mentioned before, the heat load on the divertor plates needs to be significantly reduced, compared to power that enters the SOL from the LCFS. Neutrals can provide both a reduction of plasma energy by radiative losses and by ionising the neutrals, as well as a momentum sink, mostly via charge exchange. If only a small amount of the plasma is reaching the target, and most of the plasma is cooled in an area of high neutral density in front of the divertor, detachment is reached. An experimental definition of detachment is that with increased upstream plasma density, the target plasma density is reduced. For attached conditions, the target plasma density increases with increasing upstream plasma density. For higher plasma densities the target plasma particle flux decreases after detachment is reached, which is

known as target flux roll-over [63, 64]. This coincides with a strong decrease in the heat load near the strike line, while the reduction in the far SOL is less significant [65].

As detachment is a continuous transition, if the above mentioned observations are not fully observed, the state may be called partially detached, in contrast to fully attached, where most of the plasma's energy and momentum reaches the target, and fully detached, where most of the energy and momentum is absorbed by the neutrals.

ITER is going to be expected to operate in partially detached or fully detached state, to prevent excessive heat load on the divertor tiles, and thus reduce melting and sputtering. This is required to prevent a too fast degradation of the divertor tiles, and to prevent tungsten accumulation in the core.

As detachment is reached, a cloud of cold plasma including many neutrals exists in the divertor. If the cloud moves further up towards the mid-plane, it can reach the X-point, at which point the detachment can significantly reduce core confinement, as many neutrals enter the confined region.

1.5.4 Mega Ampere Spherical Tokamak

The Mega Ampere Spherical Tokamak (MAST) is a spherical tokamak operated in Culham at the Culham Centre for Fusion Energy [26, 66, 67]. It has been recently upgraded to MAST-U, which is in most parts a complete rebuild. MAST-U is going to increase to total, magnetic field, as well as increased pulse duration and plasma current.

MAST as a spherical tokamak has a small aspect ratio. The aspect ratio is defined as the ratio between the major radius R over minor radius

r, i.e. $a = R/r$. It is the successor of Small Tight Aspect Ratio Tokamak (START), and was build after the promising results of START [68, 69]. START achieved a magnetic beta of 30 % - which was much higher than the previous record of 12.6 % achieved at DIII-D [69]. A spherical tokamak has a minor radius r similar to the major radius R and thus confines the plasma close to central solenoid. As the magnetic field decays as $\frac{1}{R}$ this means that higher pressures can be achieved at lower magnetic field strength. Thus the spherical tokamak design might allow to achieve fusion reactors at reduced costs compared to the standard tokamak design [26]. The major radius of MAST is $R \sim 0.85\,\mathrm{m}$ and the minor radius is $r \sim 0.65\,\mathrm{m}$, giving an aspect ratio of $a \sim 1.3$ [70]. The magnetic field drops from 2 T to 0.25 T at the outboard. The maximal plasma current is around 1.2 MA. MAST often operates in a asymmetric double-null divertor. Compared to the single-null geometry shown in fig. 1.2, where a single X-point exists in the lower part of the domain, a double null geometry has a second X-point on the top. Each of the X-points has an associated separatrix. If the differences between the inner and outer separatrix is much less than the heat flux width, the configuration is referred to as connected double-null (CDN). In such a configuration the connection length in the near SOL is around 10 m [71].

MAST has an open vessel, which allows wide angle views using optical observation of the plasma [26, 72]. The SOL of MAST is in general well diagnosed, which makes it suitable for studying filaments [26, 66, 67, 73, 74].

The magnetic field is mostly in toroidal direction. This implies that the connection length along the magnetic field lines from the mid-plane to the divertor is even for medium sized tokamaks like MAST several meters [22]. The pitch angle relates to the ratio of the toroidal magnetic field B_ϕ and poloidal magnetic field B_θ as $\arctan\left(B_\theta/B_\phi\right)$ [75].

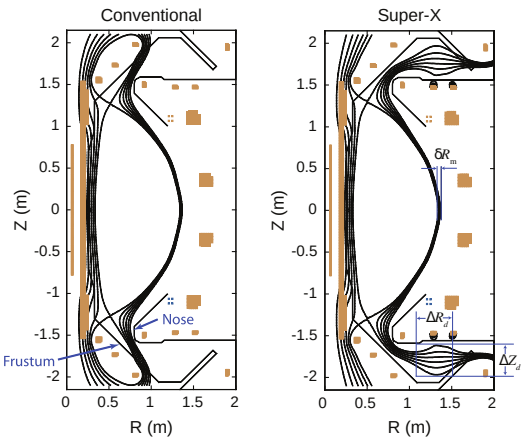

Figure 1.4: 2D cross section of MAST-U showing the divertor design as well as a conventional divertor configuration on the left and a super-x divertor configuation on the right. Reproduced with kind permission from Fishpool et al. [76].

MAST-U is going to be used to study advanced divertor geometries. The large number of magnetic coils in the divertor region allows one to also study other magnetic divertor geometries including standard divertor configuration or snow flake divertor, where a secondary X-point is close to the primary one. One of the new divertor geometries that can be achieved with MAST-U is the super-x divertor, as shown in fig. 1.4. Thereby the outer leg will be pulled further out, to a radius of 1.6 m, compared to the 0.8 m radius of the conventional divertor [76]. MAST-U has a closed divertor configuration, this means that the divertor is partially disconnected from the main chamber, which is expected to allow for a signifcantly higher neutral pressure in the divertor, compared to the rest of the device [76]. MAST-U can also be opperated in the double-decker configuration, where the inner leg is also pulled outwards in the divertor chamber.

1.6 Outline

This thesis studies the dynamics of filaments in order to increase the understanding of the impact of plasma backgrounds on the dynamic of perpendicular transport in the scrape-off-layer (SOL) of fusion devices. This is of interest as filaments are expected to be the significant transport mechanism [77]. A broadening of the SOL has been observed at high densities in different machines [37], and it has been suggested that filaments may be the cause of this transition, in particular an increased resistiviy has been proposed as a mechanism that increases the radial filament velocity. This is discussed in more detail in chapter 2.

This study is addressing the impact of the plasma backgrounds on the dynamics of filaments. This includes the impact of spatially varying backgrounds, especially in the presence of detachment where the plasma in front of the target is much colder than the upstream plasma. As cold plasma in front of target has been suggested to increase filaments' radial velocity, are detached plasmas causing the broadening of the SOL? Also the impact of neutrals on the dynamics of filaments will be studied. Besides a direct impact of neutrals via neutral-plasma collisions, indirect changes are also studied, in particular changes in the plasma backgrounds due to neutrals that are impacting the dynamics of filaments. These questions are answered by studying the radial filament velocity using self-consistent backgrounds. The STORM code was extended to include neutrals, as a step towards more realistic modelling of the backgrounds. The codes including the extensions are discussed in chapter 3.

A 1D version of the codes is used to generate the self-consistent backgrounds. The backgrounds created as part of this work are discussed in detail in chapter 4. This includes the details of the creation of the back-

ground profiles, as well as the physics of the different regimes reproduced by the backgrounds.

The study of the radial filament velocity is presented in chapter 5 for the backgrounds in attached divertor conditions. This includes a detailed discussion of the temperature dependence on the temperature backgrounds, in particular of the distinction between upstream and target temperature dependence.

As chapter 5 raises the question whether the target temperature dependence is holds in detached conditions, which would imply no variation of the filament radial velocity in detachment, chapter 6 extends the study into detached conditions. Thereby a deviation from the target temperature is observed.

The thesis is concluded by a summary of the presented findings. Chapter 7 also puts the results in context, and aims to answer the question on how this thesis has contributed to the broader fusion research.

CHAPTER 2

Review of Filament Physics

Filaments are positive density perturbations which are strongly magnetically aligned, meaning their perpendicular extent is much smaller than their extension along the magnetic field [32]. Filaments have been observed in many magnetised plasmas, for example in space plasmas [78], the here presented review will however only discuss filaments in fusion devices. Various names have been used for filaments, such as blobs, filamentary-blobs or streamers. The name blob stems from 2D imaging, such as Gas Puff Imaging (GPI), where only the cross section of filaments is visible. In this thesis only the term filament is used for consistency.

D'Ippolito et al. [32] define three main requirements for filaments:

- Monopole density perturbation, at least 2 times higher than the surrounding rms fluctuations. Different thresholds are also used, e.g. 2.5 [79].

- Magnetically aligned, i.e. much smaller perpendicular extension that parallel extensions $\delta_\perp \ll \delta_\parallel$.
- Dominant $\vec{E} \times \vec{B}$ advection in the direction of a charge-polarising force, with an associated dipole vorticity and potential structure perpendicular to the filaments motion.

Note that measuring the quantities like the potential or vorticity in experiments can be challenging [32].

2.1 Experimental observations and properties

Filaments have been observed in most fusion devices in the scrape-off layer. In tokamaks for example in JET [80], Axially Symmetric Divertor Experiment - Upgrade (ASDEX-U) [81–83], Tokamak à configuration variable (TCV) [84–86] and DIII-D [31, 87] as well as in spherical tokamaks. e.g. NSTX [88, 89] and MAST [26, 67, 73] as well as in stellarators e.g. Wendelstein 7X (W-7X) [90] and Large Helical Device (LHD) [91]. They have also been observed and studied in linear devices e.g. TORoidal Plasma EXperiment (TORPEX) [92].

The above definition for filaments stem from theoretical models. In experiments, it is often not possible to measure these quantities, or at least it is challenging [32]. Thus for experimental observation, often the intermittency of filaments is used to detect their presence. Langmuir probes are often used to diagnose plasmas, and the signal from Langmuir probes can be used to detect the presence of filaments. If there is an enhanced number of large amplitude events in the SOL, they are typically attributed

to filaments. A single probe gives only limited information about the spatial structure and does not allow one to measure the filament's vorticity or velocity. While the spatial size δ cannot be measured, the rise and fall time τ of the signal can be measured, which gives the size-to-velocity ratio $\tau \sim \frac{\delta}{v_r}$. This gives still some information about the observed filaments [93]. If the same filament is measured by a different probe, the velocity of the filament can be estimated, assuming that the two measurements can be associated. One mechanism to measure the spatial distribution of filaments is conditional averaging [32, 35, 94]. Thereby a reference signal is used to detect filaments, and average over several observed filaments. If the main probe is moved in between, this allows one to construct a spatial image of an average representation of a filament [95]. Using this technique it is also possible to obtain the evolution of a filament, and also to measure averaged electric fields during the occurrence of such an average filaments, via measuring the potential with the probe. Electric fields of a single filament can also be measured with two probes [93].

Another approach for measuring filaments is optical imaging. This allows one to measure the spatial structure of single filaments, as well as their time evolution, which can be used to infer the filament's velocity. Measuring the temperature or density of filaments however is not directly possible, as the amount of emitted light is a non-linear function of plasma density, temperature as well as neutral density [96]. One commonly used approach is gas puff imaging (GPI). Thereby a cloud of neutrals is puffed into the SOL, and the emission of the neutrals is measured with fast optical cameras. This has been used for example in Alcator C-Mod [97, 98], National Spherical Torus Experiment (NSTX) [88, 89, 99] and ASDEX-Upgrade [100]. Beam emission spectroscopy (BES) is similar to GPI, as

also the optical light emitted via neutrals is measured, but unlike GPI, a continuous signal is used [101]. This has been used for example in DIII-D to observe filaments [31]. Both GPI and BES allow one to measure the 2D structure of a filamentary structure in the poloidal, radial plane with a resolution of up to ∼1 mm and ∼1 µs [32]. Another way is to rely on the background neutral gas. This allows for an overview of filaments. This has been applied for example on MAST [73] or TCV [34]. Unlike the active imaging methods, this does not result in the observation of the filament cross section. Rather a 2D projection of the full 3D image is recorded. To get the filament cross section, the image needs to be inverted [37]. In this case the observation is typically done using unfiltered light, which is dominated by the D_α line [72].

Filaments have been observed to be a significant transport mechanism in the SOL of tokamaks [31, 72, 77, 102]. Especially in the far-SOL filaments are causing most of the cross-field transport [97, 102]. As filaments are also in the near-SOL a significant cross field transport mechanism, they might help handle the power in the divertor [103]. Large plasma fluxes onto the first wall materials may degrade the wall and cause sputtering. The thereby introduced impurities can dilute the plasma and degrade confinement. The plasma wall interaction can cause dust production as well as increased tritium retention, both concerns for ITER [30]. Filaments are also considered to explain the flattened density profiles in the far-SOL, which will be discussed in more detail in sec. 2.1.2. Understanding filaments with a view to predicting and controlling them in future devices is therefore of interest. While fully turbulent simulations, including filament generation, transport and interaction with the background are certainly of interest, the high computational cost make it challenging to use them for designing fu-

ture devices. Stochastic models, using an accurate description derived from seeded filament simulations can provide a computationally cheaper option to predict SOL profiles for future design, that can then later be verified using fully turbulent simulations. This will be discussed in sec. 2.1.2.

Filaments are born in the edge of tokamaks. On JET it was first observed that they are born in the edge shear layer [104]. On MAST measurements of the skewness suggest that they are born in the region of maximum electric field in the edge [67]. Gas puff imaging from NSTX suggests that the filaments are created in a region of high relative pressure gradients in the edge [89]. The filaments are then accelerated outwards. As the filaments have a significantly higher amplitude than the background fluctuations, this leads to a skewed probability distribution function (PDF), meaning there are more large positive fluctuations than negative fluctuations. The skewness of the PDF has been observed in many experiments [32].

2.1.1 Experimental observations on filament scalings

In experiments performed on DIII-D the filaments' radial velocity was found to be around 2.6 km/s 0.5 cm outside of the LCFS, and are dropping to around 330 m/s near the wall. The decrease in radial velocity is positively correlated with an decrease in radial size, which decreases from 4 cm to 0.5 cm [31]. The sizes are given as the full width of the filament. Rudakov et al. measured in H-mode the radial velocities to be around 1.5 km/s, and the filament sizes where around 1.5 cm [87]. This was measured in the near SOL, 1 cm outside of the LCFS. Rudakov et al. measured the size of filaments in L-Mode to be around 2.5 cm compared to the 4 cm measured by Boedo et al. [31, 87].

A measurement of filament peak density, temperature and radial veloc-

ity is shown by Rudakov et al. for the DIII-D tokamak [35]. The measured data does not show a strong correlation of average density and filament velocities. For the case of $f_{\mathrm{GW}} \approx 0.27$ the SOL temperature is increased around 6 to 10 cm outside the LCFS compared to the the other shots. The filament velocity is slightly increased compared to the other shots at the same plasma current. The velocity increase for the shot with lower plasma current is stronger, in which case both the filaments density and temperature is increased. In all cases the filament velocity increases from around 0.5 km/s at the LCFS, towards around 1 km/s at around 2 cm outside the LCFS, and drops to less than 0.5 km/s at around 6 cm outside of the LCFS [35].

At NSTX GPI has been used to track single filaments, which has been used to calculate the filaments' radial velocities [89]. The velocities lie between 100 m/s and 1.4 km/s. There is no obvious trend for the filament velocities as a function of distance from the separatrix - one filament accelerates, one decelerates and one first decelerates, then accelerates before decelerating again. The observed velocities lie mostly within the expected range from theoretical scalings, but the range of expected velocities span partially over an order of magnitude.

In JET the filaments are found to have a radial velocity around 0.38 km/s 4 cm outside of the separatrix for edge localised mode (ELM) filaments, while L-mode filaments are measured with 95 m/s and inter-ELM filaments with 60 m/s. The size of L-mode filaments was around 1 cm [80].

Kirk et al. observed in MAST that the perpendicular width of L-Mode filaments have a dependence on the plasma current [105]. The increase of the plasma current resulted in a shift of the PDF of the bi-normal filament size to larger sizes. Kirk et al. suggest that the dependence might

be introduced via the dependence of the parallel connection length on the plasma current [105]. The radial filament size decreases slightly with increasing plasma current. Kirk et al. find an average radial velocity of $0.84 \pm 0.03\,\mathrm{km\,s^{-1}}$ for a plasma current of 400 kA, and an average radial velocity of $0.36 \pm 0.03\,\mathrm{km\,s^{-1}}$ for the 900 kA plasma current [105]. This means that in addition to the radial filament size, the radial velocities of the filament decrease with increasing plasma current. Kirk et al. also found that the density fall-off length in the SOL decreases with plasma current [105]. This supports the picture that density profiles are governed by the dynamics of filaments.

Katz et al. [106] study the impact of a neutral background on the dynamics of filaments. A filament is generated using a microwave pulse and the resulting motion due to curvature drive is studied. By varying the neutral pressure, the impact of the neutral on the filament dynamics was studied. The study does not include a plasma background or plasma sheaths effects, as the filament is propagating in closed field lines. For the parameters used an inverse proportional dependency on the neutral density is observed for the filaments' radial velocity [106]. Theiler et al. [92] measure for the filaments observed in TORPEX a small decrease of the filaments' radial velocity with increasing neutral density.

2.1.2 Impact on SOL profiles

Traditionally the SOL of fusion plasmas has been modelled with 2D transport codes, that take a diffusion constant for the cross field transport. As mentioned in the previous section, the SOL, and especially the far-SOL is dominated by intermittent, large scale fluctuations. These are non-local events, and thus a local diffusion coefficient cannot predict the resulting

profiles. As the transport is inherently turbulent, turbulence transport codes have been developed for the SOL.

The flattening of profiles is an issue for fusion devices, as that can increase impurities as well as increase tritium retention. Understanding and predicting this is of interest. Currently filaments are one of the prime candidates to explain the SOL profiles. A change in the dynamics of filaments may thus trigger the flattening of SOL profiles. Stochastic models, that describe the SOL in terms of independent filaments have not only been used to reproduce the flattening in the far-SOL, but they can also reproduce the skewness of the PDFs in the far-SOL [73, 107, 108]. Thus filaments are a promising candidate to explain the SOL flattening.

As filaments are born in the edge of the tokamak, the filaments observed in the far-SOL are not born local, thus filaments are a non-local phenomena, and thus previous approaches of local diffusion rates are not sufficient for capturing the SOL transport [84, 97, 102]. Filaments have been observed to cause significant radial transport in the SOL in several devices [31, 72, 102].

Militello et al. [36] propose a stochastic model that assumes filaments as independent, randomly appearing events. The model requires the filament dynamics and the filament occurrence rate as input. The occurrence rate depends on size and amplitude. Filament shape, velocity and draining function are needed in terms of the filament dynamics, to calculate the SOL profiles [36]. Thereby several ways are discussed to achieve the double-exponential scrape-off layer profiles that are observed in many experiments [37]. The first effect to achieve this is to assume a double exponential decay in the draining function of the filament amplitude, rather than assuming a single exponential. This however results in decreased fluctuations levels in the far-SOL, which is in contrast to experimental observations,

where in the far-SOL increased relative fluctuation levels have been observed [37]. The next mentioned possibility is accelerating filaments. If filaments accelerate further out in the SOL, this results in non-exponential density profiles, in contrast to the decreased drain, the relative fluctuation level increases. Also a distribution of filaments of different amplitudes, and more so filaments of different perpendicular size can also lead to a flattening of the far-SOL [37]. Similar to the case of an increasing filament velocity, either results in increased fluctuation levels in the far-SOL.

This model has been used to reproduce the SOL profiles in MAST. Thereby the filament occurrence rates of filament size and amplitude are taken from experimental measurements. The radial velocity was assumed to be constant and the drain exponential. This method reproduces the experimentally observed SOL profile and fluctuations [107].

A similar comparison was done for JET [108]. Thereby the experimental observed PDF, the auto-correlation function of the Langmuir probe (LP) and the scrape-off layer profiles where matched. Thereby SOL profiles featuring different conditions where featured, ranging from a steep radial profile, via a SOL profile which is partially flattened, to a third SOL profile, where the density was further increased, all of which where measured at JET during a density ramp [73]. A set of parameters for the filaments was found that matches the LP measurements in the low density case. The parameters include a filament velocity scaling factor and filament size probability distribution, given by a Gaussian distribution. Additionally to finding good agreement with the above mentioned LP data, the filament occurrence frequency as well as the velocities are in agreement with previous observations in JET.

Fedorczak et al. proposes an similar model for modelling the SOL that

assumes saturated turbulence [109]. Thereby the results for the density fall of length is compared to the results of fully turbulent simulations using TOKAM2D, the 2D version of TOKAM3X. The model derives the filament properties, which are required for the stochastic SOL model by approximating the quantities in spectral space.

Paruta et al. [110] compare the filament motion observed in fully turbulent simulation in a full diverted tokamak geometry with analytical scaling predictions. The numerical model is a cold-ion drift ordered fluid model. They track filaments above a 2.5 rms fluctuation threshold, and measure velocity and size for the filaments. For small filaments they find that the velocity is limited by the inertial scaling prediction. Paruta et al. [110] claim that large filaments show good agreement with the resistive X regime, however many larger filaments are faster than predicted by the analytical model, while smaller ones are slower. From the data no clear trend is visible [110]. This may be caused by an use of an average of radial and bi-normal size, that is mainly dependent on the radial size. As Omotani et al. found, the inertial scaling depends on the radial size, while the sheath limited scaling is rather dependent on the bi-normal size [111]. Such a discrepancy can emphasise that further work in predicting filament's motion is required. Such studies complement scaling studies, as such simulations allow a more direct comparison of seeded filament simulations compared to experimental observations. While the stochastic SOL model by Militello et al. [36] can be used to explain experimentally observed SOL profiles, studies such as the comparison of analytical scalings to fully turbulent simulations can be used to verify the scaling laws. Unlike experimental observations, they allow a detailed tracking of filaments, as well as a reliable analysis of density and temperature profiles of the filaments.

To match the profiles in the higher density cases, the parameters used for the initial scan where varied. Thereby the three methods, as outlined by Militello et al. [36], that result in a flattened SOL, where studied. Thereby an increase of the drain time τ by a factor of 25 showed good agreement with the experimentally observed flattened SOL profiles. In the case where the filament velocity was increased to match the profiles and the PDF, the auto-correlation function did not match the experimentally observed one. Walkden et al. note that they only tried varying a single parameter while in the experiment probably different parameters change [108]. Thus the often observed correlation between shoulder formation and collisionality Λ might just be one of the driving mechanisms of shoulder formation [108].

Vianello et al. [34] found that the shoulder formation is not triggered by a change in collisionality, but rather by a change in line-averaged density [34]. Vianello et al. [112] scanned the dependence of the SOL profiles as they changed the connection length [112]. As the collisionality is the integrated resistivity along the flux tube, this changes the collisionality. The density fall-off length in the near-SOL showed a strong dependence on the line-averaged density, but only weakly on the connection length. In the far-SOL, the density fall-off length depended on neither [112]. The increase in density resulted in an increased size of the filaments. At the same time, the filament's radial velocity decreased slightly.

2.2 Modelling of filaments

The basic properties of filaments can be captured using a two dimensional system of fluid equations, i.e. the parallel spacial dimension can be dropped and no higher moments of the distribution functions are required to capture

the drift motion of filaments [32, 96]. A basic model and the associated set of equations is introduced in sec. 2.2.1.

This basic model has been extended, in order to refine the accuracy and thus the predictability in various ways, e.g. inclusion of a finite electron temperature perturbation [113], inclusion of a third dimension [22] or the inclusion of finite Larmor radii effects [114].

2.2.1 Basic model

For filament simulation field aligned coordinate systems are often used [32]. If the full geometry is retained, this results in the use of curvi-linear geometry. This can be significantly simplified by replacing the full curvature terms with a curvature operator. This allows one to replace the full curvi-linear geometry with a Cartesian coordinate system, and replace the curvature operator by an analytical expression. This is commonly used for filament models [22, 26, 32, 115, 116]. The radial direction is denoted by x, the z-direction is along the (equilibrium) magnetic field, and y is in the bi-normal direction $\hat{e}_y = \hat{e}_z \times \hat{e}_x$.

A further simplification is to drop any dependency in the parallel z direction. Using the previously mentioned definition of a filament, a simple model can be derived. It consists of a density field n, which is governed by the continuity equation

$$\frac{\mathrm{d}n}{\mathrm{d}t} = \frac{\partial n}{\partial t} + \vec{v}_E \cdot \nabla n \approx 0 \tag{2.1}$$

with v_E the $E \times B$ drift velocity. $\frac{\mathrm{d}}{\mathrm{d}t}$ defines the convective derivative, being

the sum of the partial derivative and and advective contribution:

$$\frac{\mathrm{d}}{\mathrm{d}t} = \frac{\partial}{\partial t} + v_E \cdot \nabla \tag{2.2}$$

Applying charge conservation results in the vorticity ω and its equation:

$$\frac{\partial \omega}{\partial t} = \nabla_{\parallel} J_{\parallel} + \frac{c}{B} \vec{b} \cdot \nabla \times \vec{F} \tag{2.3}$$

where $J_{\parallel}$ is the parallel current. The potential ϕ is given by:

$$-\nabla(n \nabla_{\perp} \phi) = \omega. \tag{2.4}$$

Solving for the potential can be challenging, both numerically as well as analytically. Therefore often the so called Boussinesq approximation is used. Thereby the density term is pulled out of the derivatives, such that the two first order differential operators can be contracted to a second order perpendicular Laplacian [117]. Using this approximation, the equation for the potential ϕ can be rewritten as

$$-\nabla_{\perp}^2 \phi = \frac{\omega}{n} \tag{2.5}$$

.

This system of equations can be solved analytically neglecting the plasma background and a Gaussian perturbation of amplitude δ_n and width $\delta_{\perp}$:

$$n = \delta_n \exp\left(\frac{-x^2 - y^2}{\delta_{\perp}^2}\right). \tag{2.6}$$

The force is assumed to be due to the toroidal curvature and the drop of $\vec{B}$ due to the inversely proportional dependence on radius. A linear

dependency between the current and potential is assumed, namely $J_{\parallel} = ne^2 c_s \phi / T_e$. Further assuming a stationary solution, the radial velocity is given as

$$v_x = c_s \frac{L_{\parallel}}{2R} \left(\rho_s / \delta\right)^2 . \tag{2.7}$$

Without the above mentioned assumption and linearisation, the system is not analytically solvable [32].

2.2.2 Three dimensional effects

As mentioned before the parallel direction is often neglected. In this case some assumptions must be used. One of the commonly used closures is the sheath dissipation closure. This closure neglects parallel gradients. Another closure is the vorticity advection closure, which neglects parallel currents. The vorticity advection does not work for large filaments, where parallel currents are important [22]. The variation along the magnetic field lines introduces also Boltzmann spinning [22], which is a spinning motion due to a monopole contribution in the potential. Also the associated poloidal drift is not observed with 2D closures. Including the parallel dynamics can influence the dynamics of filaments. Resistive drift waves can slow the motion of filaments by producing more diffusive filaments [118]. This effect is particular strong for filaments with small cross section. Due to the diffusive nature of the drift waves, small scale structures are reduced [118]. The drift waves are especially important for filaments of large amplitude [22].

2.2.3 Finite temperature perturbation

Another step towards a more complete picture of the physics involved, finite electron temperature perturbation can be included. The inclusion can significantly influence filament dynamics, as it increases the poloidal motion and decreases the radial velocity [113]. The thermal perturbation can cause a strong current in the filament, due to the fast motion of the electrons. This causes a monopole in the potential, which then causes the rotation of the filament.

2.2.4 Scaling of filaments

Scaling laws, describing the filaments radial velocity as a function of plasma background parameter, have been derived [113, 119, 120]. The scalings neglect not only neutral plasma interactions, but simplify the equations in further ways, to get an analytical expression for the filament velocity.

Depending on the perpendicular size $\delta_\perp$ of the filament, the scaling can be strongly different, as the ways the vorticity is closed is dependent on the regime the filament is in. For small filaments, typically the advection closure is used.

To derive the typical velocity, the typical electrical field is required. This derivation follows the approach outlined by Walkden et al. [113]. The steady state solution of the vorticity equation is used to approximate the electric field in the filament. Starting from eq. (2.3) only the source and the advection terms are retained for small filaments:

$$0 = v_E \nabla \phi + g \frac{\partial n}{\partial y} \tag{2.8}$$

Spatial derivatives are replaced with $\frac{1}{\delta_\perp}$, as the length scale on which a

quantity changes is the size of the filament. Further the velocity is proportional to the electric field, thus $\frac{\phi}{\delta_\perp}$. Using the Boussinesq approximation $-\nabla_\perp^2\phi = \omega$, the derivatives can be replaced by $\frac{1}{\delta_\perp}$ and thus $\phi = -\delta_\perp^2\omega$. Substituting the terms in the above equation yields

$$\frac{\phi^2}{\delta_\perp^2} = g\frac{\delta_n}{\delta_\perp} \tag{2.9}$$

with δ_n the density perturbation. Solving for v_r gives the inertial scaling

$$v_r = \sqrt{g\delta_n\delta_\perp} \tag{2.10}$$

In the case of high viscosity, the vorticity is predominantly closed by diffusion, in which case the diffusion term, rather than the advection term in eq. (2.3) needs to be retained:

$$0 = g\frac{\partial n}{\partial y} + \mu_\omega\nabla_\perp^2\omega \tag{2.11}$$

Using the above introduced assumption, this yields the viscous scaling

$$v_r = \frac{g\delta_n}{\mu_\omega}\delta_\perp^2 \tag{2.12}$$

For large filaments typically the sheath closure is assumed, where the drive is mostly closed by sheath currents

$$0 = g\frac{\partial n}{\partial y} + \frac{\phi}{L_\parallel} \tag{2.13}$$

approximating again derivatives with the filament size, gives the sheath

scaling [22]

$$v_r = g\delta_n L_\parallel \delta_\perp^{-2} \tag{2.14}$$

The scaling has been observed in several numerical simulations [115, 121].

In the case of dominant neutral-ion interaction the neutrals can be the main closing path for the curvature drive. Kube et al. [122] derive a neutral-friction scaling of

$$v_r \propto \frac{g}{\Gamma} \tag{2.15}$$

with Γ the ion-electron collisionality. The numerical investigation by Kube et al. [122] reproduces this scaling for sufficiently large collisionality and thus reproduce the results by Katz et al. [106].

To analyse the dynamics of filaments in theoretical studies, the filaments perpendicular size is often discussed with respect to critical size of filaments [119, 121]. The critical size δ^* is the perpendicular filament size where two different closing mechanism are similar in magnitude, typically the sheath closure, involving parallel dynamics, and the inertial scaling, also known as resistive ballooning regime [22, 89, 121]. Myra et al. derive a critical size [89]

$$\delta^* = \left(\frac{L^2\rho_s^4}{R}\right)^{\frac{1}{5}} \tag{2.16}$$

Easy et al. [121] compared the theoretical prediction from Myra et al. [89] for the transition from inertial scaling to sheath limited scaling using a 3D, isothermal version of STORM, which is introduced in sec. 3.3. By scanning the radial velocities of filaments as a dependence of the per-

pendicular size of filaments, the transition size was determined. By artificially changing the parallel viscosity, the scan was repeated for different viscosities. This showed that the transition happens at smaller sizes than predicted by analytical theory [89, 121].

Easy et al. compared scaling of filaments in two and three dimensions [22]. In two dimensions, using the vorticity advection closure, a scaling of the peak radial velocity v_r with the filament size $\delta_\perp$ of $v_r \propto \sqrt{\delta_\perp}$ is observed. With the sheath dissipation closure, the $\sqrt{\delta_\perp}$ scaling is only observed for small filaments, i.e. for filaments smaller than the critical size $\delta_\perp \ll \delta^*$. For filaments much larger than δ^* the scaling converges to $v_r \propto \delta_\perp^{-2}$. The 3D filaments agree mostly with the observation from the 2D sheath dissipation closure. Depending on the parallel extend of the filament, the observed radial velocity is faster or slower, than the 2D model predicted. For larger filaments, the decay is not as fast for the 3D model than for the 2D model. Such large filaments are not observed in experiments. Easy et al. [22], following the derivation of [92, 118], derive an analytical expression for the critical filament size δ^*. The assumption is that viscous effects are small in the SOL and can be neglected. The main contribution balancing the generation of vorticity are polarisation currents and sheath currents. Polarisation currents are dominant for small filaments, and sheath currents for large filaments. If both currents are of similar magnitude, the filament is of critical size, which leads to

$$\delta^* = \left(\frac{g L_\parallel^2}{2} \frac{\delta_n}{n_0 + \delta_n} \right)^{\frac{1}{5}} \tag{2.17}$$

Such scalings are important, as they significantly contribute to the understanding of filaments. Further they can be used as input into broader

models, as it has been done e.g. by Militello et al. to model the shape of scrape off layer profiles including the velocity scaling of filaments [36].

Most studies look at circular shaped filaments. Omotani et al. [116] have used the STORM model to extend this by studying elliptical shaped filaments. Thereby not only the eccentricity of the seeded filament was varied, but also the angle of the seeded perturbation with respect of the direction of drive. Omotani et al. [116] found that plotting the filament's radial velocity against the radial width δ_x, showed a dependence proportional to $\sqrt{\delta_x}$ for small filaments. The dependence for large filaments was similarly found if the peak radial velocity was plotted against δ_y, i.e. against the width in the bi-normal direction, where a δ_y^{-2} dependence was observed [116]. While this was done with a 2D code, and verified with 3D simulations, it is intend that the results can be more or less directly extended to filament simulation which include a more complete physics model.

Similarly most filament studies are done on single, non-interacting filaments. Militello et al. studied the interaction of filaments using 2D and 3D simulations [123]. The study found that filament interaction is caused by the overlapping of the electric fields caused by the vorticity of the filaments. The interaction however quickly drops off, and is only important for distances on the order of the filament size, for larger distances the filaments can be modelled as independent [123]. Militello et al. conclude that, at least for the filaments detected in MAST, the distance of the observed filaments justifies as to treat them as single filaments [123].

The above mentioned filament codes have been benchmarked with experimentally observed filaments in the TORPEX device as well as with filaments observed in the SOL of MAST [96, 124].

2.3 Sheath physics

If a plasma interacts with a surface, a sheath develops at the boundary. As the electrons are more mobile, leading initally to a larger electron flux than ion flux to the wall and thus the sheath consists of an area that is depleted of electrons. The charge density causes an electric field which in turn causes the ions to be accelerated. In order to study the sheath, a model allowing for charge separation as well as a small enough spatial resolution to resolve the sheath is required, thus rather than modelling the sheath itself, the sheath physics is replaced by appropriate boundary conditions. For a plasma fluid model these boundary conditions consist of the Bohm criterion for the ions [44], where the ion velocity U has to reach the speed of sound c_s depending on the electron temperature T_e, ion temperature T_i and ion mass m_i at the entrance to the sheath

$$U = c_s = \sqrt{\frac{T_e + T_i}{m_i}} \tag{2.18}$$

The electrons are much lighter and respond faster to electric forces, thus balance the potential ϕ at the target. The electron velocity V at the sheath is

$$V = \sqrt{T} \exp(-\frac{V_f}{T_e} - \frac{\phi}{T_e}) \tag{2.19}$$

with V_f the floating potential given by

$$\frac{eV_f}{T_e} = \frac{1}{2} \log \left(2\pi \frac{m_e}{m_i} \left(1 + \frac{T_i}{T_e} \right) \right) \tag{2.20}$$

For the steady-state background the ion and electron velocity need to be equal, thus $U = V$ and thus the potential at the target is $\phi = -V_f$.

If the filament causes a temperature perturbation, this also results in an perturbation of the boundary condition for the electrons.

The current J is given by $J = n(U - V)$ thus the sheath current is given by

$$J = n(U - V) = n\sqrt{T}\left(1 - \exp(-V_f - \frac{\phi}{T})\right) \tag{2.21}$$

This expression is non-linear in the potential ϕ but a taylor expansion can be used to get the first order response for small perturbations, which then gives the linear sheat boundary condition mentioned in section 2.2.1.

CHAPTER 3

BOUT++ and STORM

The simulation presented in this thesis have been run using the STORM [22, 113, 116, 121, 123, 125, 126] code, which is a physics model using the BOUT++ library. As part of this thesis, STORM has been extended with a neutral fluid model. The neutrals model is implemented as a separate module, to allow easier reuse in other codes, and will be presented in sec. 3.4. First however, the BOUT++ framework will be introduced in sec. 3.1 and the STORM physics model in sec. 3.3.

3.1 BOUT++

BOUT++ is a library written in C++ which allows for writing parallel plasma-fluid simulation in curvilinear geometry using the message passing interface (MPI) and OpenMP for parallelisation [61]. BOUT++ is a

rewrite of the BOUT code, having its name from its use as BOUndary Turbulence code. BOUT++ is developed on github[1] by an international group, receiving contributions from the University of York (UK), Lawrence Livermore National Laboratory (LLNL), Culham Centre for Fusion Energy (CCFE), Technical University of Denmark (DTU) and other international partners [127]. BOUT++ was written to allow a more flexible implementation of BOUT [128, 129]. As such there is a physics model called BOUT++ which is using the BOUT++ framework, but in this theses BOUT++ always refers to the framework, unless otherwise noted. BOUT++ is licensed under the Lesser General Public License version 3 or later (LGPLv3+) license [130, 131], that ensures that BOUT++ is free and can be used in research. The license is introduced in appendix D.

3.1.1 A short introduction to CFD

Plasmas fluid simulations are a special case of computational fluid dynamics (CFD). One of the main differences between standard CFD codes and the plasma codes in fusion research is the difference in the supported geometry. While the shape of a tokamak or stellarator is simple compared to the shapes required in other fields of CFD, such as plane modelling, the magnetic field makes it beneficial to use a complicated coordinate system, thus preventing the use of general CFD codes in fusion research.

In CFD, the fields that are to evolved are first discretised onto a grid. Additionally, the time is discretised, and the field is evolved iteratively in time. We will here focus on regular grids, as these are preferred due to the simple geometry. One option to discretise a field is by approximating the field locally by simple functions. The other option is to sample the field

[1] `https://github.com/boutproject/BOUT-dev`

at several points, and approximating the field using these values. The first approach is often used in engineering in the finite elements method (FEM) that is beneficial for non-regular grids. On regular grids, approximating the derivatives of a field f with finite differences is conceptually simple and computationally efficient:

$$\frac{\partial f}{\partial x} \approx \frac{-f_{i-1} + f_{i+1}}{2\Delta x} \tag{3.1}$$

where i is the spatial index and Δx is the grid spacing. The field is locally expanded in a Taylor expansion of arbitrary order, and the above shown centred derivative is stencil is to second order accurate. A 4-th order accurate stencil is

$$\frac{\partial f}{\partial x} \approx \frac{f_{i-2} - 8 * f_{i-1} + 8 * f_{i+1} - f_{i+2}}{12\Delta x} \tag{3.2}$$

Increasing the order of accuracy of a stencil increases the computational cost. In order to calculate the derivatives at the boundary of a domain, the centred stencils require cells outside the domain, which can be set by boundary conditions. Similar to the derivative stencils, the values can be calculated by Taylor expansion. Typically either the value at the boundary or the derivative of the field is given, and can be included in the calculation of the cells outside of the domain. High order schemes do require more boundary cells, which can lead to numerical instabilities caused by them. Besides that, higher order schemes are not necessarily the most appropriate way to improve accuracy. In the presence of shocks, refining the mesh gives a more accurate result than increasing the order of the differencing scheme [132].

Assuming the equation to be solved is a first order differential equation

of the form

$$\frac{\partial f}{\partial t} = F(f, x, t) \tag{3.3}$$

where f can be a scalar field, a vector field, or several of either, and F is a functional giving the time derivative, which may include differential operators and can be calculated with e.g. the above mentioned stencils. Such a system can be evolved in time using the simple Euler-Method [133]:

$$f_{j+1} = f_j + F(f_j, x, t_i) \cdot \Delta t \tag{3.4}$$

where j is the time index, and Δt is the time step. Note that this is only accurate to first order in time. Higher order can be achieved by using a Runge-Kutta method, where one or more intermediate steps are calculated [133]. If the time steps are explicitly calculated as described above, the time step needs to be sufficiently small, at least the time step needs to be smaller than the time it takes for the advection to cross one cell, i.e. $\Delta t < \frac{\Delta}{|u|} x$ where u is the velocity. Another type of time solver are implicit time solver. In contrast to the before mentioned explicit methods, F is calculated at the new time, i.e.

$$f_{j+1} = f_j + F(f_{j+1}, x, t_i + \Delta t) \cdot \Delta t \tag{3.5}$$

Note that this does not directly allow for the calculation of f_{i+1}. Various iterative methods can be used to calculate this, where the appropriate choice depends not only on the system of equations but can also depend on the parameters used [134]. One such group of methods are Newton-Krylov methods, where the Newton iteration is used to find the solution, and the

Krylov subspace method is used for inverting the jacobian matrix [134, 135].

3.2 Overview of BOUT++

BOUT++ uses the finite difference method, although additionally some finite volume schemes are available. Finite volume stencils are a variant of finite differences, that take the cell volume into account for flux derivatives, and can thus conserve the number of particles up to numerical precision. Additional to centred differences stencils, weighted essentially non-oscillatory (WENO) stencils are available as well [61, 136]. Additional flux and upwinding schemes are implemented for advective derivatives. Further BOUT++ has support for the bracket operator, which computes a derivative of the form

$$-\frac{\nabla\phi \times \vec{b}}{B} \cdot \nabla f \tag{3.6}$$

which appears quite often in drift ordered fluid equations due to the $\vec{E} \times \vec{B}$ advection. BOUT++ also supports staggered grids, where one of the grids is offset with respect to the main grid by half a grid spacing. Normally quantities are defined in the centre of the cell. In the staggered grids the quantities are defined on the cell edge. By defining flux quantities on the staggered mesh, the checker-board instability can be reduced [137], which in other cases may appear due to a partial decoupling of odd and even cells, a consequence of the stencilch eq. (3.1) being used for advective derivatives.

Although BOUT++ is not strictly limited to tokamak geometry, it is developed with a focus on the edge and SOL region of tokamaks. One of the consequences is an assumed toroidal symmetry of the geometry. A varying metric tensor in the toroidal direction is not supported, although currently

work is under way to remove this restriction, in order to allow simulations in stellarator geometries. The metric tensor can vary freely in the radial and poloidal direction.

The BOUT++ library comes with support for several solvers for the time evolution. Implicit as well as explicit methods are supported, as well as implicit-explicit (IMEX) schemes, which allows one to evolve some fields using explicit schemes, while other fields can be evolved using implicit solvers [138]. Note that most of the time solvers are not part of BOUT++ itself, but rather BOUT++ provides an interface to use various external solvers, such as Portable, Extensible Toolkit for Scientific Computation (PETSc) [139], pvode [135], arkode [140], cvode [140] or Scalable Library for Eigenvalue Problem Computations (SLEPc) [138, 139].

Additional to the above mentioned differential operators, BOUT++ provides convenient ways for basic maths operations on fields, such as multiplication or subtraction, which is implemented using operator overloading in C++ [61].

The library is written in C++ and by providing a high level application programming interface (API) allows one to write the physics equation in close to analytical form. This can significantly reduce the development time for physics models. It further simplifies to read, modify or study equations. While this abstraction does allow for faster changes to the physics model, it comes with a certain runtime cost. As the fluid models are often changed, and e.g. certain terms added or other effects temporarily disabled to check their impact, thus often more time and cost is spent on developing the codes than running them. Thus this is often a favourable trade off, if an appropriate model for the system is not fully established.

Another recent development in BOUT++ was to extend the test suite

significantly. Additional to running a few simulations and comparing with earlier or analytical results, various tests using the method of manufactured solution (MMS) and unit tests have been added [138, 141]. This ensures not only that no major mistakes are introduced over time, but also can be used that e.g. the differential operators are correctly implemented, or that the boundary conditions converge with the expected order.

As the physics model is written in close to analytical form, the amount of code that needs to be checked can be limited to a few dozen to some hundred lines. It also can be used to write code with limited understanding of the inner mechanisms of BOUT++. BOUT++ aims to find the balance between performance and usability to enable new and original research.

As BOUT++ is written mainly in C++, this allows one to achieve good performance, as well as rather straight forward implementation of physics modules.

A BOUT++ module is a program that mainly uses the BOUT++ library for solving a physics problem. Such a module consists of the code that implements the equations using the API discussed above. Additionally an input file is needed, that specifies the differential operators, and either defines the grid or refers to a grid file if a full tokamak geometry is used. The input file allows one to control parameters, in the physics model, such as filament size, providing a convenient way of running scans without having to recompile the code, or having to parse parameters. BOUT++ also ensures that the set of parameters is stored, thus simplifing to reproduce the results.

A more detailed description of BOUT++ is available in the manual folder of the BOUT++ project. A pre-compiled online version is also avail-

able[2].

During this PhD several improvements have been contributed to BOUT++, some of them are described in appendix C.

3.3 STORM

STORM [22, 113, 116, 121, 123, 125, 126] is a physics model for simulations of filaments in the scrape of layer of fusion devices using the BOUT++ framework. The model is mainly developed at CCFE in the UK. The version discussed here was extended to include the interaction with neutrals. The neutrals model will be discussed in more detail in sec. 3.4.

STORM is a drift ordered full fluid model, following the approach of Simakov and Catto [142, 143]. The equations are given in Bohm units, which are introduced in sec. 1.3.1.

3.3.1 Geometry and setup

In the here presented simulations STORM is using a slab geometry. Thereby a flux tube, as shown in fig. 3.1 is straigtend. In the slab geometry used, z denotes the parallel direction along the magnetic field lines. As shown in fig. 3.2, at $z = 0$ is a symmetry plane and at $z = L_{\parallel}$ sheath boundary conditions are applied. In y direction periodic boundary conditions are set, and in x direction zero gradient boundary conditions.

The general work flow is as follows:

- 1D background profiles are generated by providing an energy source and density source upstream in the domain. Only the parallel direction z is included.

[2] `https://bout-dev.readthedocs.io`

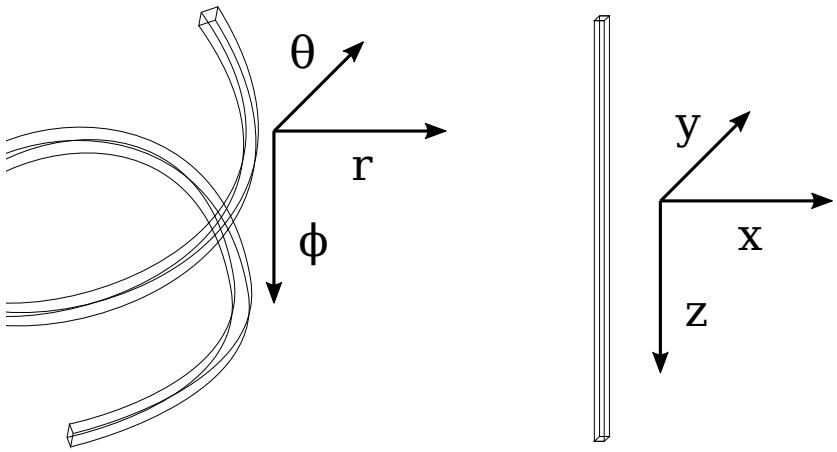

Figure 3.1: Sketch of the mapping between the slab geometry and a flux tube in a tokamak. The radial direction r is mapped to x in the slab geometry. z is the direction parallel to $\vec{B}$, and y is the bi-normal direction.

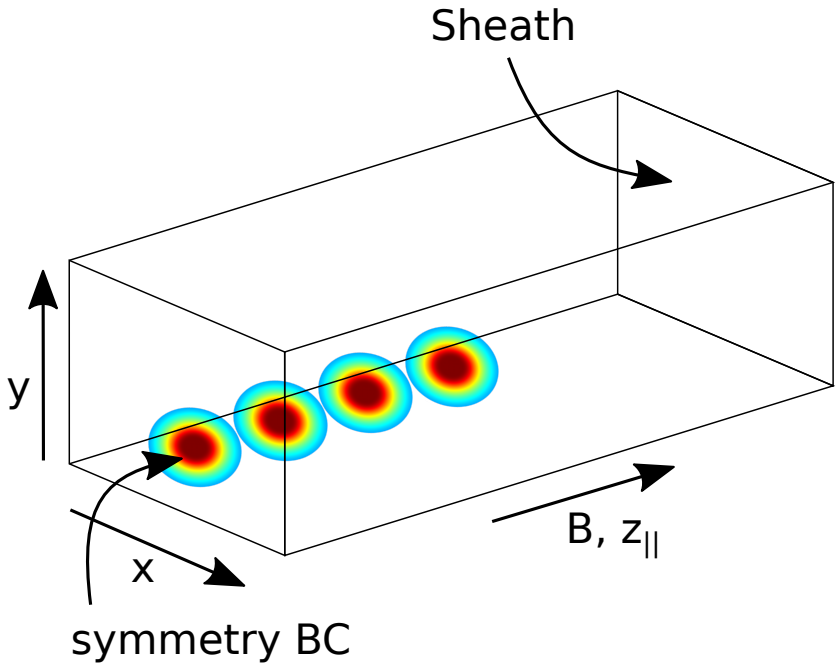

Figure 3.2: Sketch of the geometry including a seeded filament.

- The 1D profiles are extended onto 3D by setting each quantity $\alpha(x, y, z)$ to the computed 1D values as $\alpha(x, y, z) = \alpha(y)$. The 3D background, as extended from 1D, has only a dependence in the parallel direction.
- A density and temperature perturbation is added, as described in sec. 3.3.5.
- The 3D system with the added perturbation is evolved, using the equations discussed in sec. 3.3.2
- The resulting dynamic is analysed. Some of the methods used are introduced in sec. 3.5

3.3.2 Equations

The STORM equation describing the plasma consist of the density n equation for the electrons

$$\frac{\partial n}{\partial t} = A_n^{\perp} + A_n^{\parallel} + B_n + C_n + N_n \tag{3.7}$$

$$A_n^{\perp} = \frac{\nabla\phi \times \vec{b}}{B} \cdot \nabla n \tag{3.8}$$

$$A_n^{\parallel} = -\nabla_{\parallel}(Vn) \tag{3.9}$$

$$B_n = \mu_n \nabla^2 n + (\nabla\mu_n) \cdot (\nabla n) \tag{3.10}$$

$$C_n = -gn\frac{\partial\phi}{\partial y} + g\frac{\partial nT}{\partial y} \tag{3.11}$$

$$N_n = \Gamma^{\text{ion}} - \Gamma^{\text{rec}} \tag{3.12}$$

where ϕ denotes the potential, which is the Laplacian inversion $\omega = \nabla_{\perp}^2 \phi$ of the vorticity. The vorticity in this context is only the parallel component of the vorticity, which is the curl of the flow, and thus denotes "vorticies" in the perpendicular plane. A_α denotes the advection contribution for quantity α, here $\alpha = n$. A_α has been split in parallel $A_\alpha^{\parallel}$ and perpendicular contribution $A_\alpha^{\perp}$. Advection denotes the transport with the flow of the fluid. $A_\alpha^{\perp}$ is due to $E \times B$ advection. The magnetic field is of direction $\vec{b}$. μ_α is the diffusion rate for quantity α, so μ_n denotes the diffusion rate for the density, resulting in the diffusion term B_n. μ_n is [144]

$$\mu_n = \left(1 + 1.3q^2\right) \left(\left(1 + \frac{T_e}{T_i}\right) \frac{\nu_{ei} Z^2}{\mu^2 \Omega_i} \right. \tag{3.13}$$

with the safty factor $q = 7$ the ion temperature $T_i = T_e$ for the collisions and $\Omega_i = ZeB/m_i$ the ion cyclotron frequency with effective charge Z and ion mass m_i. The electron ion collisionality is the rate of collisions between ions and electrons and is given by

$$\nu_{ei} = \frac{n_0 Z^2 e^4 \Lambda}{3\sqrt{m_e}\epsilon_0^2 \pi^{\frac{3}{2}} \hat{T}^{\frac{3}{2}}} \tag{3.14}$$

with ϵ_0 the electric permitivity in vacuum, $\hat{T} = 40\,\mathrm{eV}$ the normalisation temperature and Λ is the Coulomb logarithm. π is also known as Archimedes' constant and ≈ 3.14. g is the effective gravity constant playing the role of magnetic curvature. g is related to the major radius R_c which is set to 1.5 m thus $g = \frac{2}{R_c} \approx 1.33\,\mathrm{m}^{-1}$. The terms C_α, which contain g, are drive terms. In the code, calculating the neutrals term N_n is the responsibility of the neutrals code, the STORM equation for density only request the term from the neutrals model, using an API call `neutrals->getDensitySource()` which is then added to the right hand side of the time derivative of the electron continuity equation. Γ^{ion} is the ionisation rate, Γ^{rec} is the recombination rate and Γ^{CX} is the charge exchange rate. The equation for the parallel electron velocity V is

$$\frac{\partial V}{\partial t} = A_V^{\perp} + A_V^{\parallel} + B_V + \Phi_V + P_V + F_V + T_V + N_V \tag{3.15}$$

$$A_V^{\perp} = \frac{\nabla\phi \times \vec{b}}{B} \cdot \nabla V \tag{3.16}$$

$$A_V^{\parallel} = -V\nabla_{\parallel} V \tag{3.17}$$

$$B_V = \mu_{\parallel}\nabla_{\parallel}^2 V \tag{3.18}$$

$$\Phi_V = \mu\nabla_{\parallel}\phi \tag{3.19}$$

$$P_V = -\frac{\mu}{n}\nabla_{\parallel} nT \tag{3.20}$$

$$F_V = \mu\nu_{\parallel}(U - V) \tag{3.21}$$

$$T_V = -0.71\mu\nabla_{\parallel} T \tag{3.22}$$

$$N_V = -\frac{V}{n}\Gamma^{\mathrm{ion}} \tag{3.23}$$

with the ion-electron mass ratio $\mu = m_i/m_e$. The parallel ion-electron resistivity is given by [144] $\nu_\parallel = \nu_{ei} n T^{-\frac{3}{2}}$ and is the cause of the friction term F_α. The viscous term B_V with the viscosity $\mu_\parallel$ was introduced to improve the numerical stability, with the magnitude $\hat{\mu}_\parallel = 1600 m^2 s^{-1}$ or in Bohm units $\mu_\parallel = 20$ well below the Braginskii level [10], as the full Braginskii level strongly flattens the acceleration within the flux tube and is thus unphysical. The electro static term Φ_α is due to parallel electric fields. The pressure term P_α is caused by the electron pressure $P_e = T_e \cdot n$. The T_α term is due to thermophoresis, and N_α is as mentioned before due to neutrals. The equation for the parallel ion velocity U

$$\frac{\partial U}{\partial t} = A_U^\perp + A_U^\parallel + \Phi_U + F_U + T_U + N_U + B_U \tag{3.24}$$

$$A_U^\perp = \frac{\nabla\phi \times \vec{b}}{B} \cdot \nabla U \tag{3.25}$$

$$A_U^\parallel = -U \nabla_\parallel U \tag{3.26}$$

$$\Phi_U = -\nabla_\parallel \phi \tag{3.27}$$

$$F_U = -\nu_\parallel (U - V) \tag{3.28}$$

$$T_U = +0.71 \nabla_\parallel T \tag{3.29}$$

$$N_U = \frac{v_n - U}{n} \Gamma^{\text{ion}} + \frac{v_n - U}{n} \Gamma^{\text{CX}} \tag{3.30}$$

$$B_U = \mu_\parallel \nabla_\parallel^2 U \tag{3.31}$$

the equation for the electron temperature T

$$\frac{\partial T}{\partial t} = A_T^\perp + A_T^\parallel + Q_T + T_T + B_T + F_T + C_T + N_T \tag{3.32}$$

$$A_T^\perp = \frac{\nabla\phi \times \vec{b}}{B} \cdot \nabla T \tag{3.33}$$

$$A_T^\parallel = -V \nabla_\parallel T \tag{3.34}$$

$$Q_T = -\frac{2}{3n}\nabla_\parallel q_\parallel \tag{3.35}$$

$$T_T = \frac{1.42}{3}(U-V)\nabla_\parallel T - \frac{2}{3}T\nabla_\parallel V \tag{3.36}$$

$$B_T = \frac{2}{3}\frac{\kappa_\perp}{n}\nabla_\perp^2 T \tag{3.37}$$

$$F_T = \frac{2}{3}\nu_\parallel (U-V)^2 + \frac{2}{3}\mu_\parallel \frac{V}{n}\nabla_\parallel^2 V \tag{3.38}$$

$$C_T = -\frac{2}{3}gT\frac{\partial \phi}{\partial y} - \frac{2}{3}g\frac{T^2}{n}\frac{\partial n}{\partial y} - \frac{7}{3}gT\frac{\partial T}{\partial y} - \frac{2}{3}gV^2\frac{1}{\mu n}\frac{\partial nT}{\partial y} \tag{3.39}$$

$$N_T = -\frac{T}{n}\left(\Gamma^{\text{ion}} + \Gamma^{\text{CX}}\right) - \frac{1.09T - 13.6\,\text{eV}}{n}\Gamma^{\text{rec}} - \frac{E^{\text{ion}}}{n}\Gamma^{\text{ion}} - R^{\text{imp}} \tag{3.40}$$

The parallel heat conduction term Q_T is depending on the parallel conduction coefficient [144]

$$q_\parallel = -\frac{2}{7}\kappa_0 \nabla_\parallel T^{\frac{7}{2}} - 0.71nT(U-V) \tag{3.41}$$

$$\kappa_0 = \frac{3.16\Omega_i}{\nu_{ei}} = \frac{3.16ZeB}{\nu_{ei}m_i} \tag{3.42}$$

The perpendicular transport coefficient $\kappa_\perp$ is given by [144]

$$\kappa_\perp = \frac{n^2}{T^{\frac{1}{2}}}(1+1.6q^2)4.66\frac{\nu_{ei}m_e Z^2}{\Omega_i m_i} \tag{3.43}$$

The first term in N_T is as by both charge exchange and ionisation a new ion enters the bulk, thus reducing the temperature. The second term stems from recombination, and the 13.6 eV is the energy released during recombination assuming three-body recombination where the energy is transfered to the plasma rather than emitted as a photon. The factor of 1.09 is chosen such that the recombination process heats the plasma below 5.25 eV [145, 146]. E^{ion} is the energy required to ionise an atom and is here assumed to be 30 eV [146]. The impurity radiation R^{imp} is using the carbon radiation model from Hutchinson [147] using an impurity fraction of 1 %. The radiation seems to have only a minor impact, and is not responsible for the total plasma pressure drop in front of the target. The equation for the vorticity ω is derived from charge balance, and thus currents are important for the derivation. The equation is given by

$$\frac{\partial \omega}{\partial t} = A_\omega^\perp + A_\omega^\parallel + J_\omega + B_\omega + C_\omega + N_\omega \tag{3.44}$$

$$A_\omega^\perp = \frac{\nabla\phi \times \vec{b}}{B} \cdot \nabla\omega \tag{3.45}$$

$$A_\omega^\parallel = -U\nabla_\parallel \omega \tag{3.46}$$

$$J_\omega = \nabla_\parallel (U - V) + \frac{U - V}{n}\nabla_\parallel n \tag{3.47}$$

$$B_\omega = \mu_\omega \nabla^2 \omega + \nabla_\perp \mu_\omega \cdot \nabla_\perp \omega \tag{3.48}$$

$$C_\omega = \frac{g}{n}\frac{\partial nT}{\partial y} \tag{3.49}$$

$$N_\omega = -\frac{1}{n}\nabla_\perp^2 \phi(\Gamma^{\text{CX}} + \Gamma^{\text{ion}}) - \frac{1}{n}\nabla_\perp \phi \cdot \nabla_\perp (\Gamma^{\text{CX}} + \Gamma^{\text{ion}}) \tag{3.50}$$

The advection contribution A_ω are caused by the frame of reference - as if the plasma moves, the drifts are with respect to the plasma, rather than the lab. As will be shown later, these terms are small, especially the parallel advection term is mostly negligable. The diffusive term B_ω is due to the viscosity of the plasma, and is assumed to be neo-classical level, and thus μ_ω is given by [144]

$$\mu_\omega = (1 + 1.6q^2)\frac{6}{8}\frac{\rho_i^2 n Z^4 \Lambda}{\sqrt{m_i}\epsilon_0^2 3(2\pi T_i)^{1.5}} \propto \frac{n}{T^{\frac{1}{2}}} \tag{3.51}$$

Due to the density and temperature dependence, this term is especially important in the case of high density and low temperature, as will be seen in the analysis of the detached simulations. In the vorticity equation the current term J_ω is responsible for conducting vorticity in parallel direction, and is in general more important than the advection terms A_ω, as will be shown in the analysis of the simulations. The drive term C_ω is due to the slab approach, where the field lines are streched out, and the terms C_α is to reintroduce the curvature effect in the system. The neutrals provide a frictional force [148], and as the neutrals only have a velocity in parallel direction, the perpendicular component is zero, and the neutrals provide only a dampening term.

The cross field transport coefficients are calculated self consistently, following the derivation of Fundamenski et al. [126, 144].

3.3.3 Geometry and boundary conditions

As STORM is using the BOUT++ library, it can be run using a full tokamak geometry. However, the version used here is run in a slab geometry, thus the drive terms are introduced to capture the curvature drive. A draw-

ing of the geometry is shown in fig. 3.2. The Cartesian slab represents a flux tube in a full tokamak geometry. z being the coordinate parallel to the magnetic field, $z = 0$ represents the mid-plane, and reaches to $z = L_{\parallel} = 10\,\mathrm{m}$ to the target, which is modelled by sheath boundary conditions. $z = 0$ acts as a symmetry plane for the simulation. This is a plane orthogonal to the magnetic field. The radial direction is in x direction, and the bi-normal direction is called y. Note that in the code z and y are swapped, but this convention is used to be consistent with the notation used in literature. For all simulations presented here, a uniform mesh was used. The parameters, such as the parallel connection length $L_{\parallel} = 10\,\mathrm{m}$ as well as the magnetic field $B = 0.5\,\mathrm{T}$ are representative for MAST, see sec. 1.5.4.

In the radial direction Neumann boundary conditions with zero gradient are enforced, with the exception of ω and ϕ, which are set to respective background values. The y direction is periodic for all quantities. At the symmetry plane the velocities U and V are set to zero, whereas for the other quantities zero gradients are enforced. At the target magnetic pre-sheath boundary conditions were set. The ions need to reach the speed of sound $U = \sqrt{T}$, and the electrons have to reach at the sheath boundary

$$V = \sqrt{T}\exp(-V_f - \frac{\phi}{T}) \tag{3.52}$$

where V_f is the floating potential. The heat flux at the target is give by

$$q_{\parallel}|_{\mathrm{sheath}} = (2 - V_f)\, nTU - 2.5ntV - \frac{1}{2\mu}nV^3 \tag{3.53}$$

The neutral density is forced to have a vanishing gradient at the target boundary and the neutrals velocity needs to vanish at the sheath. The plasma density and temperature is set to free, i.e. extrapolated into the

boundary without restriction.

3.3.4 Backgrounds

Before the filament can be seeded, a background is needed onto which the filament can be added, which is described in sec. 3.3.5. The backgrounds are only retaining the parallel dependence, and uniformity in the radial and bi-normal direction is assumed. Thus the backgrounds are 1D along z. The backgrounds are evolved using the above equations (3.7) to (3.50). Due to the uniformity, perpendicular terms can be dropped for computational efficiency. This also implies that the backgrounds are turbulence free. The profiles are fuelled by an density and temperature source which is located at the mid-plane, and have an exponentially decaying shape.

For the fuelling either a prescribed rate was used, or a specific upstream value for density and temperature was used, and the fuelling was controlled with a proportional-integral-derivative (PID) controller. A PID controller sets the influx as a function of the instantaneous difference to the predefined value, the integral and the derivative of the difference. It is a commonly used control loop feedback mechanism.

3.3.5 Filament seeding

Filament seeding describes the process of adding a pressure perturbation on top of an otherwise unperturbed background [32]. The alternative to seeded filament simulations, is to evolve a fully turbulent system, in which filaments are born self consistently, in order to study filament dynamics. Fully turbulent systems allow for example to also study the occurrence rate. Seeded filaments on the other hand, are computationally much less

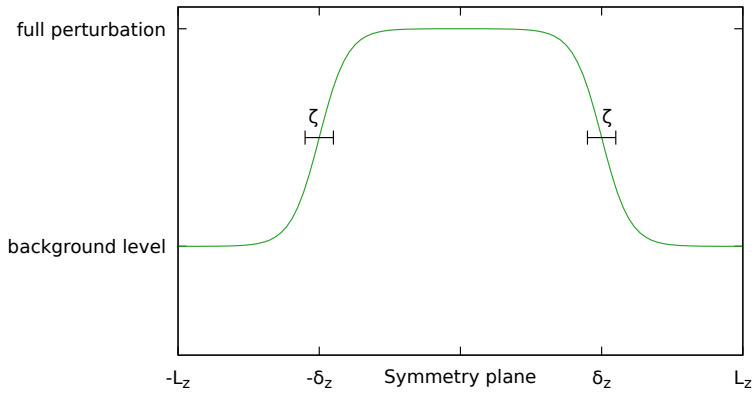

Figure 3.3: Plot of eq. (3.54) with $\delta_z = L_z/2$ and $\zeta = L_z/10$.

demanding. They also allow a fine control on various parameters, such as perpendicular size or amplitude.

STORM uses a tanh shape for the seeded filament in the parallel direction. The full functional dependence is

$$\frac{1 - \tanh((z - \delta_z)/\zeta)}{2} \tag{3.54}$$

where δ_z is the half length of the filament in the parallel direction. The full length is $2\delta_z$, due to the symmetry of the system in parallel direction and can also be seen in fig. 3.3. ζ is the length over which the filament decays to the background value. Due to the symmetry, only half of the dommain is simulated.

In the perpendicular direction a Gaussian shape is used:

$$\exp\left(\frac{x^2 + y^2}{\delta_\perp^2}\right) \tag{3.55}$$

where $\delta_\perp$ is the perpendicular width of the filament, x is the radial direction and y is the bi-normal direction. Note that STORM has also been used for non-circular filaments [111], as part of this thesis only circular filaments

have been seeded.

The filamentary perturbation has been added on top of the 1D profiles described in sec. 3.3.4. This has been done such that the upstream perturbation is constant, i.e. the amplitude of the filament was equal to the upstream value of the background $\Theta_0(z = 0)$. This results in the initial state of the perturbed field Θ

$$\Theta(x, y, z) = \Theta_0(z) + \Theta_0(z = 0) \exp\left(\frac{x^2 + y^2}{\delta_\perp^2}\right) \frac{1 - \tanh((z - \delta_z)/\zeta)}{2} \quad (3.56)$$

Only the density n and the temperature T were perturbed. The other fields were initialised unperturbed and had to adjust to the perturbed density and temperature.

3.4 Neutrals model

As part of this PhD two neutrals models have been developed. One purely diffusive, introduced in sec. 3.4.1, and one including parallel velocity, introduced in sec. 3.4.2. The API of the neutral code is introduced in appendix B.

3.4.1 Diffusive neutral model

The diffusive neutral model evolves the atomic neutral density n_n. The neutrals are transported thereby only by diffusion:

$$\frac{\partial n}{\partial t} = \mu_n \nabla^2 n_n + (\nabla \mu_{n_n}) \cdot (\nabla n_n) + \Gamma^{\text{rec}} - \Gamma^{\text{ion}} + S_R - f_l n_n \quad (3.57)$$

Note that the the term $(\nabla \mu_{n_n}) \cdot (\nabla n_n)$ is missing in the simulations performed in chapter 5 but no significant impact is expected from the omission.

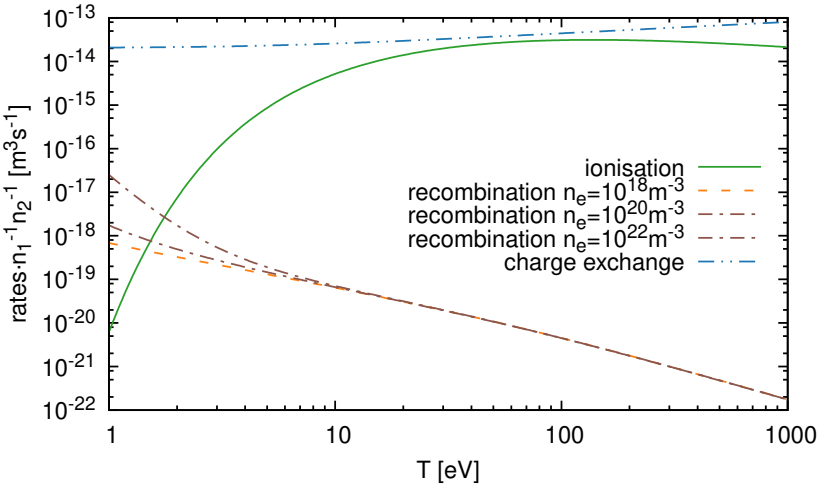

Figure 3.4: Plot of the neutrals rates fitted by Willet [58]. The recombination rates have a density dependence for low temperatures.

The ∇^2 is the full 3D Laplacian, although in the 1D simulations only the parallel contribution is retained. The rates are shown in fig. 3.4 and have been fitted by Willett [58].

In the equation for the neutral density, μ_{n_n} is the neutral diffusion, given by [125, 126, 149, 150]

$$\mu^0_{n_n} = \frac{v^2_{th}}{v_{th}\sigma n_n + \Gamma^{\mathrm{CX}} + \Gamma^{\mathrm{ion}}} \tag{3.58}$$

$$\mu_{n_n} = \begin{cases} \mu^0_{n_n} & \text{if } \mu^0_{n_n} \geq 2D^0 \\ \mu^0_{n_n}/2 + D^0 & \text{if } \mu^0_{n_n} < 2D^0 \end{cases} \tag{3.59}$$

with v_{th} deuterium's thermal speed at 300 K and the atomic deuterium-deuterium cross section $\sigma = \pi(52.9\,\mathrm{pm})^2$. The diffusion term $\mu^0_{n_n}$ is based on the step-size L and collision frequency τ of the neutrals, thus $\mu^0_{n_n} = L^2\tau$. L is given by the thermal speed v_{th}/τ. The collision frequency is the sum of the neutral-neutral collsions $v_{th}\sigma n_n$ as well as the charge-exchange and ionisation frequency.

The diffusion limiter D^0 is needed to compensate for the lack of pressure in high neutral density regions, in which case an unphysically high diffusion occurs. The term $f_l n_n$ emulates cross field losses. Recycling of the neutrals is proportional to the particle flux at the target $f_T = nU|_{\text{target}}$, the recycling coefficient $f_R = 0.9$ and depends on a Gaussian recycling falloff length $L_R = 4\,\text{m}$:

$$S_R = \alpha_R \frac{f_R}{f}_T \exp(-z^2/L_R^2) \tag{3.60}$$

where α_R is a normalisation constant, ensuring that a fraction f_R of the target flux f_T are recycled along the field line. This non-local model was chosen, as the lack of pressure combined with high neutral densities near the target results in low return fluxes of particles back along the field line. This non-local recycling model combined with a limiter for the neutral diffusion μ_{n_n} ensures that the neutrals are transported from the target up stream. The recycling model is an extension of the density source previously used in STORM [22, 113, 121]. In STORM previously an exponential function was used to redistribute the neutrals. However, the exponential function has a steep gradient near the target. Thus for short falloff length $L_R \sim d_\parallel$, this introduces a dependence on the grid size $d_\parallel$, as for finer grids recycling is located closer towards the target. A Gaussian was chosen instead, as it does have a vanishing gradient at the target, and decays further upstream.

Table 3.1 shows the parameters that can be set in the diffusive model of the neutrals-API.

Table 3.1: Options of the diffusive neutrals model.

Option	Description
`equi_rates`	Are steady state rates used from background calculations? Default: false
`recycling_falloff`	Falloff length L_R over which the neutrals are recycled Default: 4.0 Units: m
`lower_density_limit`	The minimum neutral density enforced Default: $8 \cdot 10^{10}$ Units: m^{-3}
`higher_density_limit`	The maximum neutral density enforced Default: $4 \cdot 10^{19}$ Units: m^{-3}
`recycling_fraction`	Faction of the target ion flux that is recycled Default: 0.9
`loss_fraction`	Fraction of neutrals f_l that are lost per time unit. This has the same units as the physics model. Default: 10^{-5} Units: same as physics model
`diffusion_factor`	Factor to enhance diffusion of neutrals to compensate that neutrals are not bound by magnetic field lines Default: 10.0

Table 3.1: Options of the diffusive neutrals model.

Option	Description
`onlyion`	Do we exclude charge-exchange and recombination? Can be used to reduce the impact of the neutrals model. Default: false
`use_log_n`	Evolve the logarithm of the density, rather than the density. This is discussed in more detail in 3.4.2. Default: false
`density_source:function`	Additional density source for the neutrals. Units are the same as the physics model. Default: 0 Units: same as phyics model
`impurity_fraction`	The fraction of carbon impurity with respect to the plasma density. Default: 0
`density_name`	Name of the neutral density. Can be changed in case the post processing script expects a different name. Default: neutral_density
`T_n`	Temperature of the neutrals. In diffusion neutral model, T_n influences the diffusion constant. The units can be set with the Default: 300 K `temperature_unit` option.

Table 3.1: Options of the diffusive neutrals model.

Option	Description
`temperature_unit`	Units of the temperature. "K" and "kb" refer to the Boltzmann constant, "eV" switches to electron volts, and "default" selects the temperature used by the physics model internally. Default: K

3.4.2 Parallel neutral model

The `type=parallel` neutrals model evolves in addition to the neutral density also a field aligned neutral momentum. The choice to evolve the parallel momentum allows one to conserve momentum in the neutral plasma interaction. The intent of this neutral model was allowing to support simulations in detached conditions, where a significant amount of momentum from the plasma is transferred to neutrals.

The equations for the neutrals are the density equation, which now reads

$$\frac{\partial n_n}{\partial t} = -\nabla m_n + \Gamma^{\mathrm{rec}} - \Gamma^{\mathrm{ion}} + S_R - f_l n_n + \frac{\partial}{\partial z}\left(\mu_{n_n}\frac{\partial}{\partial z} n_n\right) \tag{3.61}$$

and the equation for the parallel momentum m_n

$$\begin{aligned}\frac{\partial m_n}{\partial t} = &-v_n \nabla_\parallel m_n - m_n \nabla_\parallel v_n - \nabla_\parallel \left(T_n n_n\right) + \Gamma^{\mathrm{CX}}(U - v_n) \\ &+ \Gamma^{\mathrm{rec}} U - \Gamma^{\mathrm{ion}} v_n + \alpha_{m_n}\frac{\partial^2}{\partial z^2} m_n - S_R v_{th}\end{aligned} \tag{3.62}$$

where v_n is the parallel neutrals velocity, U is the ion velocity, α_{m_n} is a momentum diffusion constant which is required for numerical stability at

the onset of detachment. The thermal velocity of the neutrals is v_{th} and the temperature T_n, assumed to be 3 eV.

The parallel neutral model is internally based on the diffusion model, and inherits the options described in table 3.1. The only new option is the name of the parallel momentum, see table 3.2.

While also the diffusive neutral model supports evolving the logarithm of the density, rather than the density itself, this feature has been implemented in order to allow detached simulations. Evolving the logarithm ensures in a natural way that the value stays positive. In addition if implicit solvers are used, this influences the error norm, as relative small changes near zero in real space result in large differences in log space, thus increasing the accuracy of the solver for these values.

Table 3.2: Options of the parallel neutrals model, in addition to the ones from the diffusion neutrals model shown in table 3.1.

Option	**Description**
`momentum_name`	Name of the neutral momentum. Can be changed in case the post processing script expects a different name. Default: m_n

3.5 Analysis of simulation results

In order to analyse the simulation, the data was processed. In this section some of the applied methods are introduced.

3.5.1 Filament velocity

The simulations calculate the evolution of density, but the radial velocity of the filament is of interest, not the full density evolution. In order to calculate the filament velocity, different methods can be used [96, 137]. As we are interested in the density transport, the centre of mass (COM) was chosen to calculate the position $\vec{c}$ of the filament for a slice in the perpendicular direction z:

$$c_x(z) = \frac{\int\int x\Delta n(x,y,z)\,\mathrm{d}x\,\mathrm{d}z}{\int\int \Delta n(x,y,z)\,\mathrm{d}x\,\mathrm{d}z} \tag{3.63}$$

$$c_y(z) = \frac{\int\int y\Delta n(x,y,z)\,\mathrm{d}x\,\mathrm{d}z}{\int\int \Delta n(x,y,z)\,\mathrm{d}x\,\mathrm{d}z} \tag{3.64}$$

with

$$\Delta n(x,y,z) = \begin{cases} n(x,y,z) - n_{\mathrm{cut}}(z) & \text{for } n(x,y,z) - n_{\mathrm{cut}}(z) > 0 \\ 0 & \text{else} \end{cases} \tag{3.65}$$

where the cut-off density n_{cut} was computed by taking the average of the background density and the peak density amplitude of the cross-section plane. In general the filaments studied were rigid, unless otherwise specified the mid-plane COM is used, i.e. $\vec{c} = \vec{c}(z = 0\,\mathrm{m})$.

The radial filament velocity v_r can thus be calculated by taking the time derivative of the radial position

$$v_r = \frac{\partial}{\partial t} c_x \tag{3.66}$$

3.5.2 Vorticity contribution

In order to study the driving changes for the filament dynamics, the contributions of the different terms in the vorticity equation is analysed. Therefore the time derivative of the vorticity was calculated and the various contributions, as introduced in sec. 3.3.2 were analysed. The contributions were recalculated using the python interface of BOUT++, that was developed for this purpose and is introduced in appendix C.1. This allows to recalculate the terms in the post processing step using the implementation of BOUT++.

Similar to the filaments radial velocities, the data was analysed where the filaments are at peak velocity. In order to further reduce the the amount of data, each 2D slice d in the perpendicular plane was projected onto a set of physically motivated basis vectors $e_{i,j}$.

The basis vectors $e_{i,j}$ where centred on the COM of the filament, and periodicity in y was taken into account such that the branch-cut was at $y_{\text{cut}} = c_y \pm \frac{1}{2} L_y$. The non-normalised, non-orthogonal vectors $\tilde{e}_{i,j}$ are defined as:

$$\tilde{e}_{i,j} = (x - c_x)^i (y - c_y)^j \exp\left(\frac{(x - c_x)^2 + (y - c_y)^2}{\delta_\perp^2}\right) \tag{3.67}$$

and after orthogonalisation the vectors $\tilde{\tilde{e}}_{i,j}$

$$\tilde{\tilde{e}}_{i,j} = \tilde{e}_{i,j} - \sum_{(i',j')<(i,j)} \tilde{e}_{i,j} \cdot e_{i',j'} \tag{3.68}$$

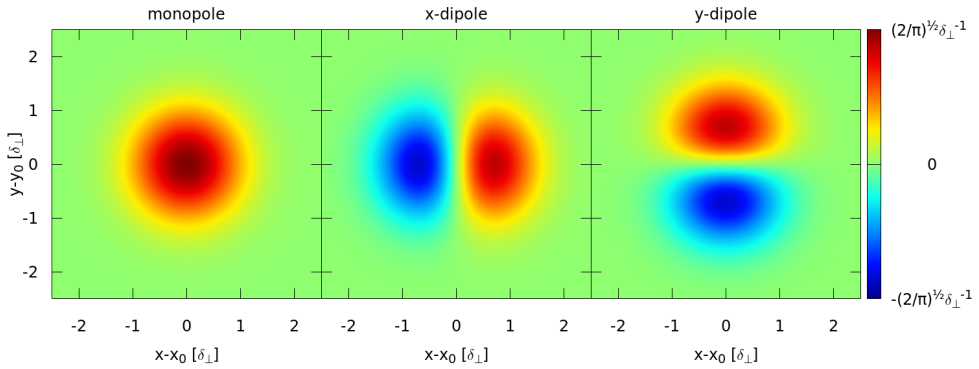

Figure 3.5: The first three base vectors, representing monopole, radial bipole and bi-normal dipole.

where the $<$ operator implies an ordering of the pairs, such as $(0,0)$ $(1,0)$ $(0,1)$ $(2,0)$ $(1,1)$ $(0,2)$ ...which does exist as $\mathbb{N}^2$ is countable. The dot product $\tilde{e}_{i,j} \cdot e_{i',j'}$ entails an integral over the product of the two functions. The base vector $e_{i,j}$ is obtained after normalisation:

$$e_{i,j} = \tilde{\tilde{e}}_{i,j} \left(\tilde{\tilde{e}}_{i,j} \cdot \tilde{\tilde{e}}_{i,j} \right)^{-\frac{1}{2}} \tag{3.69}$$

The data d can be projected onto the basis vectors, thus we get the data components $d_{i,j}$ for each slice in z:

$$d_{i,j}(z) = e_{i,j} \cdot d = \int \int e_{i,j}(x,y) d(x,y,z) \, \mathrm{d}x \, \mathrm{d}y \tag{3.70}$$

Probably the most interesting component is the (0,1) component, which represents a dipole in bi-normal direction. This creates an $E \times B$ force in the radial direction, and is thus related to the radial drive. Due to the sign of the definition in (3.67), a positive radial drive requires a negative (0,1) component in the vorticity. The other two moments that have been analysed are the (0,0) component, that represents the monopole contribution,

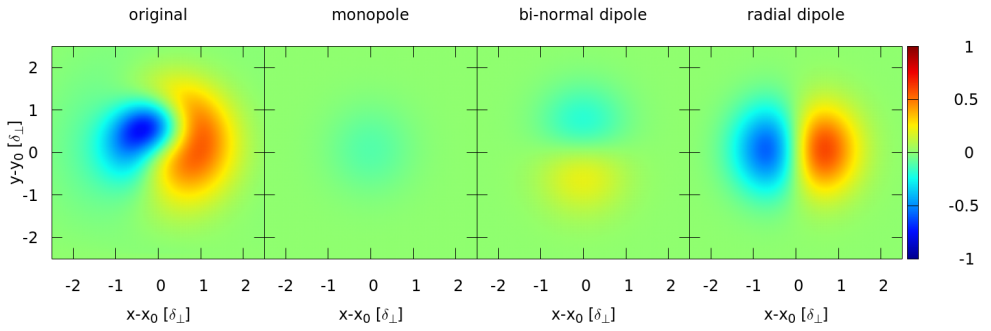

Figure 3.6: Some 2D simulation data and its projection on the three base vectors shown in fig. 3.5.

and the (1,0) component, that in turn describes a dipole in radial direction. A monopole in the vorticity field is causing a monopole potential, and thus via $E \times B$ a spinning motion [113]. The (1,0) component, or dipole in radial direction causes a motion in bi-normal direction. Fig. 3.5 shows the first 3 base vectors used.

This decomposition is an extension of the odd parts / even parts split used by Walkden et al. [113], that allows one to do this not only for a few slices, but along the whole filament. This is required to show parallel dynamics within the filament. The choice to include a Gaussian and not just using a 2D version of the Chebyshev polynomials, is that Chebyshev polynomials would weight a perturbation far outside the filament stronger, than close to the filament, even though they would have basically no impact on the filament, as the density perturbation is not aligned with the vorticity source. Additionally, as the perturbation moves across the cut-off, the polynomial changes sign, and this small, unimportant change could impact the result significantly. Fig. 3.6 shows an example decomposition of some simulation data on the three basis vectors shown in fig. 3.5. In this case the main contribution is the radial dipole. Monopole as well as bi-normal

dipole have a lower absolute amplitude than the radial dipole.

The decomposition of the time derivative of the vorticity terms is applied at the time where the filaments reach peak velocity. This is done in order to study which contributions are important for a given filament, in order to close/create the vorticity. This does however not represent how much vorticity has been created, because at that point the source and sink terms are roughly in balance. Thus even if e.g. the viscosity would be a very inefficient sink, but the other ones are even smaller, than the sink will at some point balance the source, given that the filament is not significantly advected. In addition to allowing to distinguished what terms are of relative importance, it allows one to give insight into the parallel distribution of the source and sink terms. Due to the specific choice of base vectors, it also allows one to distinguish dipole and monopole terms.

CHAPTER 4

Background Profiles

In order to study the influence of self consistent backgrounds on the dynamics of filaments, a procedure for producing such backgrounds is needed. Self consistencent backgrounds is here defined as the steady state solution to the used model equations. This includes physically motivated source terms for density and energy. Further the rates are physcically motivated and calculated with dependence on the locale state of the plasma, e.g. the local plasma density or electron temperatures. Using self consistent backgrounds helps with the comparison of experiments and simulations, as otherwise certain effects might be discovered, that are not as pronounced in experiments, or other effects that are important in experiments are shadowed by the inconsistencies in the simulation. Once the backgrounds are generated, the filaments are seeded on these backgrounds, as described in sec. 3.3.

4.1 Introduction and Generation

The backgrounds discussed here are an extension of the Two-point model, as introduced in sec. 1.5.1, in the respect that they only retain the parallel direction, but no radial dependencies. As such the backgrounds where generated by assuming radial and bi-normal uniformity.

The backgrounds for the filament simulation where obtained by running STORM to steady state. As the backgrounds where calculated numerically, the steady state solution is approximated by running the system for a long time, until the change within the last 20 % of the total runtime is less than 1 % of the value. An exception to that is the neutral velocity, where the accuracy was limited by the limited accuracy of the solver, as absolut value of the velocity was very small, thus small changes resulted in large changes in the neutral velocity. As the simulation for generating the backgrounds has been running much longer than for the filament simulations, the small remaining dynamic of the background can be neglected on the timescale of the filament dynamic. As no radial dependence, and no turbulence was included, the system was modelled only retaining the parallel dimension.

The upstream density source, as well as energy influx were controlled, and the rest of the system was evolved self-consistently to steady state. Due to the symmetry in the perpendicular plane, perpendicular terms in the STORM equations introduced above could be dropped without any influence. Due to quasi-neutrality of the plasma, the divergence of the current needs to be zero, and in combination with the boundary conditions, that implies that the current needs to be zero, i.e. $U = V$.

As such also the time derivatives of the two quantities can be set equal,

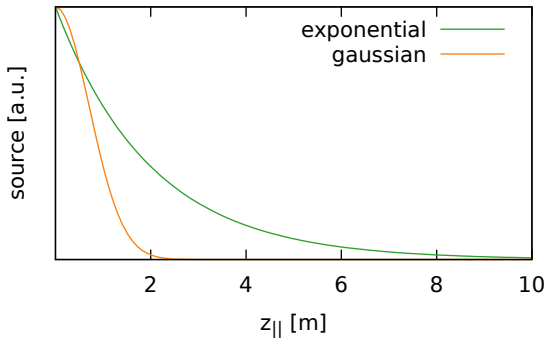

Figure 4.1: Shape of the source terms for energy and density. On the left hand side at $z_\parallel = 0$ is the mid-plane which acts as a symmetry plane. On the right hand side at $z_\parallel = 10\,\mathrm{m}$ is the target.

$\frac{\partial U}{\partial t} = \frac{\partial V}{\partial t}$ and the equation can be solved for the potential ϕ. This yields:

$$\nabla_\parallel \phi = 0.71 \nabla_\parallel T - \frac{U\Gamma^{\mathrm{ion}} + U\Gamma^{\mathrm{cx}} + V\Gamma^{\mathrm{ion}}}{n(1+\mu)} + \frac{\mu}{1+\mu}\frac{\nabla_\parallel p}{p} \tag{4.1}$$

which can be integrated starting from the target, where ϕ is prescribed from the Bohm boundary condition to be current free, i.e. $\phi_s = -V_f T$ with V_f the floating potential:

$$\phi(z) = -V_f T + \int_{L_\parallel}^{z} 0.71 \nabla_\parallel T - \frac{U\Gamma^{\mathrm{ion}} + U\Gamma^{\mathrm{cx}} + V\Gamma^{\mathrm{ion}}}{n(1+\mu)} + \frac{\mu}{1+\mu}\frac{\nabla_\parallel p}{p}\,\mathrm{d}z \tag{4.2}$$

The energy and temperature influxes were of exponential shape, that peaked at the mid-plane, as shown in fig. 4.1. Depending on whether the 1D simulation was run in constant temperature or energy influx mode, either a constant, prescribed energy influx was used, while in the case of a constant temperature, the energy influx was controlled with a PID controller to reach the prescribed value. Similarly, the density influx was controlled with a PID

controller to reach a prescribed density. In the case of the density in some cases the gaussian shape was used. The PID controller sets the influx as a function of the instantaneous difference to the predefined value, the integral and the derivative of the difference. A PID controller is a commonly used control loop feedback mechanism. For the 3D simulation the controller is replaced by the steady state value of the background simulation. While setting the value via a Dirichlet boundary condition would be easier in the case of the background profiles, the influx needed for maintaining the background is not known that way. This causes issues for the filament simulations, as a Dirichlet boundary condition would interact non-trivially with the seeded filament. Further, a Dirichlet boundary condition would concentrate all the influx in a single point, instead of spreading it.

The initial simulations are run with $n_z = 64$ points in the parallel directions, while the simulations in the detached cases, shown in sec. 4.4, are run on a refined grid with $n_z = 480$ points. The initial simulations in attached conditions are run with a simplified neutral model, that does not include a parallel neutral momentum. Instead the diffusion constant is limited to ensure transport of the neutrals from the target towards upstream. The limiter for the diffusion constant is introduced in sec. 3.4.1. In the detachment study presented in chapter 6 a carbon fraction of 1 % of the plasma density was assumed, while in the initial study presented in chapter 5 no impurities where included.

4.2 Low recycling

For sufficient low plasma densities and sufficient high temperatures, the backgrounds are in the low recycling regime. The low recycling regime

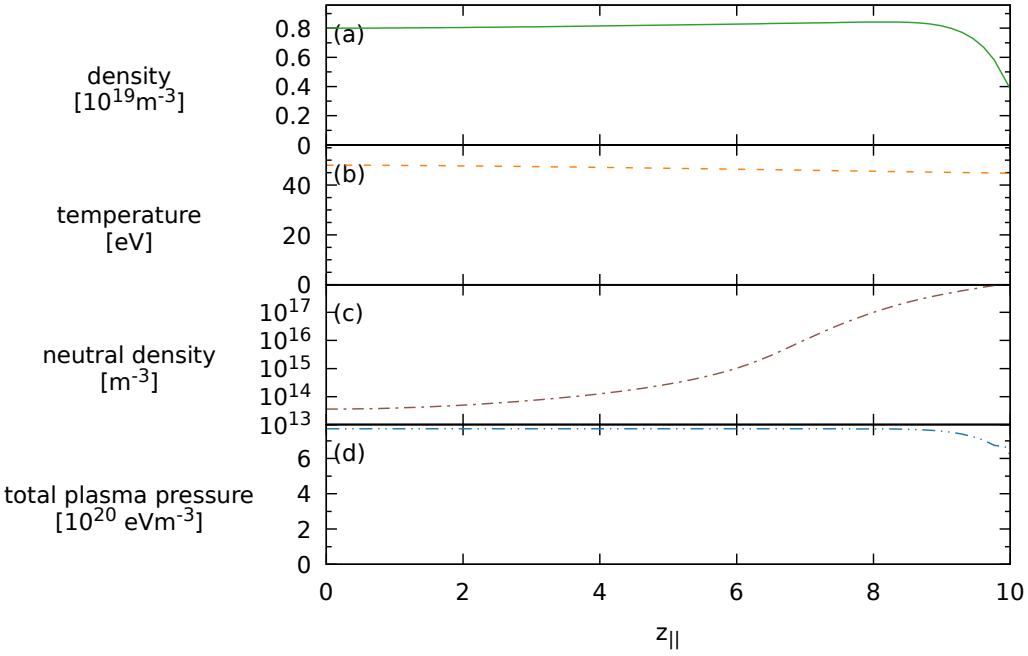

Figure 4.2: Background plasma profile, run to steady-state for a set upstream temperature $T_0 = 48\,\mathrm{eV}$ and density $n_0 = 8 \cdot 10^{18}\,\mathrm{m}^{-3}$. The sheath is at the right hand side at $L = 10\,\mathrm{m}$. The mid-plane is at the left hand side, and is a symmetry plane. From top to bottom are plotted the plasma density n, electron temperature T_e, the neutral density n_n and the total plasma pressure P_p versus the parallel connection length. Note that the neutral density is plotted on a log scale, while the other quantities are plotted on a linear scale.

is also called sheath limited regime [44], however in this discussion the name low recycling regime is preferred, to avoid confusion with the sheath limited scaling for filaments, where currents are closed via sheath currents, see sec. 2.2.4.

An example of background profile in the low recycling regime is shown in fig. 4.2. Typically for the low recycling regime, the temperature profile, shown in fig. 4.2(b) is quite flat. This is caused by the high conduction of the hot, low density plasma. The plasma density, shown in fig. 4.2(a) is also

mostly flat, and only drops in front of the target. The neutral density, shown on a log scale in fig. 4.2(c), is strongly peaked on the target at the right hand side, and drops off towards the mid plane, where diffusion increases and the profile become flatter. The total plasma pressure, i.e. sum of the static plasma pressure $n \cdot T$ and dynamic pressure $\frac{1}{2}n \cdot V^2 + \frac{1}{2}n \cdot U^2 = n \cdot V^2$ is shown in fig. 4.2(d). The drop in front is due to charge-exchange of the neutrals with the plasma, by absorbing parallel momentum and thus pressure, as in the case without the pressure stays constant.

4.3 High recycling

With increasing density, the background profiles transition to the high recycling regime, as shown in fig. 4.3. A defining feature of the high recycling regime is the significant drop of the temperature towards the target, as is present in the shown fig. 4.3(b). As the temperature starts dropping towards the target, the density increases, as shown in fig. 4.3(a). This is required to preserve the total pressure in the flux tube, which is shown in fig. 4.3(d).

The neutral density is peaked at the target, and drops towards the mid-plane, shown in fig. 4.3(c). This is similar to the low recycling case (fig. 4.2(c)).

The transition from low to high recycling regime is a continuous process. The transition is shown in fig. 4.4. Thereby the different quantities, that in fig. 4.2 and 4.3 have been plotted separately are merged into a single sub-plot to allow a convenient comparison.

The temperature increases from left to right, where fig. 4.4(a) is the low temperature case of $T_0 = 12\,\mathrm{eV}$, which is also shown in fig. 4.3. The high

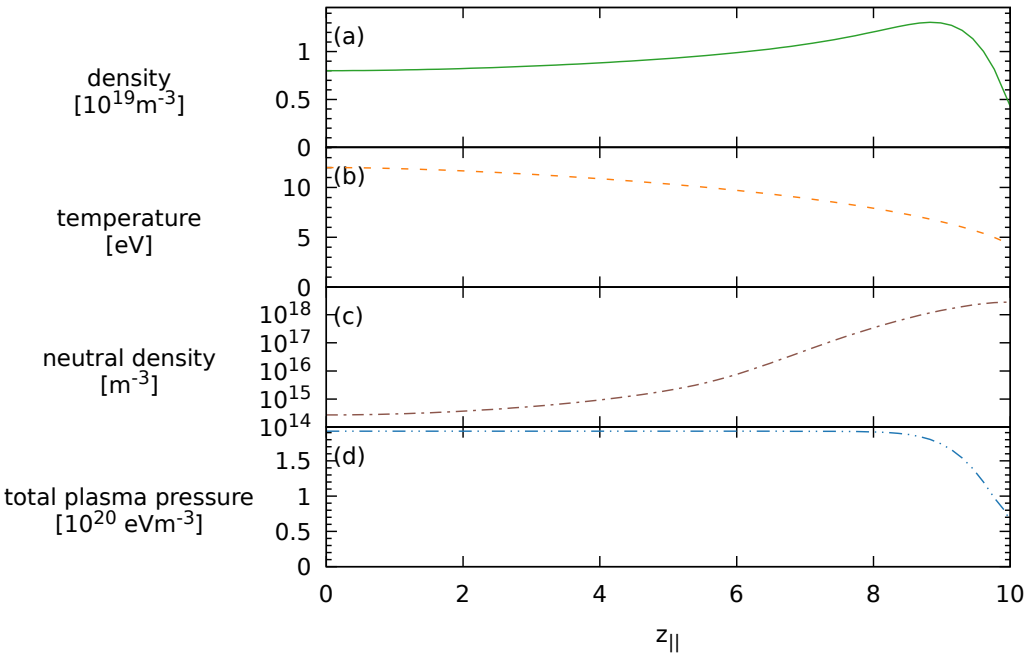

Figure 4.3: Background plasma profile, run to steady-state for a set upstream temperature $T_0 = 12\,\mathrm{eV}$ and density $n_0 = 8 \cdot 10^{18}\,\mathrm{m}^{-3}$. The sheath is at the right hand side at $L = 10\,\mathrm{m}$. The mid-plane is at the left hand side, and is a symmetry plane. From top to bottom are plotted the plasma density n, electron temperature T_e, the neutral density n_n and the total plasma pressure P_p versus the parallel connection length. Note that the neutral density is plotted on a log scale, while the other quantities are plotted on a linear scale.

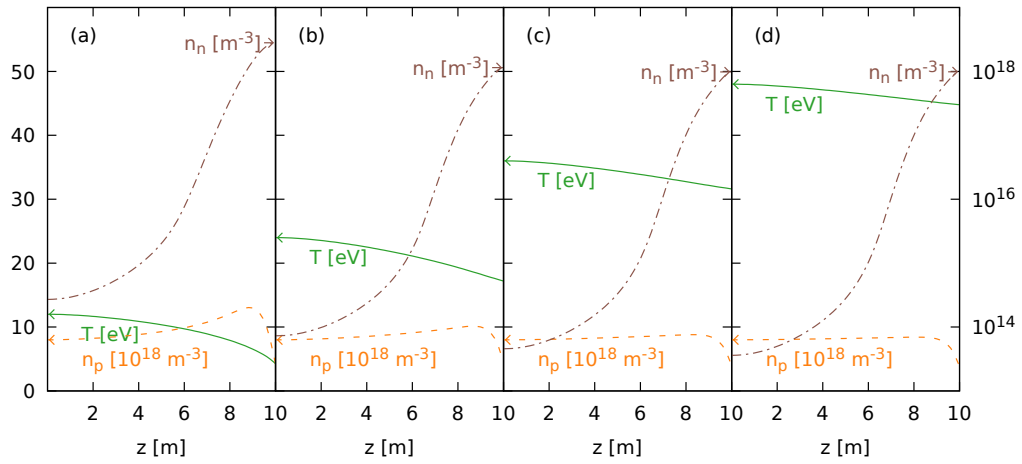

Figure 4.4: Background plasma profile, run to steady-state for a set upstream temperature (a) $T_0 = 12\,\mathrm{eV}$, (b) $T_0 = 24\,\mathrm{eV}$, (c) $T_0 = 36\,\mathrm{eV}$ and (d) $T_0 = 48\,\mathrm{eV}$ all with an upstream density $n_0 = 8 \cdot 10^{18}\,\mathrm{m}^{-3}$. The sheath is at the right hand side at $L = 10\,\mathrm{m}$. The mid-plane is at the left hand side, and is a symmetry plane. Plotted is in each case the plasma density n_p, the electron temperature T_e and the neutral density n_n. Note that the neutral density is plotted on a log scale on the right, while the other quantities are plotted on a linear scale on the left.

temperature case in fig. 4.4(d), is the low recycling case from fig. 4.2.

From left to right the temperature increases both upstream, and thus also in general. At the same time the temperature profiles become relatively flat. The density profiles as well become increasingly flat. The neutral density decreases with increasing density. The mid-plane density is decreasing continuously with increasing temperature, while the target neutral density only decreases initially, and stays roughly constant.

In addition to the temperature scan shown in fig. 4.4, fig. 4.5 extends the scan to higher densities. In the high density, low temperature case (fig. 4.5(a)) the temperature drops even stronger towards the target than in the low density case, (c).

In the high density, low temperature case the pressure drop is strongest. This coincides with a rather low target temperature, of only a few eV.

In order to understand the impact of neutrals on these backgrounds, the simulations have repeated while minimising the impact of neutrals, but keeping the fuelling mostly unchanged. This was achieved by retaining the neutrals, but only including ionisation, and not charge exchange and recombination. The resulting profiles are shown in fig. 4.6. In the high T_0, low n_0 case, in fig. 4.6(d) only a small deviation can be observed. The main difference is an increased neutral density and no pressure drop towards the target. The small remaining lack of pressure conservation along the flux tube is caused by numerical inaccuracies caused by discretisation and approximation of the infintesimal derivative by a finite stencil. The pressure is fully conserved in the simulations neglecting charge-exchange and recombination. In the other cases, fig. 4.6(a-c), the temperature drops to lower values at the target. Especially in the low temperature cases, the neutral density is significantly increased, in order to provide ionisation of a similar

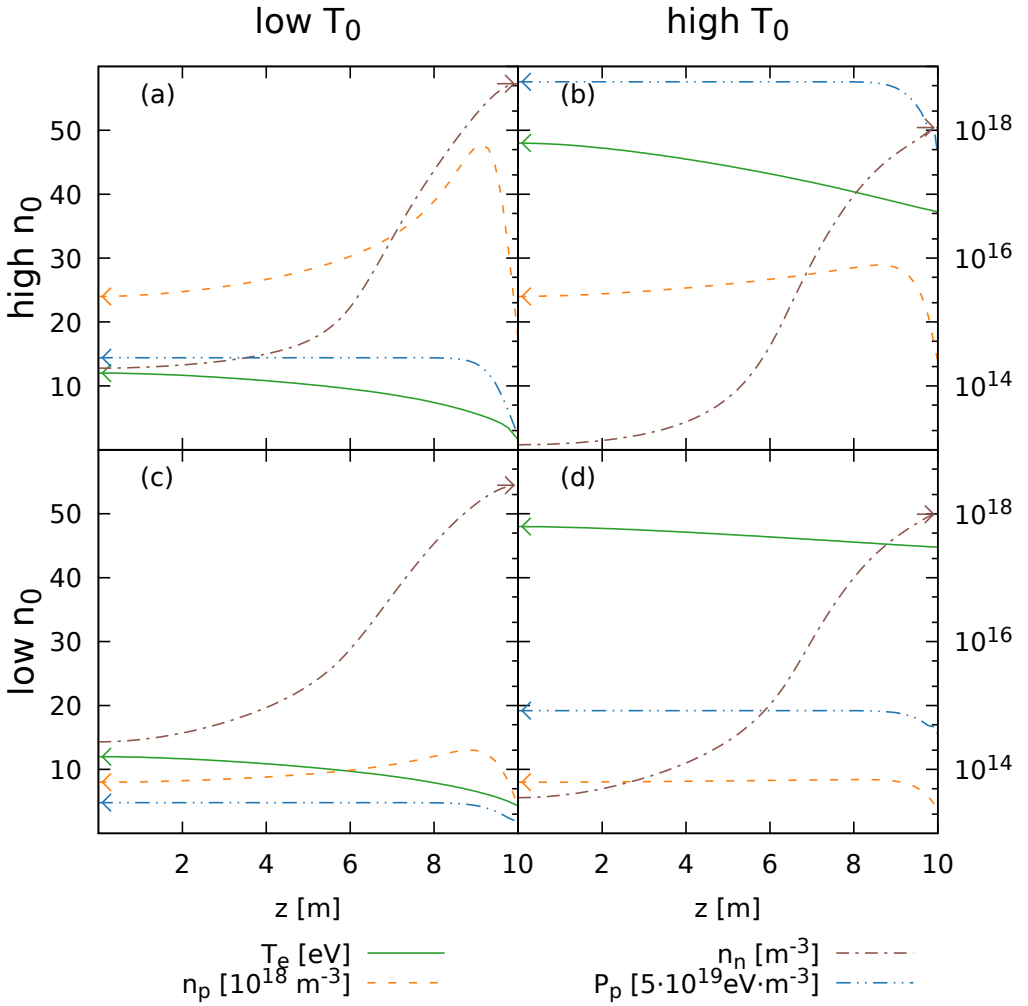

Figure 4.5: Background plasma profile, run to steady-state for a set upstream temperature (a,c) $T_0 = 12\,\mathrm{eV}$ and (b,d) $T_0 = 48\,\mathrm{eV}$ with (a,b) upstream density $n_0 = 32 \cdot 10^{18}\,\mathrm{m}^{-3}$ and (c-d) $n_0 = 8 \cdot 10^{18}\,\mathrm{m}^{-3}$. The quantities in each part are the same as in fig. 4.4.

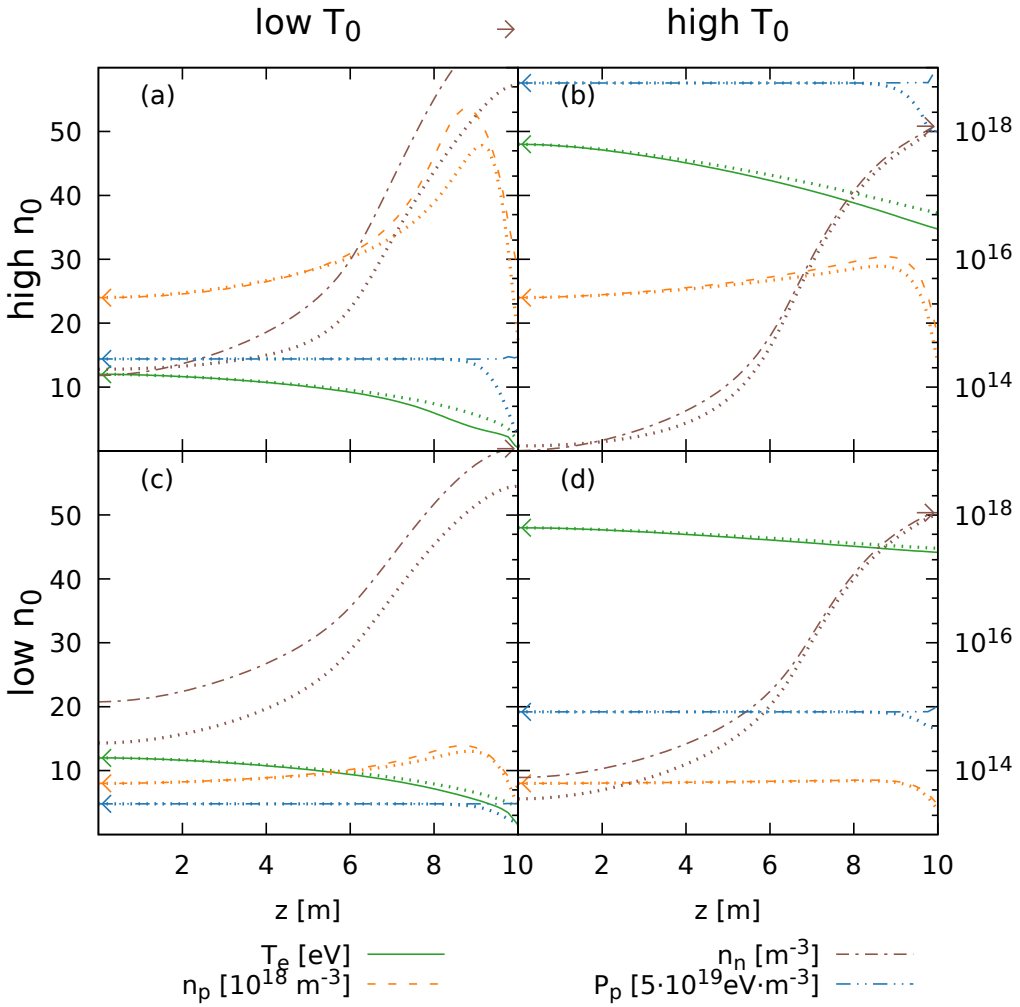

Figure 4.6: Background plasma profile, run to steady-state for a set upstream temperature (a,c) $T_0 = 12\,\mathrm{eV}$ and (b,d) $T_0 = 48\,\mathrm{eV}$ with (a,b) upstream density $n_0 = 32 \cdot 10^{18}\,\mathrm{m}^{-3}$ and (c-d) $n_0 = 8 \cdot 10^{18}\,\mathrm{m}^{-3}$. The quantities in each part are the same as in fig. 4.4. The simulations did only include ionisation, but no charge exchange or recombination to minimise the impact of neutrals. For comparison the quantities from fig. 4.5, i.e. for the case of full neutral interaction, are shown as dotted lines.

level to the full neutral model.

One should also note that the drop is plasma pressure is soley due to charge-exchange. This can be seen in fig. 4.6, as in the ionisation-only case the pressure is conserved. This has been verified by including ionisation as well as recombinisation, but no charge exchange, in which case the the pressure is conserved, as in the ionisation-only case.

Fig. 4.7 shows the neutral interaction rates for the backgrounds shown in fig. 4.5. The charge exchange rate is the largest rate, shown in green, followed by the ionisation rate, which is shown as orange dashed-line. The recombination rate is by far the smallest rate, and shown as a blue dash-dotted line. All quantities are shown on a log scale, as all, but the recombination rate, are strongly peaked at the target, due to the dependence on the neutral density. Also, the relative difference between the different rates are several orders of magnitude.

Shown in fig. 4.8 is the plasma potential for the four backgrounds shown in fig. 4.8. The potential is dropping off towards the sheath on the left hand side.

4.4 Detachment

As the density is further increased, the hot plasma is prevented from reaching the target. Instead cold plasma is close to the divertor, which is accompanied by a volume of high neutral density. Such a background is shown in fig. 4.9.

The temperature T_e is plotted in fig. 4.9(b). Starting from $T_e \approx 32\,\mathrm{eV}$ at the mid-plane, the temperature drops, until it reaches around $2\,\mathrm{eV}$ in the detached region. Within that region the temperature stays constant, as the

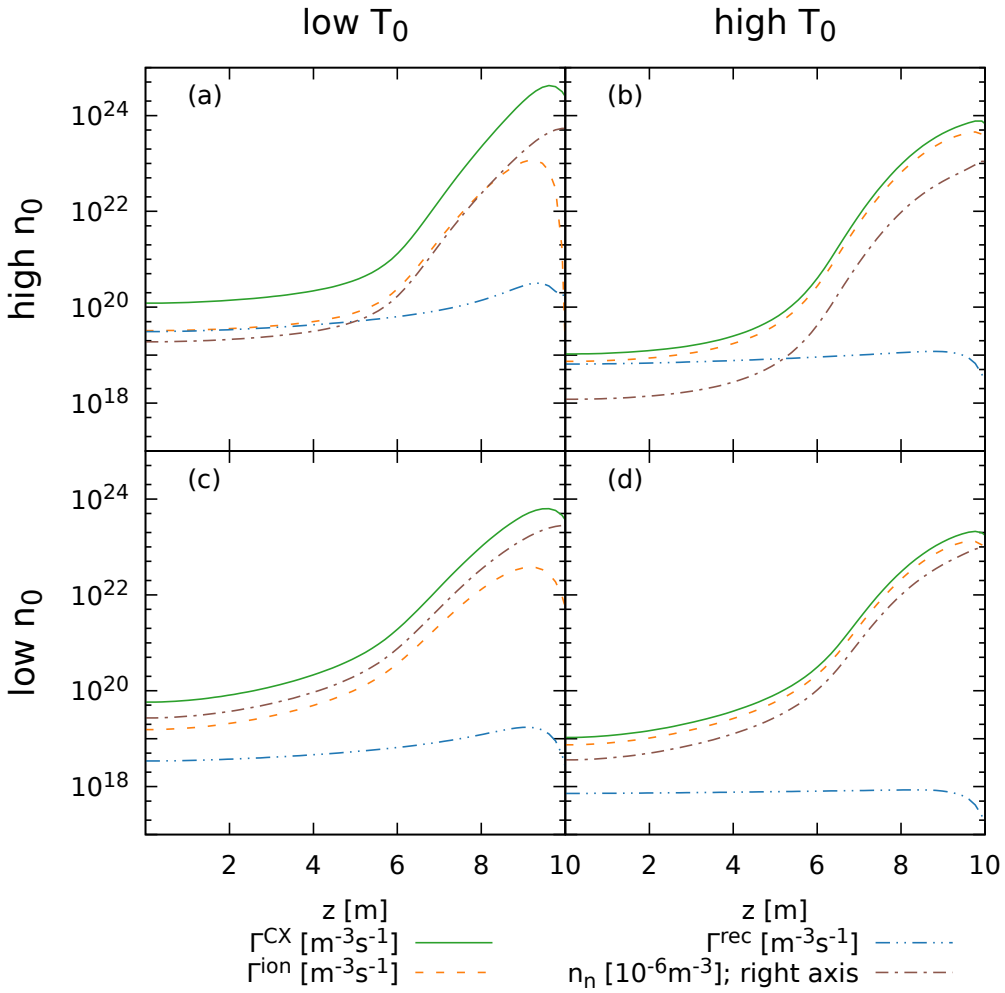

Figure 4.7: Neutrals interaction rates of the steady-state plasma backgrounds. Shown is the case of upstream temperature (a,c) $T_0 = 12\,\mathrm{eV}$ and (b,d) $T_0 = 48\,\mathrm{eV}$ with (a,b) upstream density $n_0 = 32 \cdot 10^{18}\,\mathrm{m}^{-3}$ and (c-d) $n_0 = 8 \cdot 10^{18}\,\mathrm{m}^{-3}$. The conditions in each part are the same as in fig. 4.5. Shown is the charge-exchange rate Γ^{CX}, ionisation rate Γ^{ion}, recombination rate Γ^{rec} as well as neutral density n_n for comparison. Note that the neutral density is scaled by 10^6 to match the rates' magnitude in the given units.

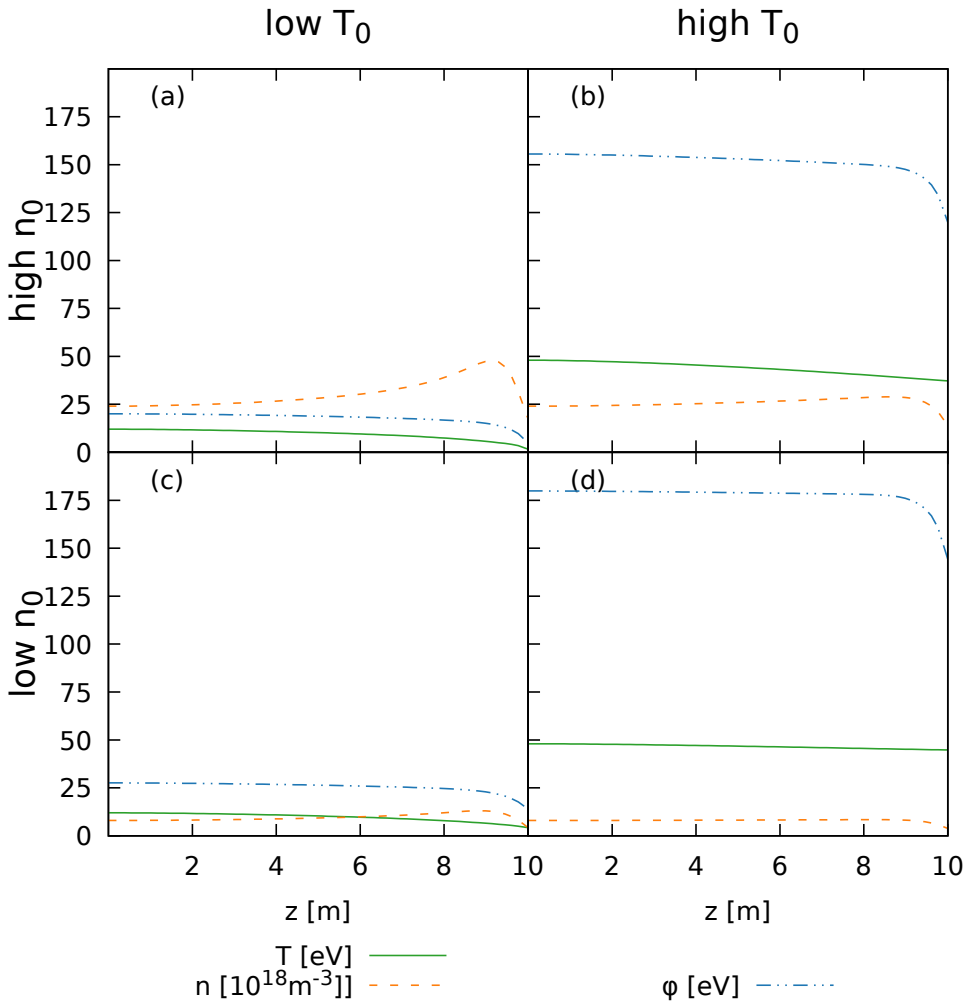

Figure 4.8: Plasma potential ϕ of the steady-state plasma backgrounds. Shown is the case of upstream temperature (a,c) $T_0 = 12\,\mathrm{eV}$ and (b,d) $T_0 = 48\,\mathrm{eV}$ with (a,b) upstream density $n_0 = 32 \cdot 10^{18}\,\mathrm{m}^{-3}$ and (c-d) $n_0 = 8 \cdot 10^{18}\,\mathrm{m}^{-3}$. The conditions in each part are the same as in fig. 4.5. Shown is the plasma potential ϕ as well as plasma density n and electron temperature T.

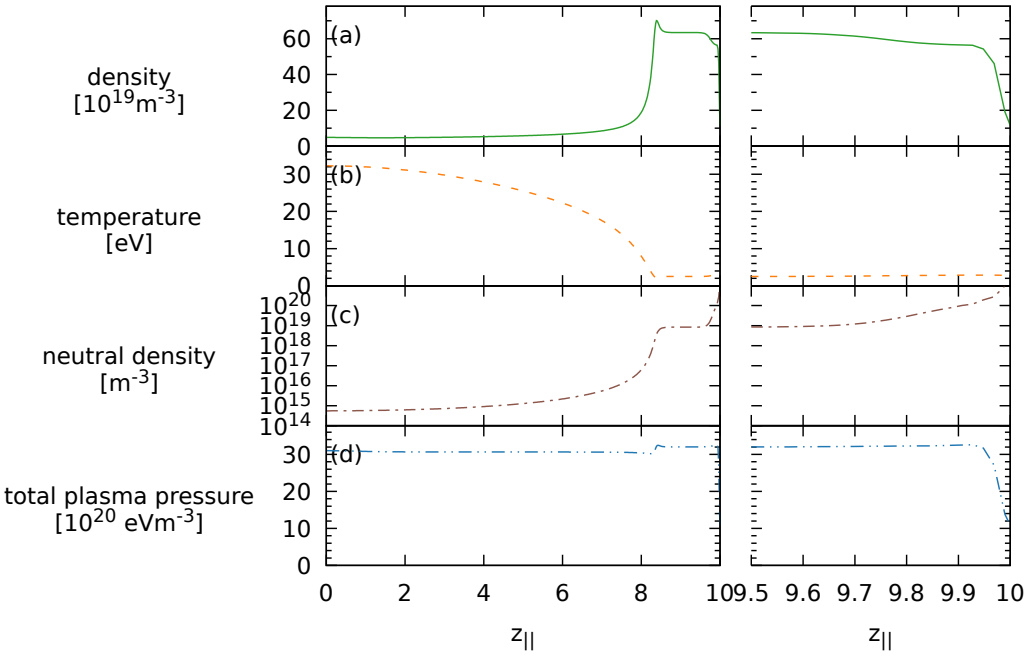

Figure 4.9: Background plasma profile, run to steady-state for an energy influx $10\,\mathrm{MW/m^2}$ and density $n_0 = 48 \cdot 10^{18}\,\mathrm{m^{-3}}$. On the right is a zoom in of the last meter in front of the target. The sheath is in both cases at the right hand side at $L = 10\,\mathrm{m}$. The mid-plane is at the left side, and is a symmetry plane. From top to bottom are plotted the plasma density n, electron temperature T_e, the neutral density n_n and the total plasma pressure P_p versus the parallel connection length. Note that the neutral density is plotted on a log scale, while the other quantities are plotted on a linear scale.

plasma is heated by the energy released from recombination [145, 151].

As the temperature drops, the pressure, shown in fig. 4.9(d) is conserved, and thus the density needs to increase. This can be seen in fig. 4.9(a). At the detachment front, the density peaks at $z = 8.4\,\mathrm{m}$, and then becomes flat within a detached region, where temperature T_e, plasma and neutral density are mostly constant. The neutral density, shown in fig. 4.9(c) increases from the mid-plane, where $n_n \approx 10^{15}\,\mathrm{m}{-}3$ to around $n_n \approx 10^{19}\,\mathrm{m}^{-3}$ in the detached region. Close to the target the plasma gets accelerated and the density is dropping. The neutral density is increasing further towards the target, and reaches densities around $n_n \approx 10^{21}\,\mathrm{m}^{-3}$ just in front of the target. The pressure drops just in front of the detachment front to around 30 % of the upstream value. The pressure shows also some deviation from conservation at $z = 8.4\,\mathrm{m}$, where due to the discretisation of the steep gradients a small increase is observed.

Similar to the attached conditions, where density and temperature scans of the background profiles where performed, also density and energy influx scans are shown in fig. 4.10. The above discussed features are generally present in the detached profiles, while the actual values, like the position of the detachment front, or the value of the pressure drop differ.

In the $5\,\mathrm{MW/m^2}$ case, detachment occurs below $n_0 = 32{\cdot}10^{18}\,\mathrm{m}^{-3}$. With increasing density the detachment front moves further towards upstream. The strongly detached cases, where the detachment front has moved quite far towards upstream would be experimentally not of interest, as the detachment front would reach the X-point, and the cold plasma and neutrals would lead to an increased radiation and thus decreased plasma performance [152]. This can lead to a a disruption caused by a radiative collapse of the plasma, e.g. a multifaceted asymmetric radiation from the edge

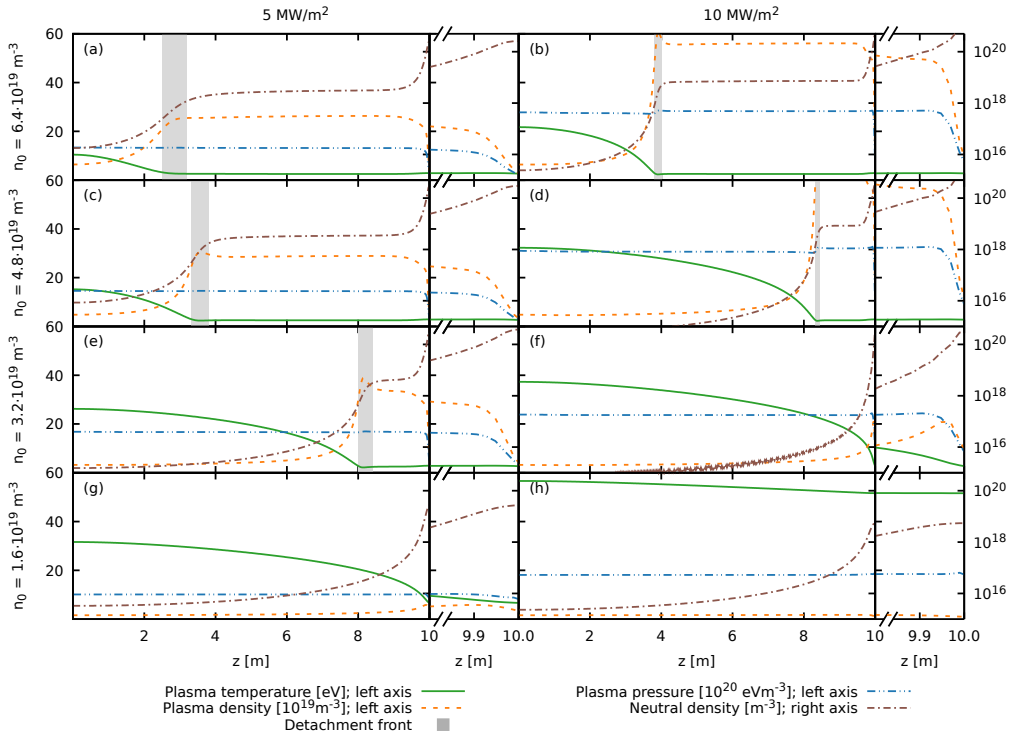

Figure 4.10: Background plasma profile, run to steady-state for set upstream energy influxes $5\,\mathrm{MW/m^2}$ (left) and $10\,\mathrm{MW/m^2}$ (right). The upstream density ranges from $n_0 = 64 \cdot 10^{18}\,\mathrm{m^{-3}}$ (a,b) to $n_0 = 16 \cdot 10^{18}\,\mathrm{m^{-3}}$ (g,h). The quantities in each part are the same as in fig. 4.9. Also a zoom-in on the last 20 cm in front of the target is included. As in the previous plots, the neutral density is on a log scale on the right, while the other quantities are on a linear scale on the left. The volume of the detachment front is shaded in grey.

(MARFE).

While in the attached case going to higher energy reduces the neutral density at the target, after detachment the opposite trend is observed, and the neutral density is increased. While in attached conditions a higher energy influx means a higher plasma temperature at the target, and thus more ionisation, in the detached cases more energy means more pressure that needs to be balanced by the neutrals, and thus an increased neutral density, as the temperature in the detached plasma is in all cases the same, around 2 eV.

An energy influx of $5\,\mathrm{MW/m^2}$ results for MAST parameters of $\lambda_q = 8.0\,\mathrm{mm}$ and a circumference of $2\cdot\pi\cdot R \approx 9.4\,\mathrm{m}$ for a major radius $R \approx 1.5\,\mathrm{m}$, yielding a total energy flux across the outer part of the SOL of 0.4 MW and 0.8 MW for the $10\,\mathrm{MW/m^2}$ case [67]. This is lower than the heating power of 5 MW that was available in MAST, thus these conditions are similar to MAST L-mode [67].

Often detachment is associated with plasma target flux roll-over. The plasma target flux as a function of upstream density is shown in fig. 4.11. After an initial increase of the plasma target flux, the flux decreases above $n_0 = 16 \cdot 10^{18}\,\mathrm{m^{-3}}$ for the $5\,\mathrm{MW/m^2}$ case, above $n_0 = 24 \cdot 10^{18}\,\mathrm{m^{-3}}$ for the $7\,\mathrm{MW/m^2}$ case. For the $10\,\mathrm{MW/m^2}$ case the picture is less clear, and the target flux shows a decreased increase above $n_0 = 30\cdot10^{18}\,\mathrm{m^{-3}}$, and decrease above $n_0 = 48 \cdot 10^{18}\,\mathrm{m^{-3}}$.

The neutral interaction rates for the backgrounds shown in fig. 4.10 are shown in fig. 4.12. Similar to the the rates shown in fig. 4.7, the charge exchange rate is by far the largest rate. In contrast to the attached conditions discussed in the previous section, in the detached volume recombination becomes important, and is of the same magnitued as ionisation. In

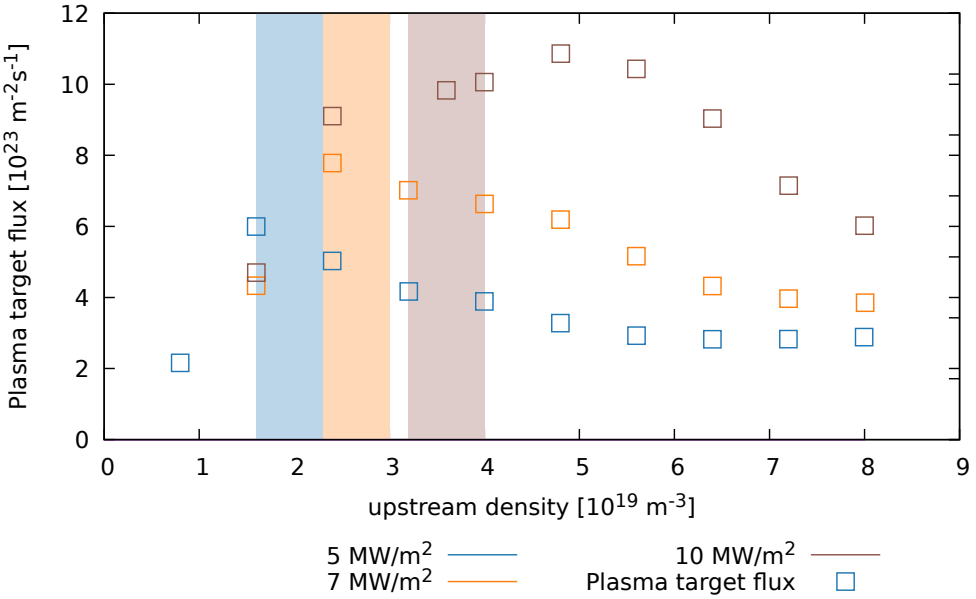

Figure 4.11: Plasma target flux as a function of upstream density for different values of the energy influx. The shaded region denotes the approximate region where the roll-over happens.

the shaded region showing the detachment onset, recombination is larger than ionisation, and density is transferred from the plasma to the neutrals.

Fig. 4.13 shows the plasma potential of the detached plasma backgrounds introduced in fig. 4.10. The plasma potential is mostly flat within the detached region, and only features gradients upstream of the detachment, as well as just in front of the target, where also density and temperature gradients are present. Thus, even though within the detached volume a high resistivity is present, no electric fields are observed.

One should note that the model is missing some physics, that may be important to accurately study detachment, e.g. molecules [57]. Also due to the 1D geometry used for the background, a full divertor geometry is not included. Related to this, the neutrals are only allowed to flow parallel to the magnetic field, rather than to at least include a 2D cross section as

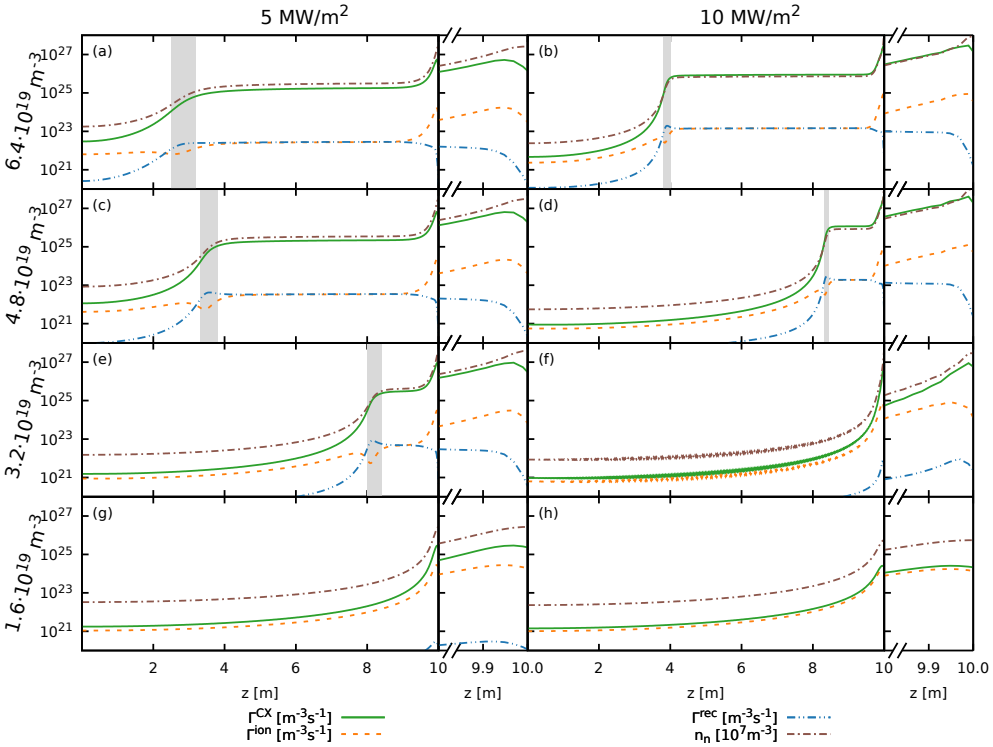

Figure 4.12: Neutrals interaction rates of the steady-state plasma backgrounds. Shown are the cases for an upstream energy influxes $5\,\mathrm{MW/m^2}$ (left) and $10\,\mathrm{MW/m^2}$ (right). The upstream density ranges from $n_0 = 64 \cdot 10^{18}\,\mathrm{m^{-3}}$ (a,b) to $n_0 = 16 \cdot 10^{18}\,\mathrm{m^{-3}}$ (g,h). Shown is the charge-exchange rate Γ^{CX}, ionisation rate Γ^{ion}, recombination rate Γ^{rec} as well as neutral density n_n for comparison. Note that the neutral density is scaled by 10^7 to match the rates' magnitude in the given units. The backgrounds are the same as in fig. 4.10, and similar to the previous figure, a zoom-in on the last 20 cm in front of the target is included. sdf The volume of the detachment front is shaded in grey.

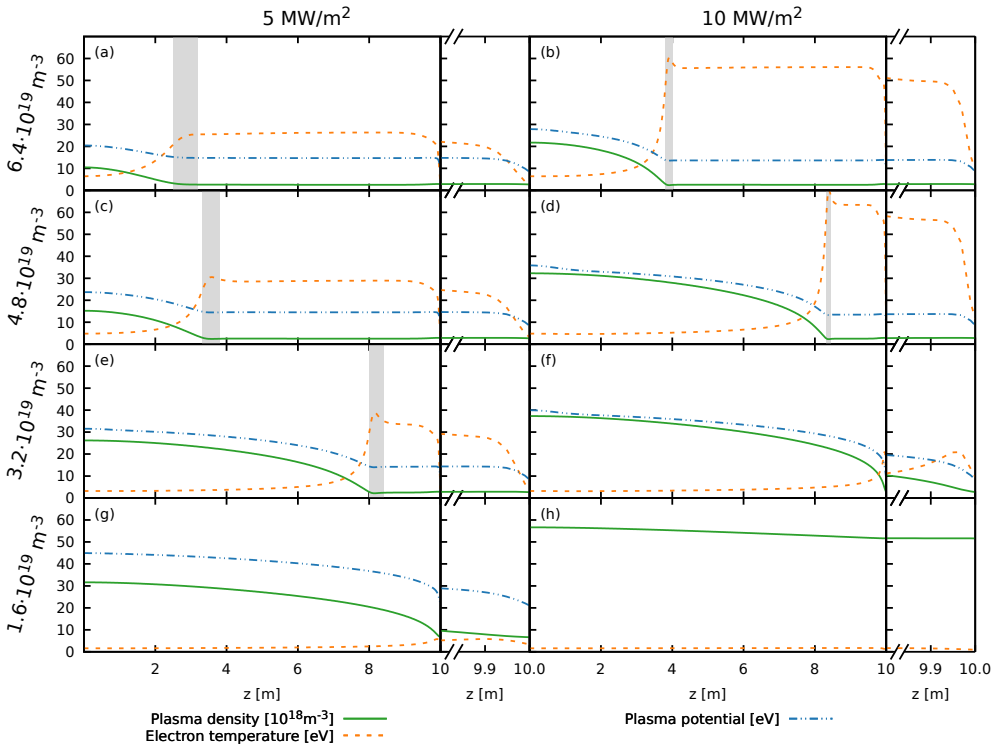

Figure 4.13: The Plasma potential of the steady-state plasma backgrounds shown in fig. 4.10. Shown are the cases for an upstream energy influxes $5\,\mathrm{MW/m^2}$ (left) and $10\,\mathrm{MW/m^2}$ (right). The upstream density ranges from $n_0 = 64 \cdot 10^{18}\,\mathrm{m^{-3}}$ (a,b) to $n_0 = 16 \cdot 10^{18}\,\mathrm{m^{-3}}$ (g,h). Shown is the plasma potential ϕ as well as plasma density and electron temperature. A zoom-in on the last 20 cm in front of the target is included. In the $n_0 = 16 \cdot 10^{18}\,\mathrm{m^{-3}}$ $10\,\mathrm{MW/m^2}$ case shown in (h) the potential reaches a midplane value just above 200 eV and is thus not shown. The volume of the detachment front is shaded in grey.

used in transport codes. As such, for example the plasma density where target flux rollover is observed is not expected to be accurate. Also the specific channels that are causing the density and mementum loss must not necessarily be accurate. As the primary focus of this thesis is on the filament dynamcics, it is expected that this does not significantly alter the dynamics of filaments, as the main features such as low plasma temperature, high plasma density as well as high neutral density, are reproduced.

4.5 Summary

The here presented 1D backgrounds, only retaining the parallel dimension, have been used to reproduce different plasma conditions, including low recycling, high recycling as well as detachment. In the high density cases, the total plasma pressure drops in front of the target, which is caused by charge exchange, as shown in sec. 4.3. As the density is further increased, detachment is reached. In this case the plasma flux decreased with increasing upstream density, in contrast to attached conditions, where an increase of flux with increasing density was observed.

CHAPTER 5

Filament dynamics in attached conditions

This chapter presents the effect of self-consistent plasma backgrounds including plasma-neutral interactions, on the dynamics of filament propagation in low to medium densities. The principle focus is on the influence of the neutrals on the filament through direct interactions as well as through their influence on the plasma background. As mentioned in the previous chapter, the neutrals interaction is for example responsible for the pressure drop in front of the target, and as such the neutrals influence the plasma background. Direct interactions are here defined as the interaction between the vorticity and the neutrals. The background profiles do have an impact on the filament dynamic, as the plasma parameter, such as viscosity, depend on density and temperature. The backgrounds have been introduced in sec. 4.2 and 4.3.

The results presented here have been run using the STORM model with

diffusive neutrals, as introduced in sec. 3.3 and 3.4.1.

The results have been published in two papers in Nuclear Materials and Energy [125] and Plasma Physics and Controlled Fusion [126].

5.1 Filament evolution

As discussed in the STORM section, the filament is seeded as a density and temperature perturbation on top of the background profiles. The initial shape in the perpendicular direction is Gaussian. The width used was $\delta_\perp = 20\,\mathrm{mm}$, and has later been extended by a scan in perpendicular filament size. The filament size of $\delta_\perp = 20\,\mathrm{mm}$ was chosen, as it is both close to the critical size δ^*, but also similar to the size experimentally observed in MAST [113, 125]. In the parallel direction a tanh shape is used with a typical parallel filament length of 5 m.

As discussed in sec. 2.2.4, the radial velocity from scaling laws is expected to scale with

$$v_r^s \propto \frac{\delta_p \sqrt{T_0 + \delta_T}}{(n_0 + \delta_n)\,\delta_\perp^2} \tag{5.1}$$

for the sheath limited regime and

$$v_r^i \propto \sqrt{\frac{\delta_p \delta_\perp}{n_0 + \delta_n}} \tag{5.2}$$

for the inertial limited regime [113]. δ_α is the perturbation above the background value α_0, for $\alpha \in n, T$. The pressure perturbation δ_p consists of density and temperature perturbation $\delta_p = \delta_n T_0 + \delta_T n_0 + \delta_T \delta_n$. To simplify the scalings we assume for now a constant filament size $\delta_\perp$, and set the density perturbation δ_n to the upstream density, n_0, such that $\frac{\delta_n}{n_0} = 1$. Doing

the same for the temperature perturbation, i.e. setting $\delta_T = T_0$, yields for the pressure perturbation $\delta_p = 3n_0T_0$. The scalings (5.1) and (5.2) reduce to:

$$v_r^s \overset{\delta_\alpha=\alpha_0}{\propto} \frac{n_0T_0\sqrt{T_0}}{n_0} \tag{5.3}$$

$$v_r^i \overset{\delta_\alpha=\alpha_0}{\propto} \sqrt{\frac{n_0T_0}{n_0}} \tag{5.4}$$

yielding a temperature dependence of $T_0^{\frac{1}{2}}$ for the inertial regime and $T_0^{\frac{3}{2}}$ for the sheath limited regime and no dependence on the density is predicted.

This convention for the filament perturbations will be adopted through out this chapter. Within the scaling T_0 describes a "background" temperature. As the background temperature in this study changes along the magnetic field lines, it is not obvious how this T_0 for the scaling should be calculated. The average temperature along the flux tube could be used, as well as the temperature at a certain point within the the flux tube, for example the upstream temperature or the electron temperature at the target.

For each filament simulation, the velocity of the the centre-of-mass was computed, using eq. (3.63) introduced in sec. 3.5.1. In order to compare the filaments of different backgrounds, the maximum of the radial filament velocity is computed and compared.

An example of a filament shape is shown in fig. 5.1. The mushrooming behaviour, typical for these filaments [22, 32, 113], can be seen. The mushrooming is caused by a non-uniform advection of the filament. The density perturbation causes a dipole in the vorticity, due to the curvature term C_ω in eq. (3.44). This dipole term in the vorticity causes an electric field, that is strongest in the centre of the filament. Due to $E \times B$ advection, the

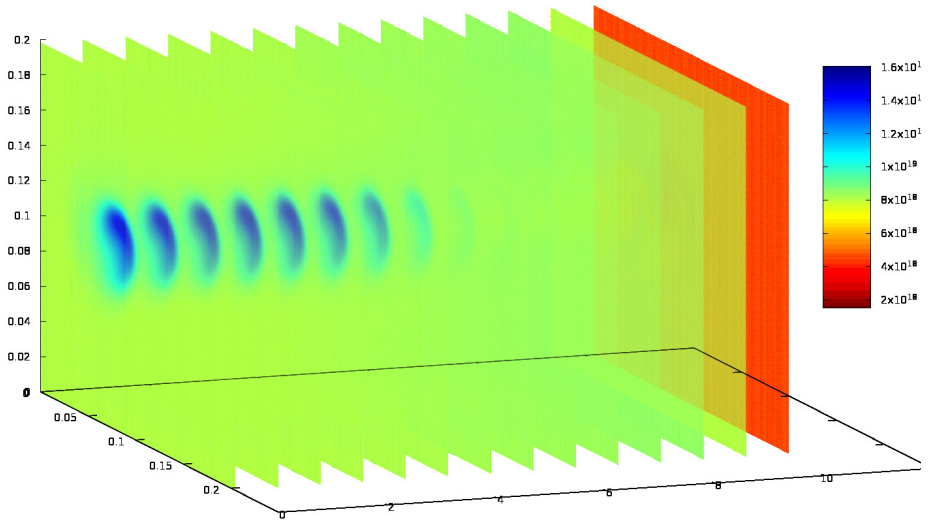

Figure 5.1: Snapshot of the density $\sim 7.5\,\mu s$ after the filament was seeded. The upstream background plasma density was $n_0 = 8 \cdot 10^{18}\,m^{-3}$ and the upstream electron temperature was $T_0 = 48\,eV$. The perpendicular size of the filament was $\delta_\perp = 20\,mm$.

centre of the filament moves fastest, and thus the typical mushroom shape can be observed. The filament is not symmetric in the y-direction. The motion in the y-direction, due to the temperature perturbation, has been observed and discussed [113, 153]. The temperature perturbation causes a monopole potential perturbation at the sheath. This in turn causes a monopole contribution in the currents, which causes a monopole contribution in the potential. This causes then a breaking of the up-down symmetry and causes the filament to spin. Note that also in iso-thermal systems spinning can be observed, for example the inclusion of a third dimension [22]. In other words, only in simple models preserve the up-down symmetry, and no spinning or bi-normal advection is observed. Fig. 5.2 shows the time trace of a filament. Initially the perturbation is Gaussian. After $\approx 8\,\mu s$ a deviation is visible as the filament started moving, and after $\approx 12\,\mu s$ a mushrooming form becomes apparent. The lack of up-down symmetry is

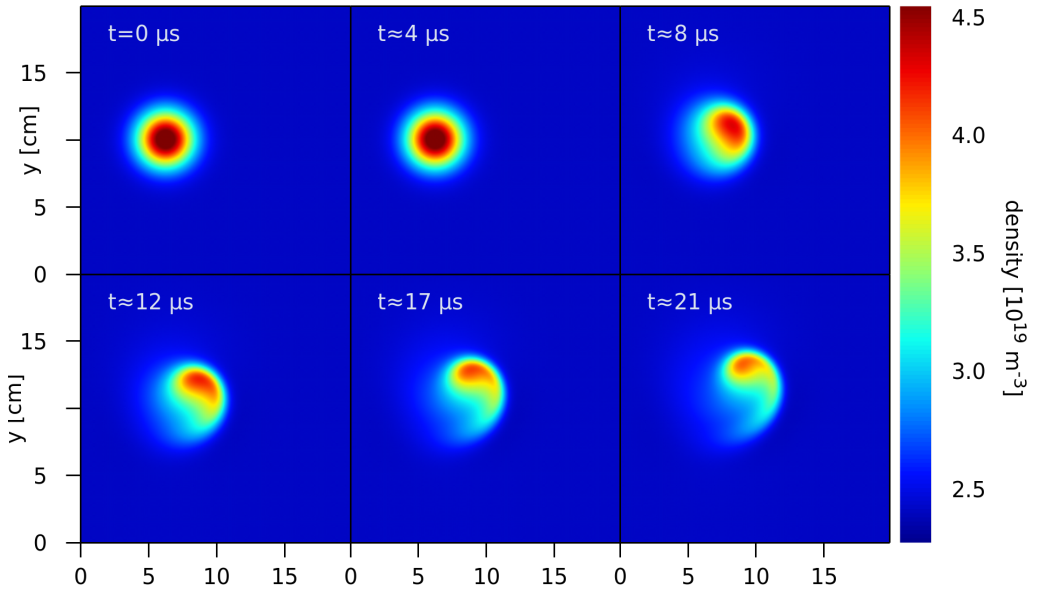

Figure 5.2: Snapshots of the evolution of the density of a seeded filament. The upstream background plasma density was $n_0 = 24 \cdot 10^{18}\,\mathrm{m}^{-3}$ and the upstream electron temperature was $T_0 = 48\,\mathrm{eV}$. The perpendicular size of the filament was $\delta_\perp = 20\,\mathrm{mm}$.

visibly broken as soon as the filament starts moving around $\approx 8\,\mu\mathrm{s}$.

5.2 Influence on filament velocity

In order to distinguish the direct and the indirect influence of neutrals on filaments, different neutral models are compared in sec. 5.2.1. This will be followed by a study of the dependence of filament dynamics on the backgrounds in sec. 5.2.2, before we conclude in sec. 5.2.3 with results of the filament size dependence.

5.2.1 Neutrals

As the neutral density in the divertor is rather high, it is important to understand the effect of neutrals on they dynamics of filaments. Especially

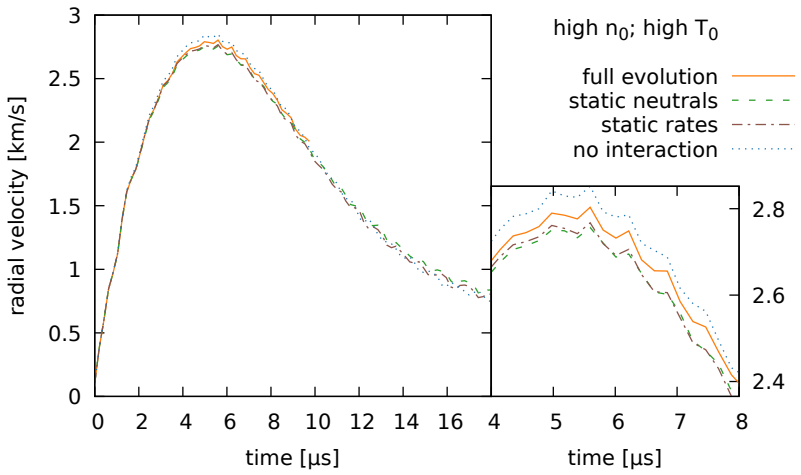

Figure 5.3: Comparison of different neutral filament interaction models. Left an the full time range, and on the right a zoom-in on the time around the peak. In the full evolution case (orange line), the neutral density is co-evolved with the filament, and the rates were calculated self consistently. In the no interaction case (blue dotted), the neutral term in the vorticity equation is switched off. In the static-rates case (green dashed) the neutral interaction rates Γ^{α} from the equilibrium profiles are used. In the static neutrals case (brown dash-dotted), the neutrals are not evolved, but the rates were calculated.

as future fusion devices are expected to operate at even higher densities, it is of importance to increase the understanding and ability to extrapolation to these regimes. In this section the direct influence of neutrals on the filament dynamics is studied. The direct influence is here understood as the influence of the neutrals via an interaction with the vorticity of the filament, while the indirect one is understood as the remaining interaction of the neutrals with the filament. This includes for example changes in the plasma background profiles due to neutrals, or fuelling of the filament density via increased ionisation of the hot filament. In order to study the direct interaction between the neutrals and the filaments, different neutral-filament interaction models are used.

The results are shown in fig. 5.3. The no interaction case is where the neutral term in the vorticity equation is set to zero, so that there is no direct interaction between the filament and the neutrals. In terms of the vorticity equation (3.44), N_ω is dropped. For the other terms the neutrals are kept static, i.e. the neutrals are not evolved in the filament simulation, but rather the neutral profiles, as determined by the background simulations are used. This is equivalent of setting $\mathrm{d}n_n/\,\mathrm{d}t = 0$. The neutral rates are nevertheless calculated self consistently. In the static rates case the neutral plasma interaction rates, namely charge exchange rate Γ^{CX}, ionisation rate Γ^{ion} and recombination rate Γ^{rec}, are kept at their steady state values. This ensures that areas not affected by the filament are kept at the steady state value. The static rates case represents a state where the neutrals are still interacting with the plasma, but the impact of neutrals on the filament is only possible via the background profiles. In another set of simulations, the "static neutrals" case, the interaction between filament and neutrals is increased. There the neutral profiles are not evolved, but the plasma is used to calculate the interactions rate. Thus the density perturbation, the temperature perturbation as well as parallel velocities are taken into account to calculate the rates. In the full evolution case the interaction is fully enabled. The neutrals are evolved self consistently, and the interaction rates are computed including both background and filament contributions to density and temperature.

These simulations were done for the different backgrounds shown in fig. 4.5. The result shown in fig. 5.3 is the one with the strongest difference between the velocities caused by the different neutral models, the background profile with high density n_0 and high temperature T_0. The relative reduction for the high density and low temperature case is about half of the

reduction of the velocities shown in fig. 5.3. As shown in fig. 4.7 the charge exchange rate of the backgrounds is in the low T_0 case ~ 5 times as high, as in the high temperature case, while the ionisation rate peaks at about $\frac{1}{4}$ of the high temperature case. Fig. 5.3 shows that there is only a small difference for the static neutrals and static rates cases. In the case where the neutrals are evolved, the filament moves slightly faster. The filament is fastest when the neutrals drag term in the vorticity equation is switched off, as shown in fig. 5.3, labelled as the no interaction case. This can be explained as the neutrals are causing a diffusion like term in the vorticity equation, thus reducing the vorticity and causing a reduced electric field. In the case where the neutrals are co-evolved with the filament, the filament ionises a part of the neutrals, reducing the neutral density, which explains why the velocity lies between the static case and the no interaction case, as here the drag term N_ω is included, but is reduced compared to the static cases, but still larger to the no interaction case, where N_ω is completely dropped from the vorticity equation (3.44).

While the direct impact of neutrals on the filament motion is very small, the impact increased for higher plasma density and plasma temperature. The impact observed here of neutrals is experimentally not measurable. Increased neutral interaction rates are probably needed for the effect to become measurable. The following results in this chapter are obtained using the static neutral approximation, as this significantly accelerates the computation, without strongly impacting the filament dynamics. With the full neutral model evolving the filament simulation for $1/\Omega_i$ took ~ 3 to 24 minutes, depending on the background conditions, while the static neutral model took between 0.3 and and 0.6 minutes per $1/\Omega_i$, resulting in a speed-up between 8 and 40. As with decreasing neutral density the diffusion rate

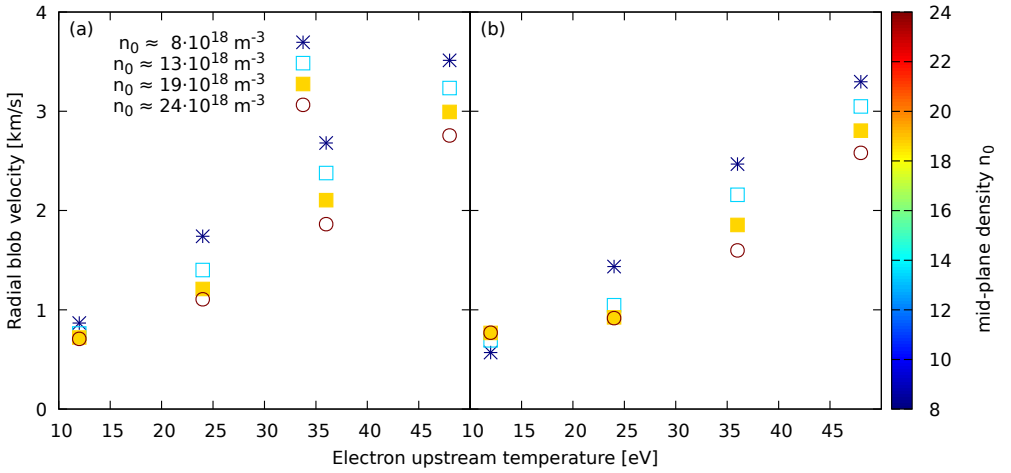

Figure 5.4: Comparison of the filament velocities for the different set of background profiles, (a) backgrounds with full neutral interaction and (b) without recombination and charge exchange. The upstream density is colour coded, see legend. The simulations in (a) are run on the backgrounds shown in fig. 4.5, while the simulations in (b) are run on the ones shown in fig. 4.6.

increases, the time step of the simulation is decreased for low densities, thus increasing the wall time significantly if the neutrals are evolved. The deviation from the full neutrals evolution is less than 2 % in the conditions featured here, which do not include detachment. As shown by Thrysøe et al., D_2 molecules can fuel the atomic neutral density in a filament, which makes the static neutrals approximation even more applicable [154]. In the here presented model only atomic neutrals are present, thus any source from D_2 molecules is missing. As some of the depleted neutrals, which are ionised by the filament, would be replaced by dissociated molecules, the expected neutral densities are somewhere between the static neutrals case, which neglects the filament, both for ionisation and dissociation, and the full evolution of the neutrals, which neglects dissociation.

In addition to the weak dependence on the direct interaction between

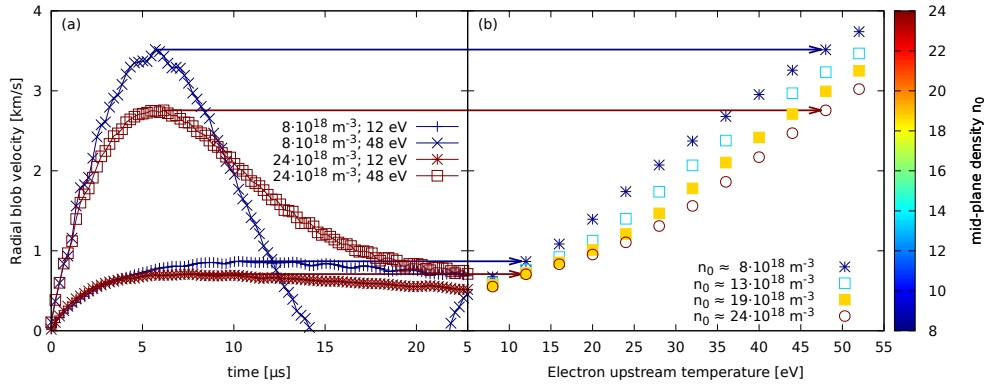

Figure 5.5: Radial velocity of filaments seeded on different backgrounds. Shown in (a) is the time evolution of the filaments, and (b) shows the peak radial velocities as a function of the upstream temperature. The upstream density is colour coded, see legend.

filament and neutrals, the filament velocity varies strongly with background conditions. This is shown in fig. 5.4, where on the left filaments were seeded on the backgrounds, that have been discussed in sec. 4.3 and shown in fig. 4.5. Also shown is the effect of removing charge exchange and recombination from the simulations. The backgrounds that have been used in this set of simulations, are shown in fig. 4.6. This impacts filament velocity through the change in the backgrounds, indicating that neutrals are important and interact with the filament indirectly via the plasma background. In the next section the filament velocity's dependence on the background conditions is studied in more detail.

5.2.2 Dependence on the plasma background

This section presents the dependence of the filament's radial velocity on the background conditions. Fig. 5.5(a) shows the time evolution of filaments seeded on the background profiles shown in fig. 4.5. On the right hand side of fig. 5.5 is a plot of the peak of the filament's radial velocity as

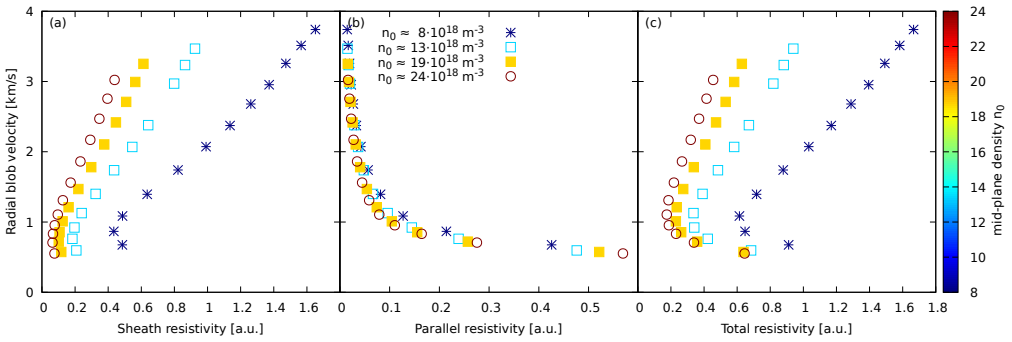

Figure 5.6: Radial velocity of filaments seeded on different backgrounds. Shown in (a) is the peak velocity as a function of sheath resistivity, (b) as a function of the parallel resistivity and (c) as a function of total resistivity. The upstream density is colour coded, see legend.

a function of the upstream temperature. The velocity increases with an increase of temperature. The velocity decreases with increasing density, with the exception of low temperatures, where this trend is inverted. As the filaments are seeded such that $\frac{\delta_n}{n}$ stays constant, the density dependence is not expected from the simple scaling analysis shown in section 2.2.4.

Earlier studies in STORM looked at the influence of the resistivity [121]. The resistivity was studied as with increased resistivity currents are suppressed, and especially larger filaments, where a significant part of the vorticity is closed via sheath currents, are expected to be accelerated. This was done by artificially changing the resistivity in an ad-hoc manner. In this study the resistivity scan is repeated in a self consistent way, by changing temperature and density, which then changes the resistivity, as the resistivity $\nu_\parallel$ is $\nu_\parallel = 0.51\nu^0_{e,i} n T^{-\frac{3}{2}}$ with $\nu^0_{e,i}$ the ion-electron collisionallity at the reference density and temperature.

Fig. 5.6 shows the peak velocity as a function of (a) the sheath resistivity, (b) the plasma resistivity integrated along the magnetic field lines and (c) the total resistivity, consisting of the sum of both. The sheath resistivity

is calculated as $\sqrt{T}/n$ following the derivation by Easy et al. [121]. Note that the non-monotonic behaviour below 1 km/s is because the density at the target reduces quite strongly with decreasing temperature. Therefore the sheath resistivity increases, and the colder temperatures have a higher target resistivity. As such the resistivity is not an ordering parameter, as for the same resistivity different filament velocities are measured, even if the data set is restricted to a single density. As the plasma resistivity is a function $\propto 1/T^{\frac{3}{2}}$ of the temperature, the scaling in (b) shows a monotonic decreasing behaviour. This is not an effect of the resistivity as with increasing resistivity the vorticity should increase, which Easy et al. observed to result in faster filaments [121]. This shows that in this self consistent study, the change in resistivity is less important than the associated change in temperature, for the conditions studied here.

The simple scaling analysis shown in section 2.2.4 requires a single background temperature, however the temperature is not constant along the magnetic field lines. Fig. 5.7 shows the filament peak velocities for the different profiles as a function of the upstream temperature, the average temperature along the magnetic field lines and the target temperature, in each case of the background profiles. In all cases a monotonic increase with temperature is observed. In the "no neutrals" case, the density source has been replaced by an exponentially decaying density source at the target to emulate the ionisation from the neutrals. The systematic, small reduction in filament velocity for the "no neutrals" case is most likely due the mismatch in plasma source compared to the full neutral backgrounds. This is most evident when plotted against the target temperature. When plotted against the target temperature, the data approximately collapses onto a single curve regardless of upstream density This suggests that the tar-

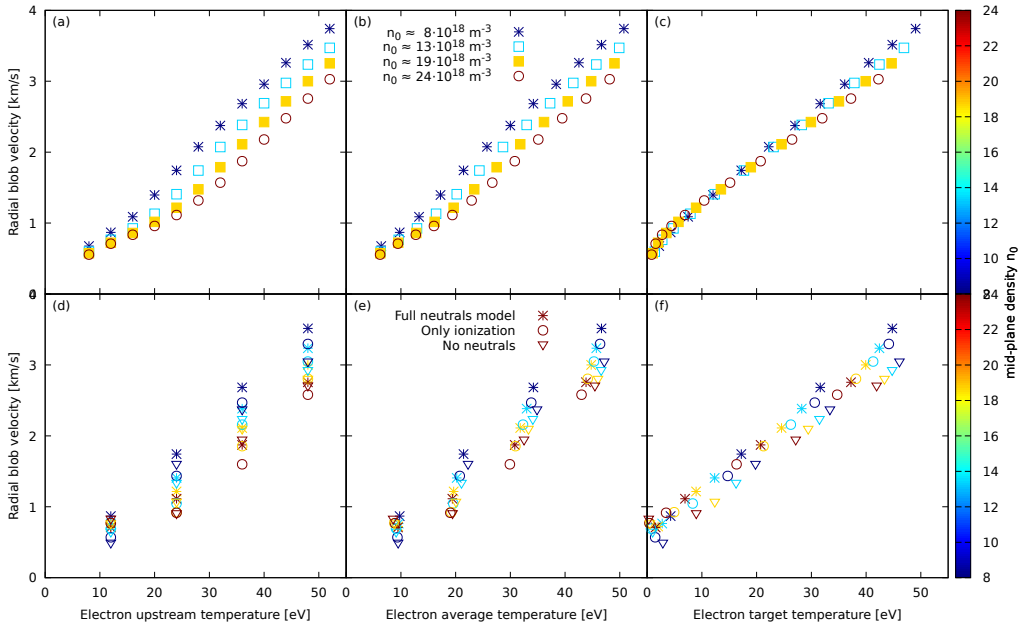

Figure 5.7: Radial velocity of filaments seeded on different backgrounds. Shown is the peak velocity as a function of the temperature. On the top (a-c) are the results with static neutrals, while on the bottom (d-f) are the results for both the full neutral model (stars), the ionisation only model (open circle) and no neutrals model(open triangle). On the left (a,d) the velocity is plotted against the upstream temperature, in the middle (b,e) the velocity is plotted against the average temperature and on the right (c,f) the data is plotted against the target temperature. The upstream density is colour coded, and in (a-c) also shown with different symbols, see legend in (b) or colour-bar.

get temperature is a good scaling quantity for the radial velocity of the filaments studied here. In fig. 5.7 (f) the results from the different neutral models are much closer to each other than in fig 5.7 (d-e) where they are plotted as a function of the upstream temperature T_0 and the average temperature.

In the vorticity equation, which determines the filament radial velocity, the drive term C_ω is balanced by an interplay between advection terms A_ω, parallel currents J_ω, viscous currents B_ω and neutral friction currents N_ω. As part of the filament's vorticity is closed via viscous currents B_ω, we do not expect such a strong dependence on the target temperature. To study the impact of the viscosity further, a set of simulations was run, removing the density dependence of the plasma viscosity μ_ω in eq. (3.48). μ_ω has otherwise a linear density dependence, so an increased density leads to an increased diffusion of the vorticity, thereby reducing the drive. Fig. 5.8 compares the simulations with self consistent viscosity (a-c) with the ones where the plasma viscosity has no density dependence (d-f). The density dependence of the radial velocity, when plotted against the upstream temperature, is significantly reduced in fig. 5.8(a,d). In fig. 5.8 (f) the radial velocity is plotted against the target temperature. Although the points do not collapse onto a single line, they are still reasonably close to a single line. This supports the argument that the filaments are not only influenced by the target temperature, but also by the plasma viscosity μ_ω. It is worth noting that a similar collapse onto one line is apparent in fig. 5.8(d). It seems like the average temperature strongly influences the filament velocity when the density dependence of the plasma viscosity is removed. In the case of the self consistent viscosity, the target temperature appears to be the dominant influence on the filament velocity. Since the viscosity is acting

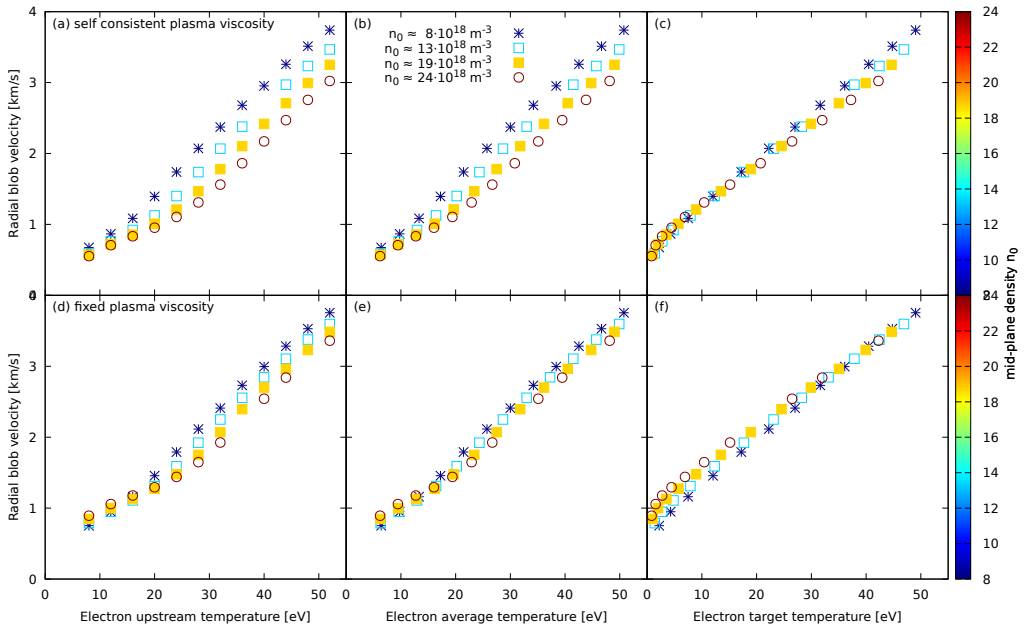

Figure 5.8: Peak radial velocity of filaments as a function of upstream, average and target temperature. The filaments in (a-c) are evolved with self consistent plasma viscosity and in (d-f) with the density dependence of the plasma viscosity removed. The upstream density is colour coded, see legend in (b) or colour-bar.

in the drift plane, it seems unlikely that in one case the target temperature is controlling the filament's dynamics, and in the other the average temperature is dominant. This supports the argument that the collapse onto a single line is a coincidence, and most likely will not hold true for other conditions. In the simulations presented here sheath currents play a significant role, therefore the results are not directly applicable to situations where they are suppressed, for example in detached regimes. However the target temperature is experimentally easier to measure than the upstream temperature or the average temperature, thus this may still be useful to infer filament velocities.

Looking at fig. 5.8 (a) and (d), removing the density dependence of the plasma viscosity reduces the dependence of the filament velocity on the density. For the remaining density dependence, different reasons come into play. The plasma viscosity still has a temperature dependence and for higher densities the target temperature drops to lower values than for lower densities, causing a higher viscosity near the target. This shows that the filaments are indeed influenced by the conditions at the target. Note that the filaments have been seeded in a manner such that they are initially unconnected from the sheath. The filament also stays physically unconnected from the target, as the density perturbation does not reach the target during the filament simulation. The temperature perturbation can reach the target, depending on the background conditions. And in all here presented cases the electric perturbation can reach the target, as was already previously discussed by Easy et al. [121]. As such the filament can be influenced by the target, even if the density perturbation does not reach the target.

Another reason for the density dependence is via the neutrals. The

study of the direct influence of neutrals suggests that the neutrals have less of an impact for lower densities, compared to the dependence observed in fig. 5.3. The neutrals can only explain a part of the reduction for the filament's velocity, even for the higher density cases. Further, the background parallel velocity decreases with increasing density. The change in the parallel velocity is stronger for lower temperatures. This can be explained by an increasing importance of recycling compared to upstream density fuelling. Although this contribution is only small, it might explain in part the filament velocity crossover at low temperatures, where low densities are slower than high densities. This crossover is observed in the case where the density dependence of the viscosity is removed (fig. 5.8 (d)) as well as in the ionisation only case (fig. 5.4 (b)), while in the full case the density dependence is reduced (fig. 5.8 (a)).

Finally parallel currents play a significant role in the generation of vorticity. The parallel currents are affected by the sheath conditions, as they are flowing through the sheath. Therefore currents further upstream are also influenced by the sheath temperature.

Figure 5.9 shows different contributions to the time derivative of the vorticity equation (3.44). The different terms where introduced in sec. 3.3.2. The first row in fig. 5.9 shows the contribution from the C_ω term, being the curvature drive. The green line is the bi-normal dipole contribution, which results in a radial drive. See sec. 3.5.2 for a more detailed description of the decomposition used. The negative sign of the contribution results in a positive radial drive. The C_ω is mostly causing a bi-normal dipole vorticity contribution, as the pressure perturbation has only changed mildly from the initial Gaussian perturbation. The C_ω is mostly localised in the upper half of the domain, which represents the upstream half of the domain, where

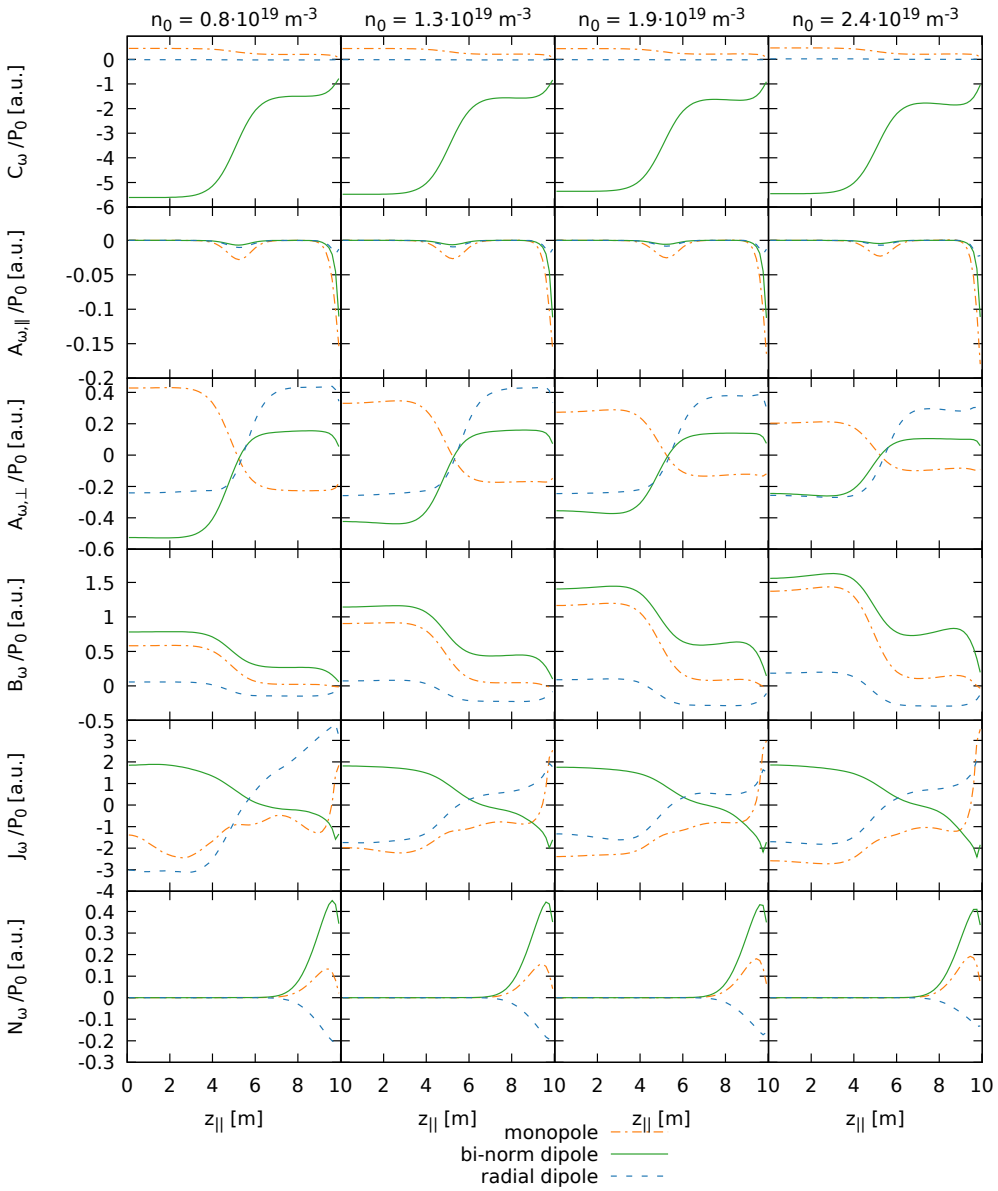

Figure 5.9: Contribution of the different terms in the vorticity equation (3.44). The different parts are decomposed as described in sec. 3.5.2. The contributions are analysed as the filament reaches peak velocity. Different density cases are analysed, all having an upstream temperature $T_0 = 48\,\mathrm{eV}$. All quantities are plotted on the same scale.

the perturbation is seeded. The different plots in the first row are taken from different density cases, all at $T_0 = 48\,\mathrm{eV}$. C_ω increases with increasing density, as the pressure in the flux tube, and thus the absolute perturbation is increased. The increase is however slightly less than linear, as the density increases 3-fold between the $n_0 = 8 \cdot 10^{18}\,\mathrm{m}^{-3}$ case on the left hand side, and the $n_0 = 24 \cdot 10^{18}\,\mathrm{m}^{-3}$ on the right hand side. Fig. 5.10 shows the same analysis as shown in fig. 5.9, but for an upstream temperature $T_0 = 12\,\mathrm{eV}$. In the low density case, the normalised drive, C_ω/P_0 does increase with density.

As the radial velocity is of prime interest in this study, mostly the binormal dipole vorticity contribution is discussed here, as it causes the binormal electric field that causes the radial $E \times B$ advection. The advection contribution A_ω has been split in a parallel and a perpendicular contribution. The perpendicular contribution is the $\vec{E} \times \vec{B}$ advection. The parallel contribution peaks at the target, where the parallel velocity is highest. A smaller peak is in the middle of the domain, where the filament ends, and the parallel movement is reducing the pressure difference. The perpendicular contribution has no significant density dependence. Thus the relative importance decreases with increasing density. This is in contrast to the viscous contribution B_ω, which increases even stronger than the driving term C_ω with increasing density. The current contribution J_ω is the largest contribution, besides the drive C_ω and is also increasing with increasing density. In the last row of fig. 5.9 is the impact of the neutrals on the vorticity equation. The impact of the neutrals is localised to the target, as the neutral density peaks at the target. While the impact of the neutrals increases with increasing density, the increases is less pronounced as the one for C_ω.

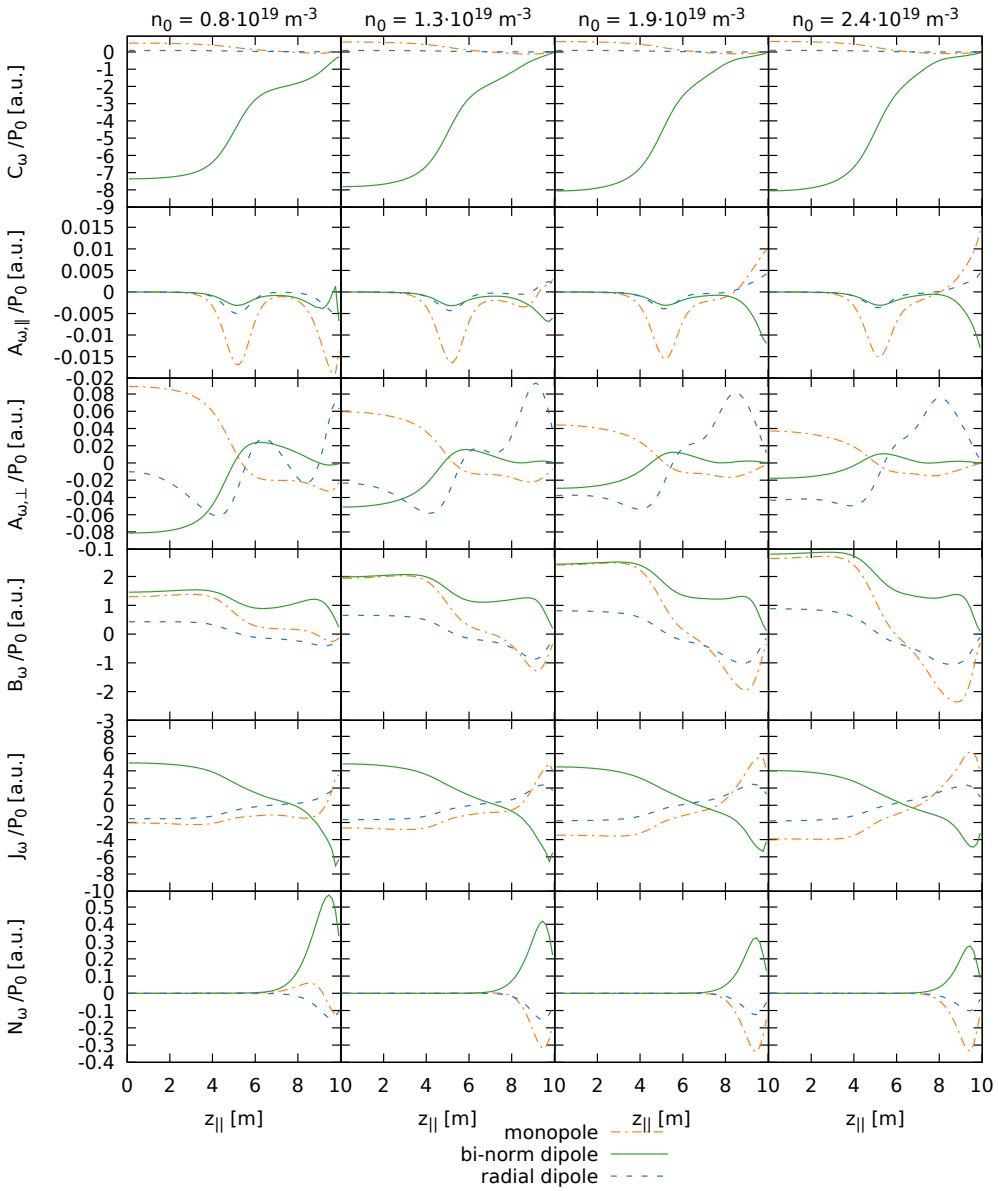

Figure 5.10: Contribution of the different terms in the vorticity equation (3.44). The different parts are decomposed as described in sec. 3.5.2. The contributions are analysed as the filament reaches peak velocity. Different density cases are analysed, all having an upstream temperature $T_0 = 12\,\mathrm{eV}$. All quantities are plotted on the same scale.

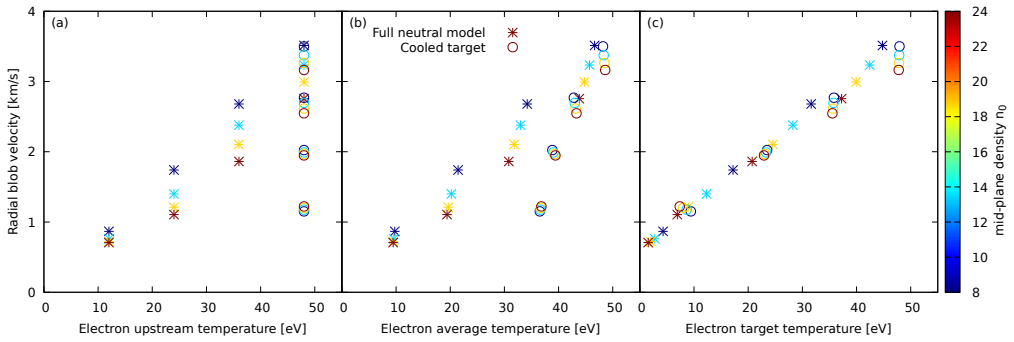

Figure 5.11: Peak radial velocity of filaments as a function of upstream and target temperature. In the simulations plotted with the open circle symbol, the plasma was cooled with an additional heat sink near the target. The upstream density is colour coded, see colour-bar.

To further test the dependence of the filament velocity on the various temperatures within the system, the upstream and target temperatures have been partially decoupled from one another. This has been achieved by inserting an artificial heat sink localised near the target to control the target electron temperature independent of the upstream temperature. This was done for the simulations with an upstream temperature of $T_0 = 48\,\mathrm{eV}$. For the plasma background profiles the temperature close the target was set to values between 12 eV and 48 eV. The resulting radial filament velocities are shown in fig. 5.11. Although the filaments were all seeded with the same perturbation of $\delta_T = 48\,\mathrm{eV}$, the filament velocity agrees with the scaling of the target temperature, rather than the upstream temperature.

Fig. 5.12 shows the contributions for the vorticity equation, as the target temperature is increased, for the $n_0 = 8 \cdot 10^{18}\,\mathrm{m}^{-3}$ cases. Fig. 5.13 shows a similar scan, but in contrast to fig. 5.12, no target heat sink was included, and the target temperature is changed self consistently by changing the upstream temperature. Fig. 5.13 shows, like fig. 5.12 the vorticity contribution for the $n_0 = 8 \cdot 10^{18}\,\mathrm{m}^{-3}$ case. If the target is significantly cooled,

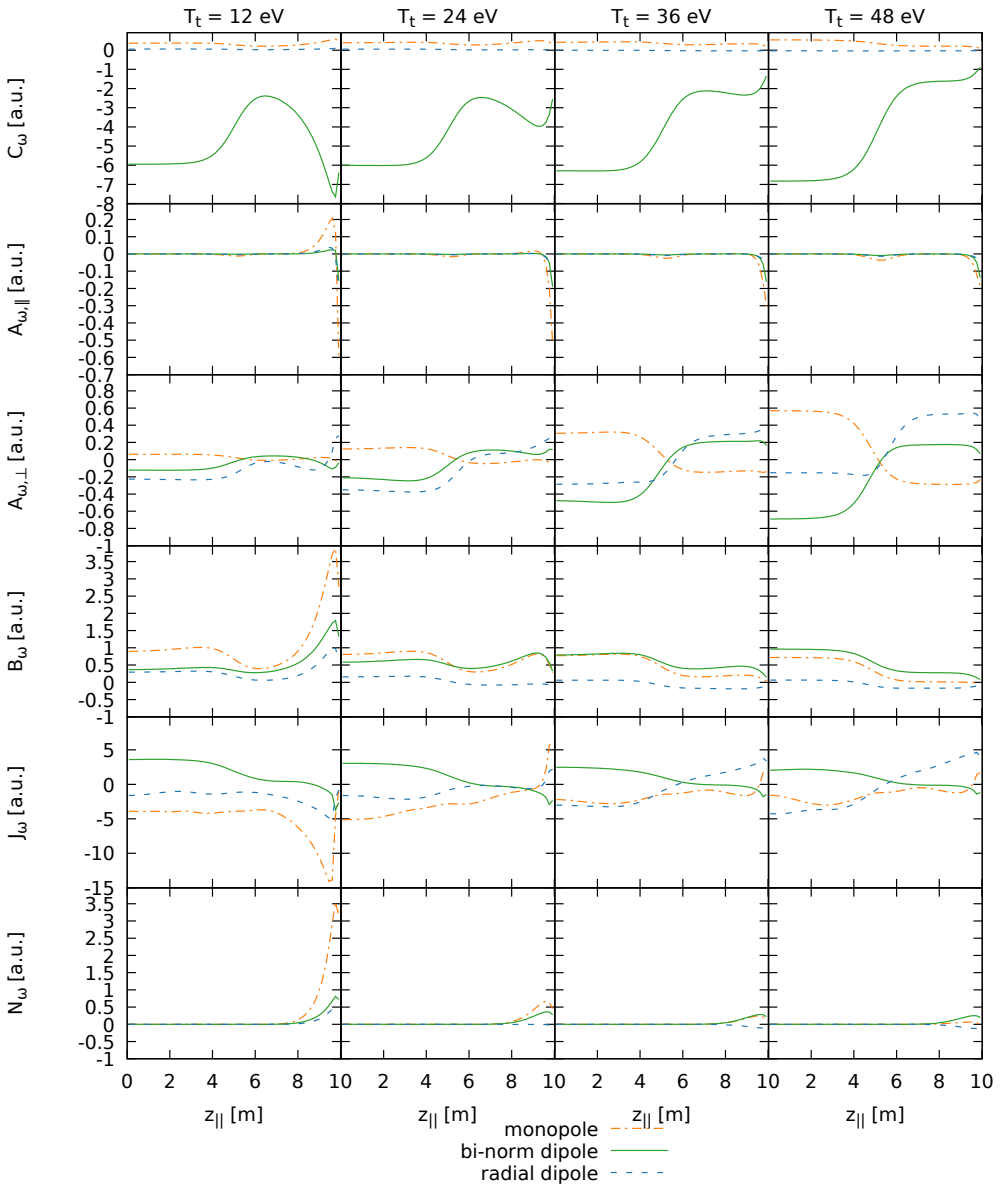

Figure 5.12: Contribution of the different terms in the vorticity equation (3.44). The different parts are decomposed as described in sec. 3.5.2. The contributions are analysed as the filament reaches peak velocity. Different target temperature cases are analysed, all having an upstream temperature $T_0 = 48\,\mathrm{eV}$ and an upstream density $n_0 = 8 \cdot 10^{18}\,\mathrm{m}^{-3}$. All quantities are plotted on the same scale. Fig. 5.13 shows a scan in temperature without additional cooling.

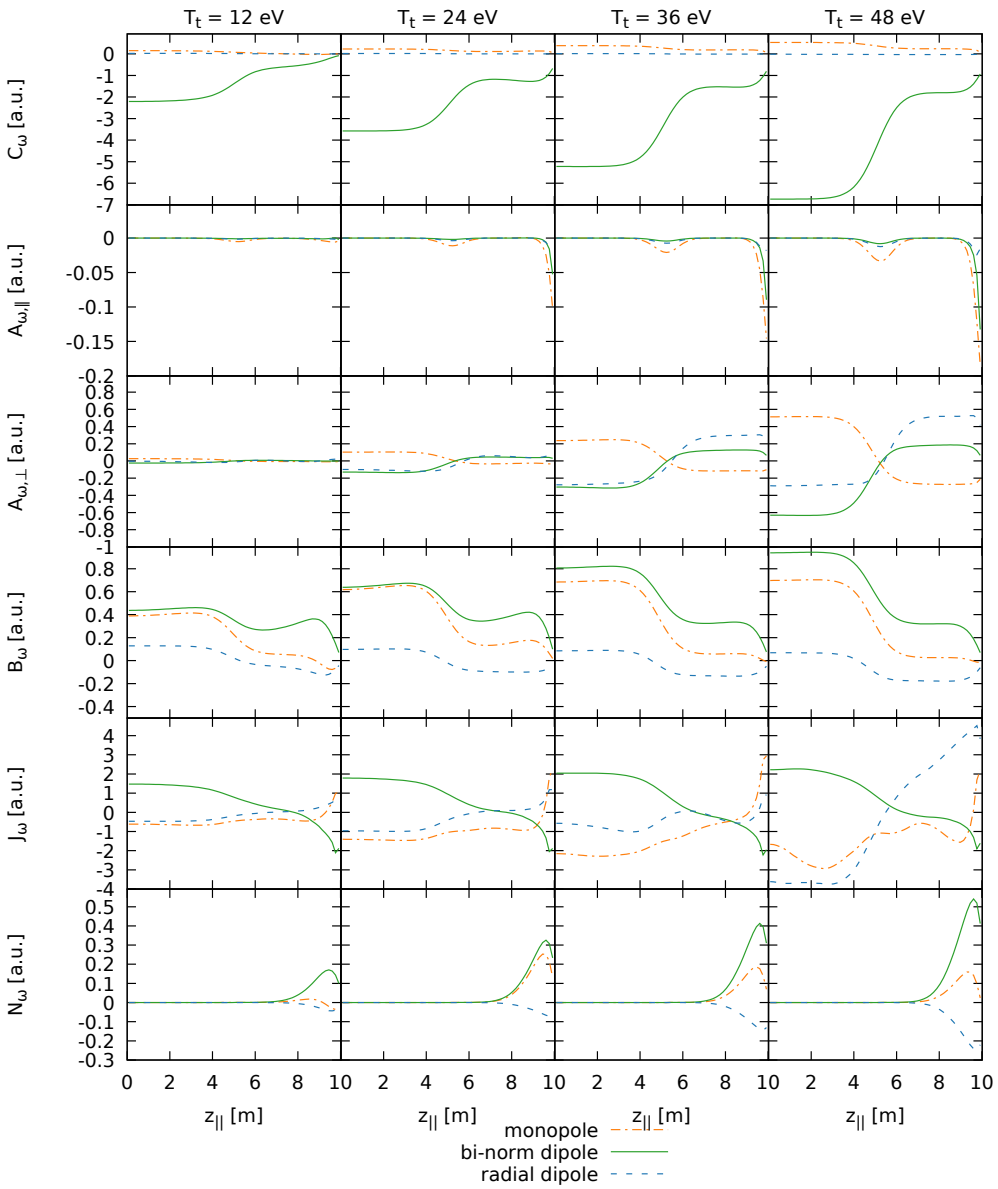

Figure 5.13: Contribution of the different terms in the vorticity equation (3.44). The different parts are decomposed as described in sec. 3.5.2. The contributions are analysed as the filament reaches peak velocity. Unlike fig. 5.12, the profiles are evolved self-consistently without cooling the target. The upstream density is $n_0 = 8 \cdot 10^{18}\,\mathrm{m}^{-3}$ and all quantities are plotted on the same scale.

the drive term is no longer only strong upstream, but also in front of the target, as the thermal perturbation quickly relaxes along the filament, and thus there is a significant pressure perturbation in front of the target. This is in agreement with fig. 5.14, where it can be seen that the temperature quickly relaxes to mostly flat profiles. As already established, the viscosity is responsible for a part of the T_t dependence. However, within the filament the viscosity is mostly independent of the T_t of the background, as the filament heats the plasma in front of the target. In the $T_t = 12\,\mathrm{eV}$ case, the plasma is heated to above 40 eV, thus significantly reducing the viscosity to around $\frac{1}{8}$ of the background profile value. In the strongly cooled $T_t = 12\,\mathrm{eV}$ case, the drive is similar to the non-cooled $T_t = 48\,\mathrm{eV}$ case, however the velocity of the $T_t = 12\,\mathrm{eV}$ case is well below that of the $T_t = 48\,\mathrm{eV}$ case. The J_ω term, caused by currents, is significantly increased in the cooled target cases. Especially in the area in front of the target, this causes a large monopole contribution. The significant viscous contribution B_ω near the target, which might suggest a T_t dependence, does on the one hand have mostly a monopole contribution, and the dipolar sink is well below the additional C_ω source near the target. As such it is not obvious why the target temperature scaling is reproduced. It seems however not be directly linked to the target temperature, as otherwise the $T_t = 48\,\mathrm{eV}$ cases should all drop on a single point in fig. 5.11, without a density dependence. Instead it is likely that the strong parallel temperature gradients significantly change the system, and the newly studied system, especially the $T_t = 12\,\mathrm{eV}$ has only limited applicable to the system of interest.

An exception is probably the $T_t = 48\,\mathrm{eV}$ case, as here the parallel dynamics is only slightly modified. And in this case, the target temperature dependence is not reproduced, but the density dependence compared to the

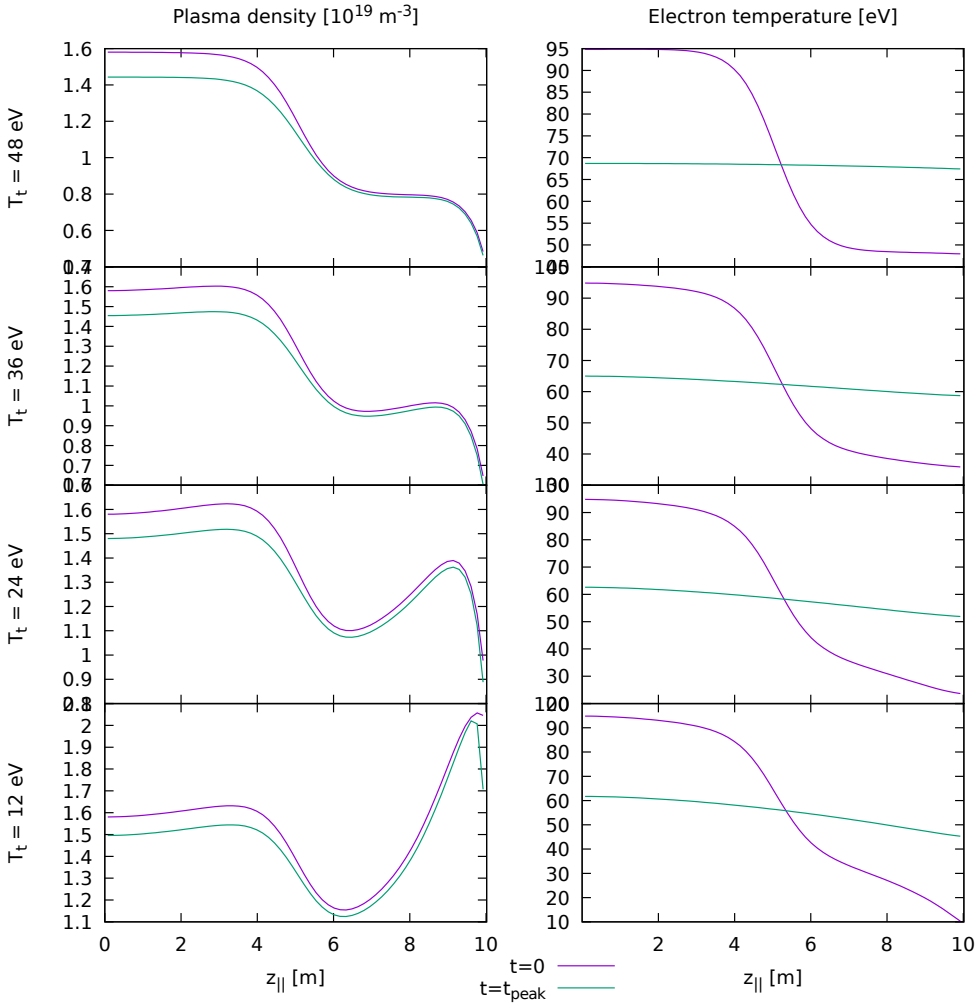

Figure 5.14: Density and temperature profile within the filament for the cooled target case for an upstream density $n_0 = 8 \cdot 10^{18}\,\mathrm{m}^{-3}$. n and T is plotted for $t = 0$ as well once it reaches peak velocity t_{peak}.

unaltered $T_0 = 48\,\mathrm{eV}$ case is reduced, as can be seen in fig. 5.11(c) on the right. This supports the point that a part of the deviation from an upstream temperature dependence is via sheath conditions, and another part is due to viscosity,

Based on the strong target temperature dependence, it seems tempting to derive a scaling law based on the floating potential, which is dependent on the target temperature. Walkden et al. shows that the thermal contribution to the filament motion causes filament spinning, rather than advection [113]. The floating potential might be involved in the acceleration of the filament, and might even be partially responsible for the linear target temperature dependence. But rather than advecting the whole filament, the detailed motion of the filament needs to be considered, thus making this process hard to capture in a scaling law.

5.2.3 Filament size

To study the influence of the size of the filament on its dynamics, different sized filaments have been seeded, and their motion analysed. Fig. 5.15 (a) presents the scan in filament size. It can be seen that the filament size δ^*, where the filaments are fastest for $n_0 = 8 \times 10^{18}\,\mathrm{m}^{-3}$ is between 15 and 20 mm, and for $n_0 = 24 \times 10^{18}\,\mathrm{m}^{-3}$ is between 19 and 22 mm. The critical size is determined by fitting a quadratic function in log space using gnuplot [155]. The critical size increases with increasing density, as well as with increasing temperature. The dependence of the temperature is decreased with increasing density. As in the high density case, the relative difference between the critical size for the two temperature cases is decreased, which is shown in the inset in fig. 5.15.

As already done in the study of the dependence of the background con-

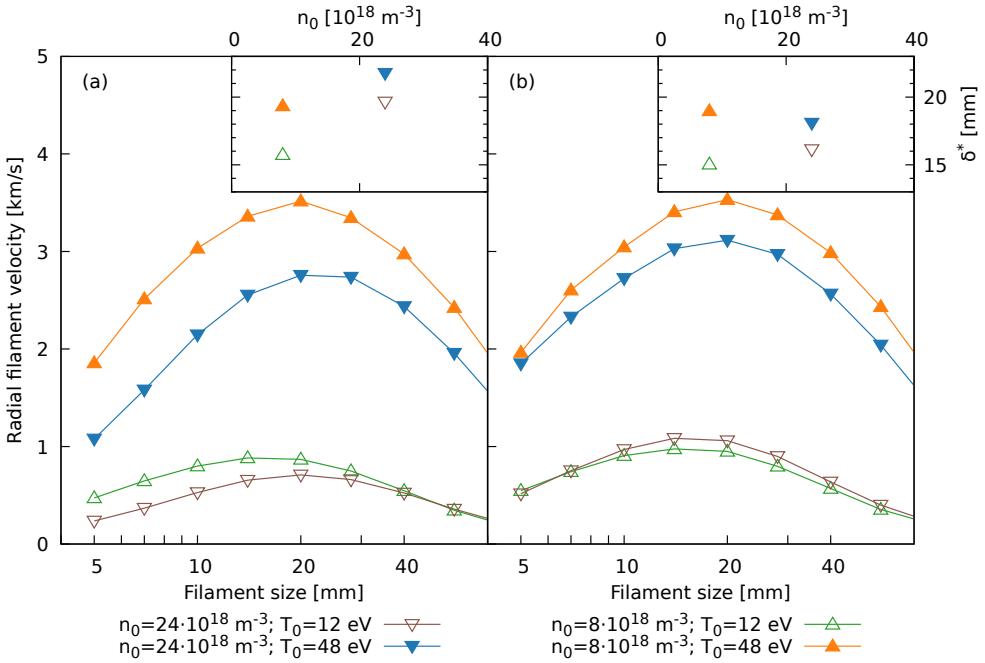

Figure 5.15: Radial velocity of different sized filaments. Shown is the peak velocity for the four backgrounds from fig. 4.5. The filaments on the left (a) are evolved with self consistent plasma viscosity and on the right (b) with the density dependence of the plasma viscosity removed. On the top right in (a) and (b) the critical size is plotted against the upstream density for the different cases using the same symbols.

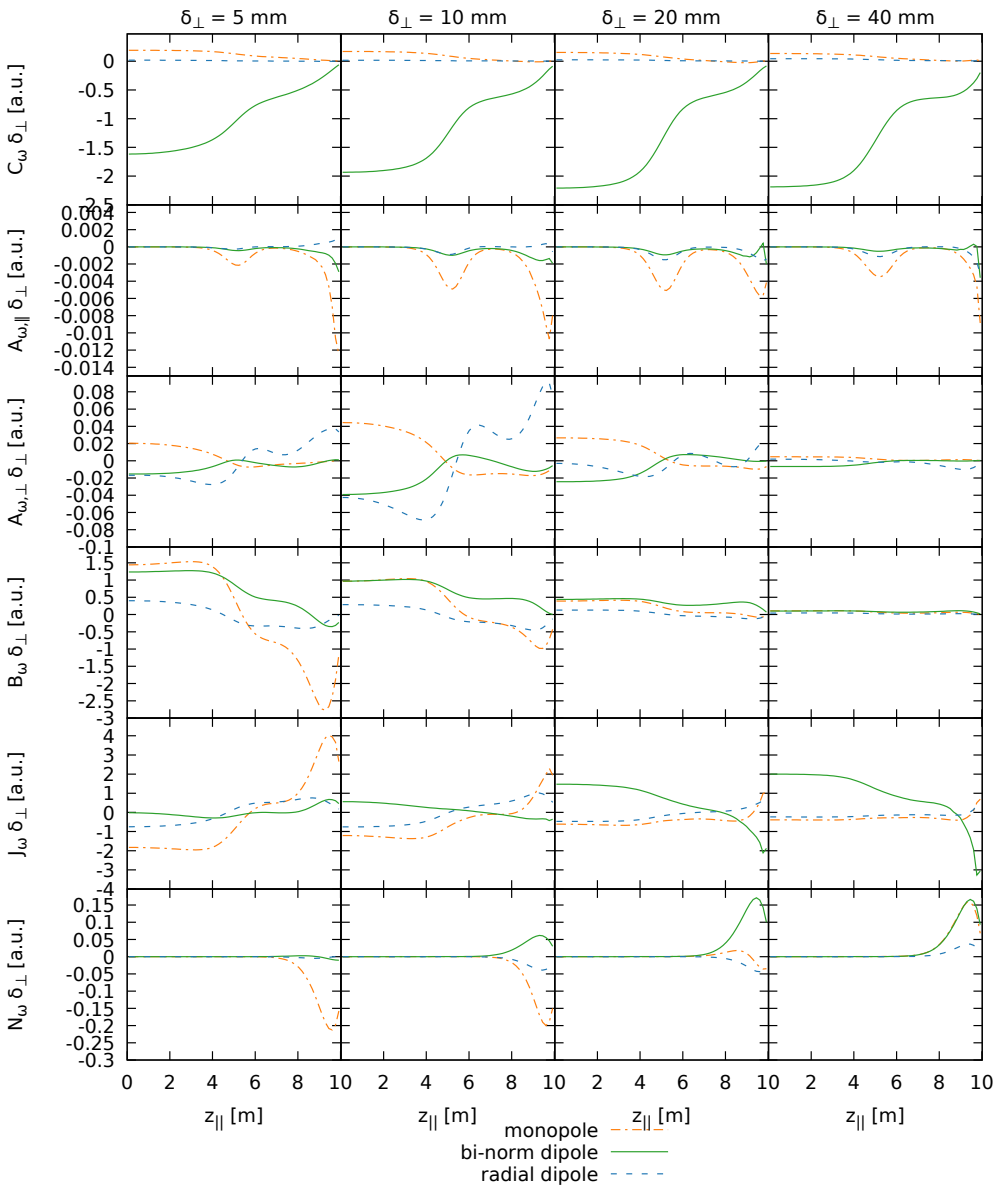

Figure 5.16: Contribution of the different terms in the vorticity equation (3.44). The different parts are decomposed as described in sec. 3.5.2. The contributions are analysed as the filament reaches peak velocity. Different filament sizes are analysed, all having an upstream temperature $T_0 = 12\,\mathrm{eV}$ and upstream density $n_0 = 8 \cdot 10^{18}\,\mathrm{m}^{-3}$. All quantities are plotted on the same scale.

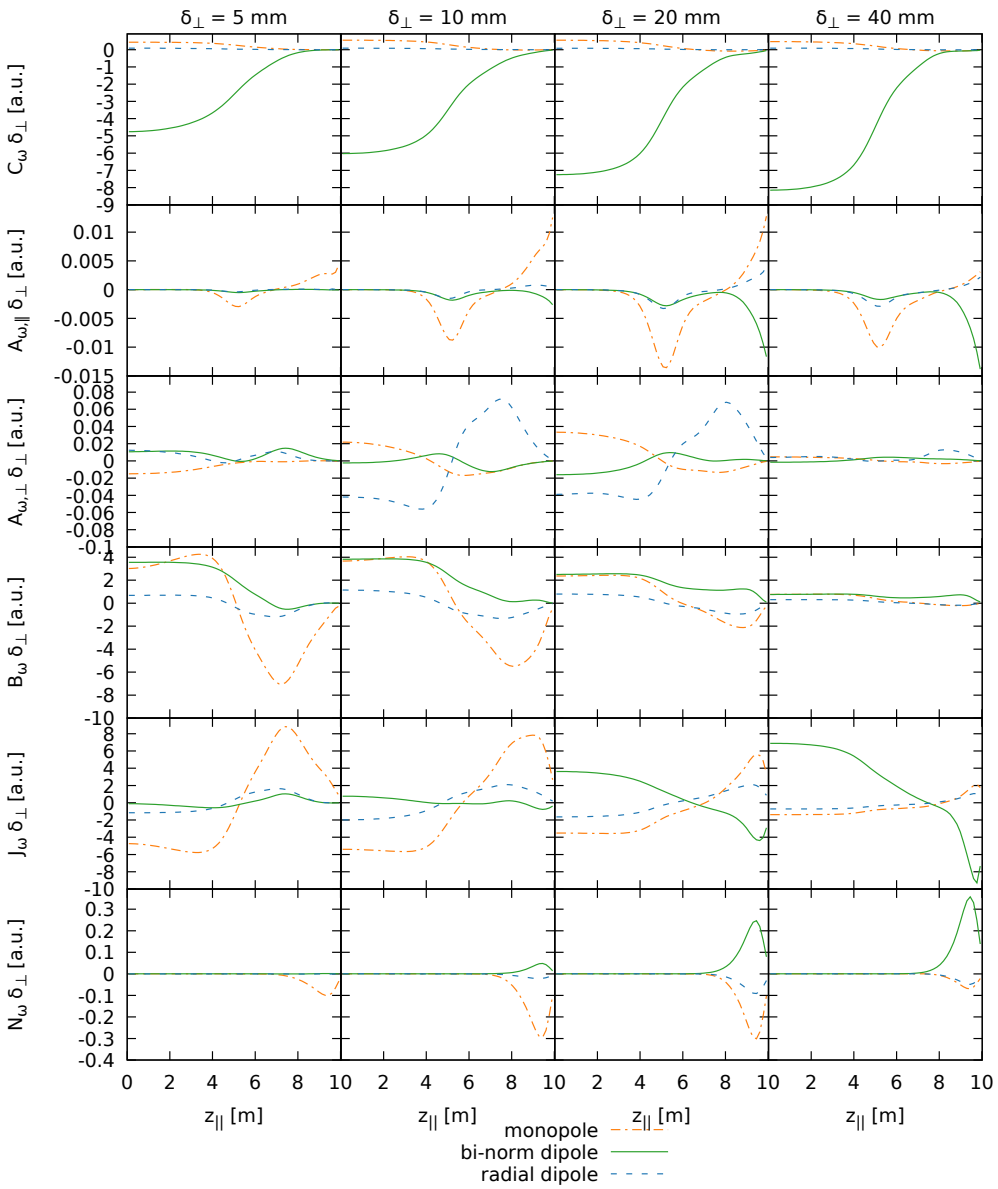

Figure 5.17: Contribution of the different terms in the vorticity equation (3.44). The different parts are decomposed as described in sec. 3.5.2. The contributions are analysed as the filament reaches peak velocity. Different filament sizes are analysed, all having an upstream temperature $T_0 = 12\,\mathrm{eV}$ and upstream density $n_0 = 24 \cdot 10^{18}\,\mathrm{m}^{-3}$. All quantities are plotted on the same scale.

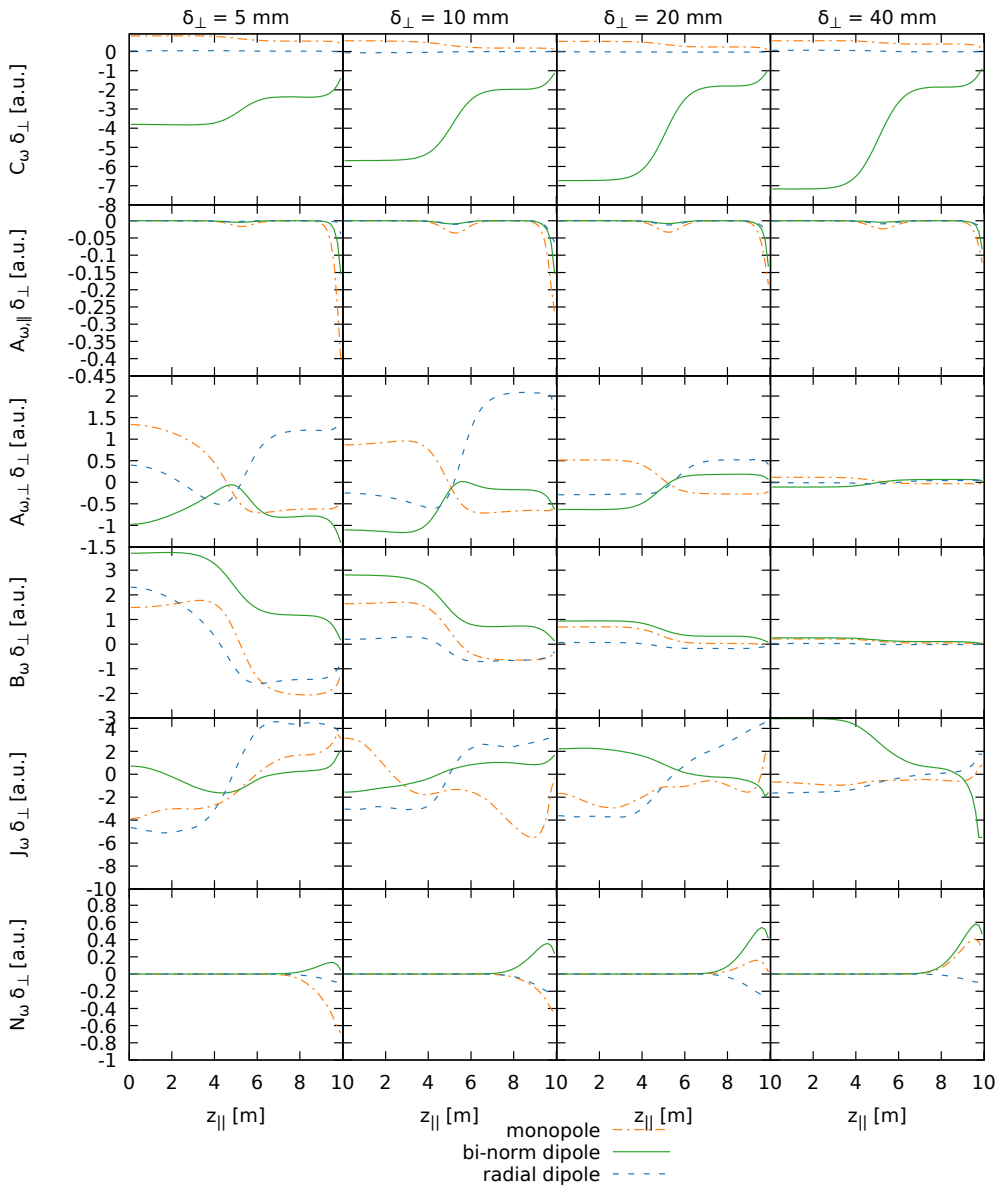

Figure 5.18: Contribution of the different terms in the vorticity equation (3.44). The different parts are decomposed as described in sec. 3.5.2. The contributions are analysed as the filament reaches peak velocity. Different filament sizes are analysed, all having an upstream temperature $T_0 = 48\,\mathrm{eV}$ and upstream density $n_0 = 8 \cdot 10^{18}\,\mathrm{m}^{-3}$. All quantities are plotted on the same scale.

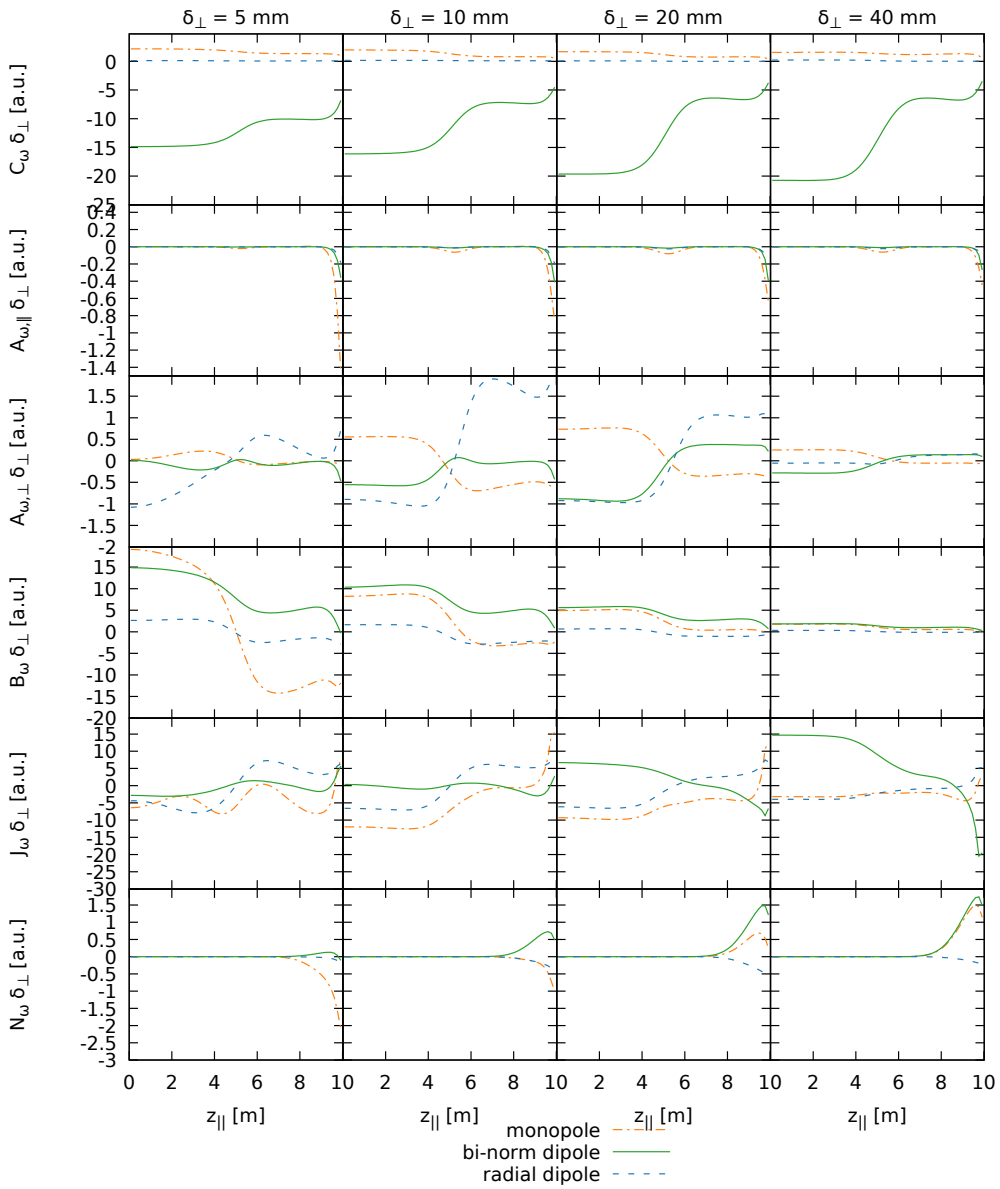

Figure 5.19: Contribution of the different terms in the vorticity equation (3.44). The different parts are decomposed as described in sec. 3.5.2. The contributions are analysed as the filament reaches peak velocity. Different filament sizes are analysed, all having an upstream temperature $T_0 = 48\,\mathrm{eV}$ and upstream density $n_0 = 24 \cdot 10^{18}\,\mathrm{m}^{-3}$. All quantities are plotted on the same scale.

ditions in sec. 5.2.2, a scan where the plasma viscosity has no density dependence was performed. This is shown in fig. 5.15 (b). Similar to (a), the fitted position of the critical size is shown in the top right corner. With increasing density, the critical size shows no systematic increase. Only the temperature dependence is reduced. This shows that the density dependence of the critical size observed in (a) is due to the density dependence of the plasma viscosity, which has not been included in past studies. Further, a weak temperature dependence of δ^* is observed. From the simple scaling derived in section 2.2.4, a temperature dependence but no density dependence is expected, suggesting that future derivations of δ^* should include a self consistent plasma viscosity, and currents due to viscosity.

The stronger density dependence of small filaments can be explained by the density dependence of the viscosity. This can be seen in figs. 5.16 to 5.19. Note that figs. 5.16 to 5.19 are normalised by the filament size. As the drive term C_ω have a $\delta_\perp^{-1}$ dependence, all terms would be smaller for the larger filaments. This would make it much harder to compare them. Instead the normalisation allows one to compare non-trivial changes more easily.

As for small filaments the currents are closed via currents in the drift plane, where viscous currents can contribute. In the case of small filaments the current contribution J_ω has no significant dipole contribution, nevertheless a monopole contribution is observed in figs. 5.16 to 5.18. The remaining dipole current is transporting within the filament from the midplane towards the filament front. As the filament is hotter, there is less resistance within the filament than in the plasma outside of the filament. For large filaments, the viscosity contribution is small and as such no dependence on the viscosity is observed, as the currents are closed via the

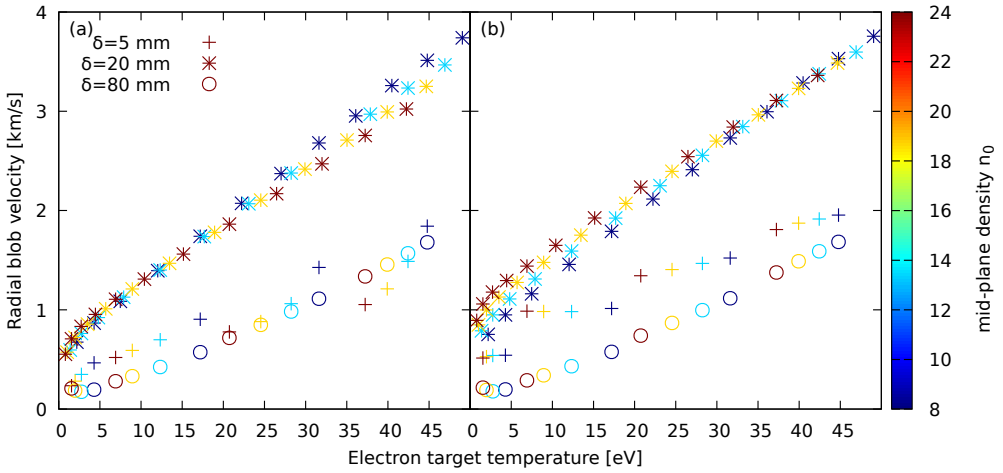

Figure 5.20: Radial velocity of different sized filaments. Shown is the peak velocity as a function of target temperature for different sized filaments. The viscosity is included self-consistent in (a), while in (b) the density dependence is removed. The $\delta_\perp = 20\,mm \approx \delta^*$ are similar in size to the ones observed in MAST. Small filaments are denoted by a plus, critical sized filaments by a star, and large filaments by an open circle. The upstream density is colour coded, see colour-bar.

sheath. In this case the bi-normal dipole contribution in J_ω is dominating, and the monopole contribution can be neglected.

The advective contribution is in all cases small, as shown in figs. 5.16 to 5.19. The parallel perpendicular advection $A_\omega^\perp$ due to $E \times B$ is only for the hot cases $T_0 = 48\,\mathrm{eV}$ not small.

Fig. 5.20 shows the peak radial velocity for different sized filaments. The ones with size $\delta_\perp \approx \delta^*$ are the fastest ones. The smaller ones and larger ones are significantly slower. The larger ones collapse on a line, as they are plotted against the target temperature. This agrees with theory, as the vorticity for larger filaments is mainly closed via sheath currents, therefore a dependence on the sheath conditions is expected. The smaller ones, where the currents are closed mainly via currents in the drift plane, show a stronger dependence on the density. This strong density dependence

can be explained by the viscosity. If the density dependence of the viscosity is removed, they do not collapse that closely onto a single line, as shown in fig. 5.20(b). This suggests a weaker target dependence compared to larger filaments. As this geometry does not include an X-point, filaments can be connected to the target, and therefore influenced by the target. If a more realistic geometry is used, it is quite likely that at least for the smaller filaments the influence of the plasma conditions at the sheath is further reduced compared to larger filaments, as in that case the monopole part of the current contribution should be also suppressed.

5.3 Summary

Filament radial velocities in the scrape-off layer for different background profiles have been studied. The upstream temperature and density have been varied, resulting in self consistent parallel profiles. The backgrounds do not include gradients in the radial direction. Filaments were seeded on the background profiles, and the radial filament velocity was measured.

It has been shown, that the direct interaction between the filament and the neutrals is strongest in the high density and high temperature case, where a weak reduction of velocity was observed, agreeing with the prediction by Theiler et al. [92]. As the filament motion depends on the background profiles, all filaments were subject to indirect neutral influences via the dependence of the background profiles on neutrals. To accurately capture filament dynamics, the parallel variation of the background plasma, including interactions with the neutral population, should be included.

Increasing the upstream temperature resulted in faster radial motion of the filament. The radial velocity also decreased with increasing upstream

density. This can be explained by the reduced target temperature with increasing density, as the target temperature was shown to be the best ordering parameter for the filaments studied here. The filament perturbation is seeded in a manner such that it is initially unconnected to the sheath. It is the fast electron motion that connects the filament electrically to the sheath. This way the target temperature dependence can be explained by the temperature dependence of the plasma viscosity and by sheath currents.

The strong target temperature dependence is not only observed for filament sizes close to the critical size δ^* but also for larger ones. Here the bulk of the vorticity is closed via sheath currents. Smaller filaments show a strong dependence on plasma density, due to the density dependence of the plasma viscosity. If this influence is reduced, they show also a strong dependence on the sheath temperature. Further a shift of δ^* with density is observed. This is not expected from scaling laws, but can be explained by the density dependence of the plasma viscosity. This suggests that the plasma viscosity should be included if scalings for δ^* are derived.

CHAPTER 6

Filament dynamics in detached conditions

This chapter studies the dynamics of filaments in detached conditions. This extends the study from chapter 5 of the impact of the plasma background on filament dynamics. The background profiles pertaining to the study of detachment have been presented and discussed in sec. 4.4. As mentioned on the introductions of the backgrounds, the filaments are not expected to be overly sensitive on the details of detachment. The main contributions are expected from the high plasma density and low plasma temperature and only to a certain extend from the neutrals. As future work, this could be verified using a more detailed neutrals model.

6.1 Introduction

As discussed in sec. 1.5.3, a major challenge for the operation of fusion devices, such as ITER, is the power handling in the divertor. ITER will thus have to operate in detached, or at least partially detached conditions [63]. Detachment is an operational regime in which the heat and particle target fluxes are reduced, as a significant part of the plasma is cooled before it can reach the target [147, 156]. Detached conditions require a drop of total plasma pressure along the flux tube. Charge-exchange can be an efficient sink for plasma momentum as well as a sink for the plasma energy, reducing the heat load at the target, as well as reducing the density flux.

The importance of the dynamics of filaments for the plasma profiles has already been discussed in sec. 2.1.2. However, the dynamics of filaments in detached conditions is not fully understood, even though this is the expected operation regime for ITER and future fusion devices.

As detachment is reached the plasma temperature drops significantly in the vicinity of the target. This causes an increased plasma resistivity. Easy et al. [121] found by introducing an artificially increased resistivity that the radial filament velocity increased. As well as increased radial velocity, an increased critical size δ^* was observed with increasing resistivity [121].

Filaments are a significant cross field transport mechanism and have been shown that they significantly influence the time averaged profiles [36, 107]. At the same time filaments depend on the background condition, as demonstrated in chapter 5. In order to understand this non-trivial interaction, an increased understanding of filament dynamics in detached conditions is required.

As shown in the previous chapter 5, realistic background profiles can

have a significant impact on the dynamics of filaments, where a strong dependence of the target temperature has been observed in attached conditions [126]. In the attached conditions, only a weak influence of neutrals on the dynamic of filaments has been observed. The increased resistivity by a decreased temperature did not result in an increased velocity, as the change in target temperature had a stronger effect [121, 126], shown in fig. 5.6

This chapter aims to extend the previous chapter into detached conditions, as it is expected that the filament-neutrals interaction will become important in the higher density cases. This also allows one to extend the resistivity of the background plasma in a self-consistent way to levels studied by Easy et al. [121].

The model used was introduced in chapter 3 including the neutrals model retaining parallel dynamics 3.4.2. The background profiles showing detachment, that are used in this chapter as input for the filament simulations are presented in sec. 4.4. Filaments were seeded on the backgrounds as discussed in sec. 3.3 as a Gaussian perturbation in the drift plane, and with a tanh shape in the parallel direction, where the length was chosen as 5 m. In the perpendicular direction a Gaussian width of $\delta_\perp = 2\,\mathrm{cm}$ was chosen for the study of the direct impact of the neutrals on filament dynamics in sec. 6.2, as well as for the study of the impact of detachment on the radial filament velocity in sec. 6.3. The perpendicular size $\delta_\perp$ was later varied to study the roll of $\delta_\perp$ in sec. 6.4.

In sec. 6.5 the rigidness of the filaments in detached conditions is studied, before the results are discussed in sec. 6.6.

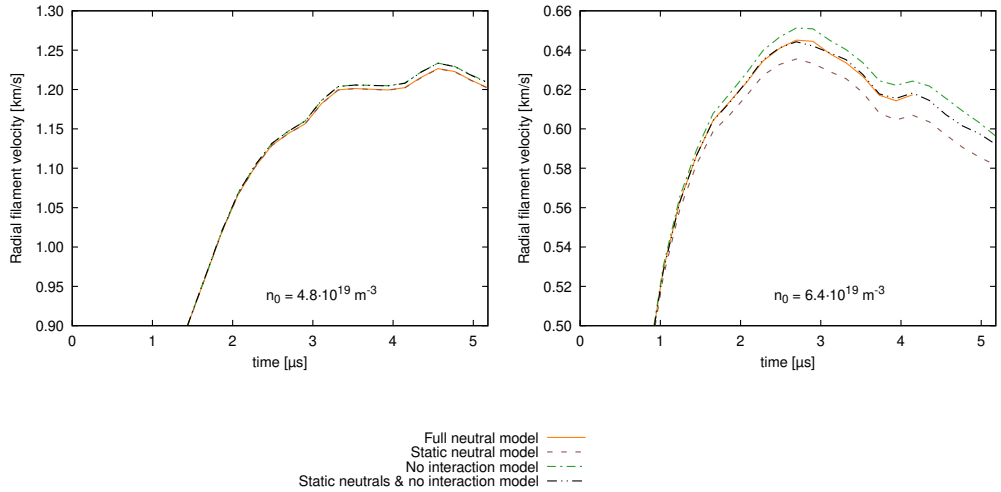

Figure 6.1: Time evolution of the radial velocity of a filament seeded on the background with $10\,\mathrm{MW/m^2}$ and $n_0 = 48 \cdot 10^{18}\,\mathrm{m^{-3}}$ (left) as well as $n_0 = 64 \cdot 10^{18}\,\mathrm{m^{-3}}$ (right), shown in fig. 4.10(d,b). Results for different neutrals model are shown, see legend.

6.2 Direct influence of neutrals

Similar to the study in attached conditions in sec. 5.2.1, the direct influence of neutrals on the dynamics of filaments has been studied in detached conditions. Fig. 6.1 shows the time evolution of the radial velocity of a filament seeded on the high density backgrounds $n_0 = 48 \cdot 10^{18}\,\mathrm{m^{-3}}$ and $n_0 = 64 \cdot 10^{18}\,\mathrm{m^{-3}}$ in the $10\,\mathrm{MW/m^2}$ case, shown in fig. 4.10(b,d). The no-interaction models in all cases show faster radial filament velocity than the version that includes the vorticity-neutral interaction, however the effect is below 1 % in the $n_0 = 64 \cdot 10^{18}\,\mathrm{m^{-3}}$ case and not noticeable in the lower density cases.

In the $n_0 = 48 \cdot 10^{18}\,\mathrm{m^{-3}}$ case, keeping the neutrals static has no effect. In the $n_0 = 64 \cdot 10^{18}\,\mathrm{m^{-3}}$ case where the cold detachment front is within the seeded filament, the static neutral simulation over-estimates the influence of the neutrals by about 1.5 %. This can be explained by looking at the

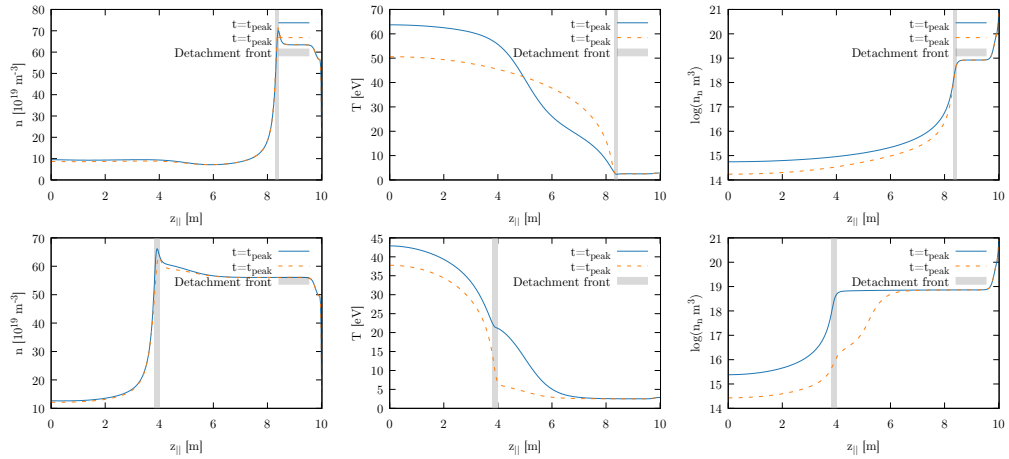

Figure 6.2: Plasma profiles at the centre of the filament. Shown in blue are the profiles just at the beginning of the simulation, before the neutrals could adjust to the perturbation. Shown in red are the profiles after $\approx 4\,\mu s$. Shown is the plasma density (left), electron temperature (centre) and neutral density (right). On the top is the $n_0 = 48 \cdot 10^{18}\,\mathrm{m}^{-3}$ case, and on the bottom the $n_0 = 64 \cdot 10^{18}\,\mathrm{m}^{-3}$ case, both with $10\,\mathrm{MW/m^2}$ energy influx, as shown in fig. 4.10(d,b) The detachment front is shaded in grey.

plasma profiles, shown in fig. 6.2. In the $n_0 = 48 \cdot 10^{18}\,\mathrm{m}^{-3}$ case the cold plasma region does not extend into the seeded filament, and thus the neutral density is rather low in the seeded filament. In the $n_0 = 64 \cdot 10^{18}\,\mathrm{m}^{-3}$ case, the filament is seeded within the cold plasma region which includes a high neutral density. Thus in the $n_0 = 64 \cdot 10^{18}\,\mathrm{m}^{-3}$ case a significant amount of neutrals are ionised by the filament, unlike in the $n_0 = 48 \cdot 10^{18}\,\mathrm{m}^{-3}$ case. The difference in the neutrals density results in a difference in the neutral interaction rates Γ^{CX} and Γ^{ion}, which in turn has an impact on the vorticity equation (3.44), namely via the neutrals term (3.50). Thus by ionising the neutrals, the filament reduces the neutral friction term significantly. In the no-interaction case, only indirect interactions remain. In the static neutrals case the neutrals are more effective at cooling, than in the case where the neutrals are allowed to be ionised. This is similar to the direct

interaction in attached conditions, shown in fig. 5.3, however the difference between the models is here increased, as the neutral density is increased. Experimentally, this is not expect to be a significant contribution, as the filament ionises the neutrals, as the filament penetrates into the detached volume. The indirect interaction, e.g. by cooling the filament as it heats the detached plasma, are probably more relevant.

6.3 Dependence on detachment

Compared to the filaments studied in the previous chapter, where the filaments where in fully attached conditions, the velocity of filaments in these higher density simulations is decreased [126]. Previously the slowest filament velocity reached was around 550 m/s at an target temperature of 0.8 eV, see e.g. fig. 5.7. Higher target temperatures resulted in faster filament velocities. In the simulations presented here the target temperature does not drop below 2.5 eV, as the recombination acts as a heat source for the electrons at low temperatures, as in this chapter the extended neutral model, introduced in sec. 3.4.2 is used. Fig. 6.3 shows the peak radial filament velocity versus the target temperature. While for the high target temperature cases the previous findings of a target temperature dependence are reproduced, this does not hold for target temperatures below ∼5 eV. The main differences to the study in the previous chapter is the increased plasma density, as well as the energy source from recombination. This leads to a range of filament velocities for a single target temperature during the detached phase and causes the scaling with target temperature to break down

To understand the dependence of the filament velocity in detached con-

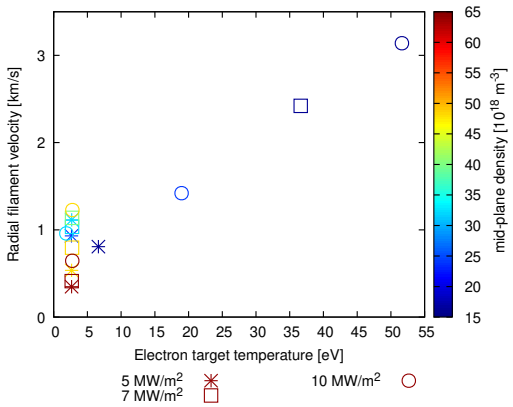

Figure 6.3: Peak radial filament velocity for the backgrounds shown in fig. 4.10 versus target temperature of the background. The target temperature dependency breaks down for target temperatures below 5 eV.

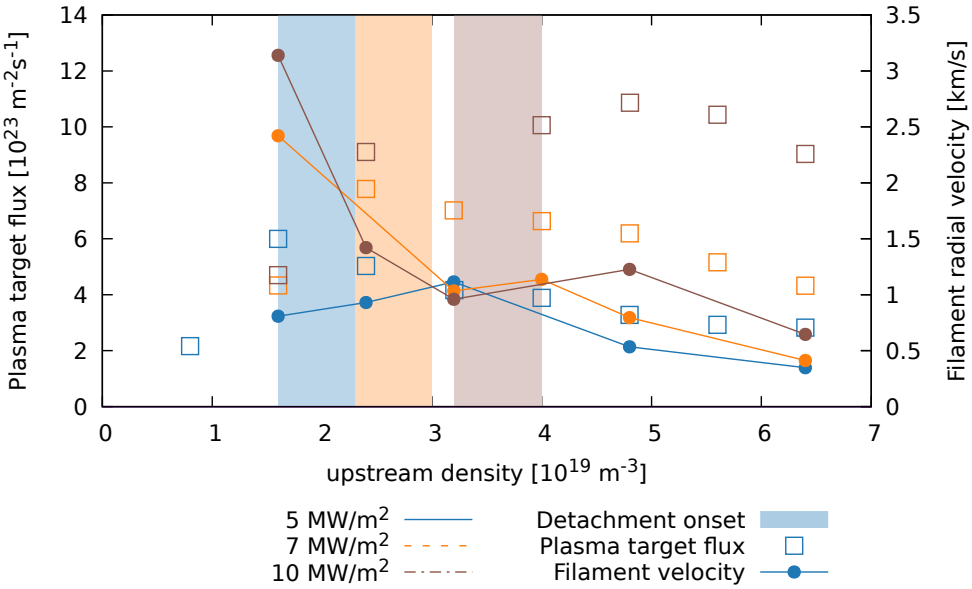

Figure 6.4: On the left axis is the particle target flux of the associated background profiles. On the right axis is the peak radial filament velocity for different plasma backgrounds. The lines are to guide the eye, and do not imply that the transition between the points would be linear. The shaded are represent detachment onset for the different energy influxes. A general decreasing trend of the radial velocity with increasing density is observed, except at the flux roll-over point, where the filaments become temporarily faster.

ditions, fig. 6.4 shows the filament velocity as a function of upstream density, as well as particle target flux of the associated backgrounds. The particle target flux allows one to identify the the roll-over point, and thus the onset of detachment. The filament velocity generally decreases with increasing density. The $5\,\mathrm{MW/m^2}$ case has an exception for densities less than $n_0 = 32 \cdot 10^{18}\,\mathrm{m^{-3}}$, the $7\,\mathrm{MW/m^2}$ case between $n_0 = 32 \cdot 10^{18}\,\mathrm{m^{-3}}$ and $n_0 = 40 \cdot 10^{18}\,\mathrm{m^{-3}}$ and the $10\,\mathrm{MW/m^2}$ case between $n_0 = 32 \cdot 10^{18}\,\mathrm{m^{-3}}$ and $n_0 = 48 \cdot 10^{18}\,\mathrm{m^{-3}}$. The particle target flux roll-over is at $n_0 = 16 \cdot 10^{18}\,\mathrm{m^{-3}}$, $n_0 = 24 \cdot 10^{18}\,\mathrm{m^{-3}}$ and $n_0 = 40 \cdot 10^{18}\,\mathrm{m^{-3}}$ respectively, and as such the detachment onset. In all three cases, with increasing density the target flux roll-over and pressure drop happen, and at even higher densities the radial velocity increases temporarily. This suggests that after detachment is reached, the filaments get faster, before the velocity begins to decrease again. At this point, a cold and dense plasma in front of the target is building up and with increased density as well as decreased temperature, the resistivity is significantly increased, which prevents currents in the filament reaching the target. Fig. 6.5 shows the current density in the centre of the filament, for the $10\,\mathrm{MW/m^2}$ cases. While in the attached cases, the currents flow to the target on the right hand side, in the detached cases the currents are only flowing to the edge of the cold plasma region. The increase of the filament radial velocity with increased resistivity was predicted by Easy et al. [121]. To study the decrease of radial velocity with increasing density, the contributions of the vorticity equation (3.44) was analysed as described in sec 3.5.2. The result is shown in fig. 6.6. The drive term C_ω is increasing with increasing density, that can be in part explained by an increase in upstream pressure with increasing density. Normalising the drive by the upstream pressure $P_0 = n_0 T_0$, an increase, especially for the

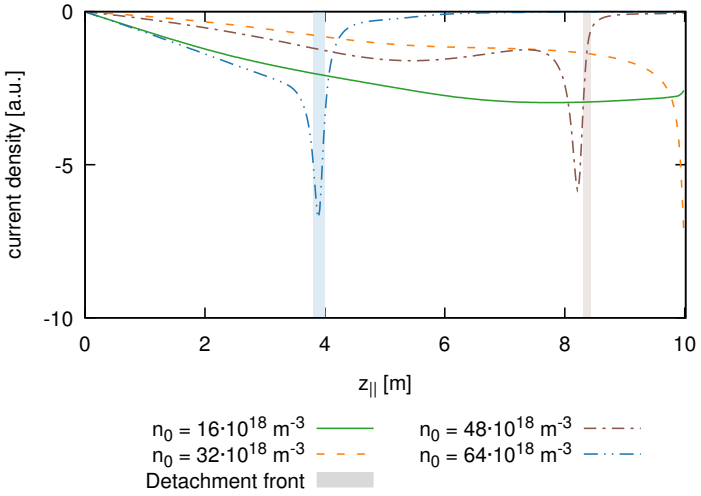

Figure 6.5: Current density at the centre of the filament after ∼4 µs for the 10 MW/m^2 cases shown in fig. 4.10(b,d,f,h). In the detached cases, currents near the target are strongly suppressed. The detachment front is shaded.

$n_0 = 64 \cdot 10^{18}\,\mathrm{m}^{-3}$ case is still observed. Fig. 6.7 shows the density and temperature profiles in the centre of the filament at both $t = 0$ with the seeded perturbation as continuous line, as well as at $t = t_{\mathrm{peak}}$ when the filament reaches its maximum radial velocity as dashed line. Both density and temperature is normalised to its respective upstream value of the background profile. The upstream density perturbation shows in general less of a drop than the upstream temperature perturbation, as parallel transport for the density is significantly slower than for the temperature, where conduction plays a role. As the background density is increased, and the backgrounds transition from low recycling to high recycling and then become increasingly detached, the upstream perturbation shows less of a decrease. Temperature in the low recycling case, $n_0 = 16 \cdot 10^{18}\,\mathrm{m}^{-3}$, is flat by the time $t = t_{\mathrm{peak}}$ is reached. For the deeply detached case $n_0 = 64 \cdot 10^{18}\,\mathrm{m}^{-3}$, the filament cannot transport the perturbation in parallel direction effectively, as the conduction has a strong temperature dependence $T^{\frac{7}{2}}$ and thus cannot con-

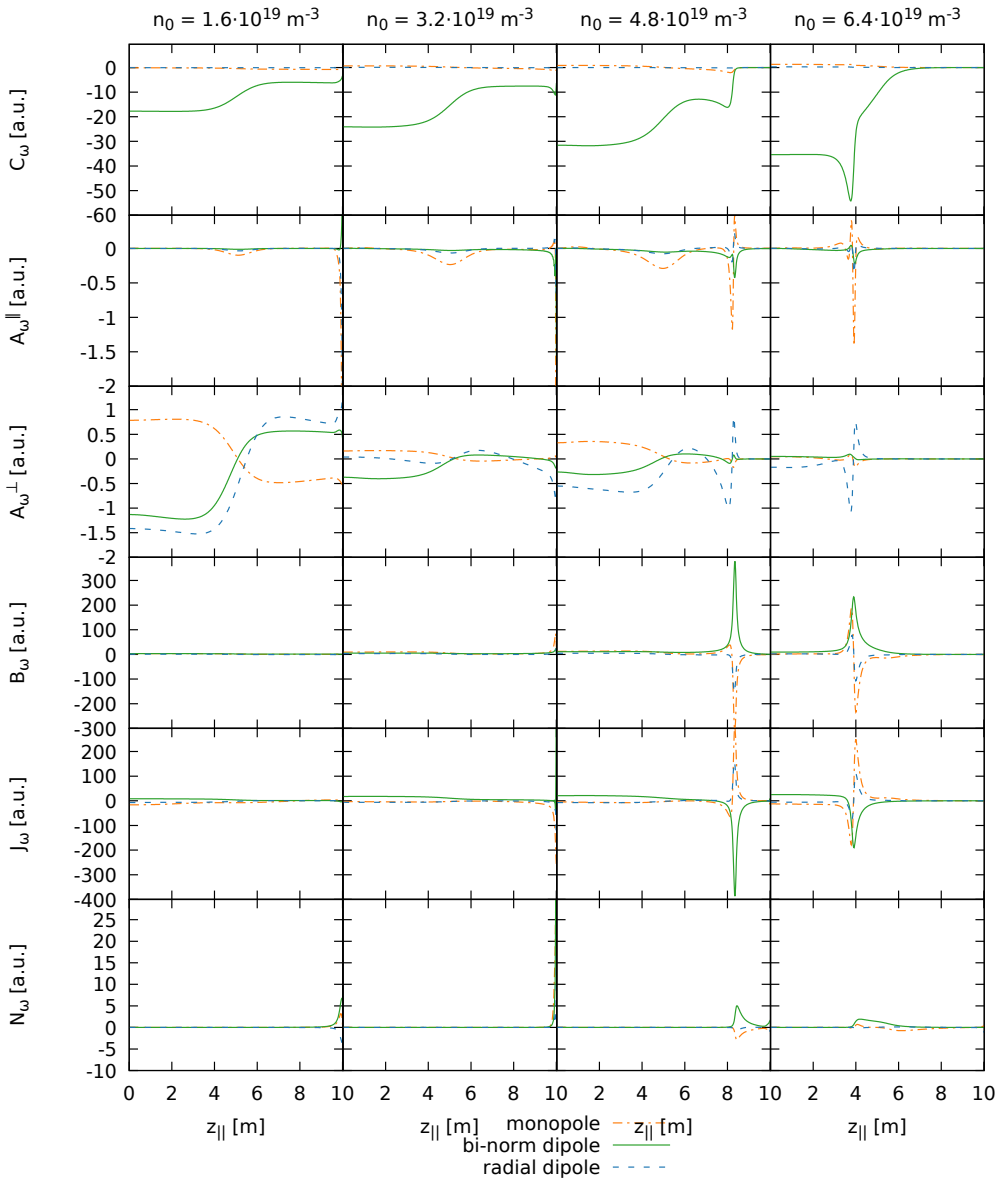

Figure 6.6: Contribution of the different terms in the vorticity equation (3.44). The different parts are decomposed as described in sec. 3.5.2. The contributions are analysed as the filament reaches peak velocity. Different densities are analysed with an energy influx of $10\,\mathrm{MW/m^2}$. All quantities are plotted on the same scale.

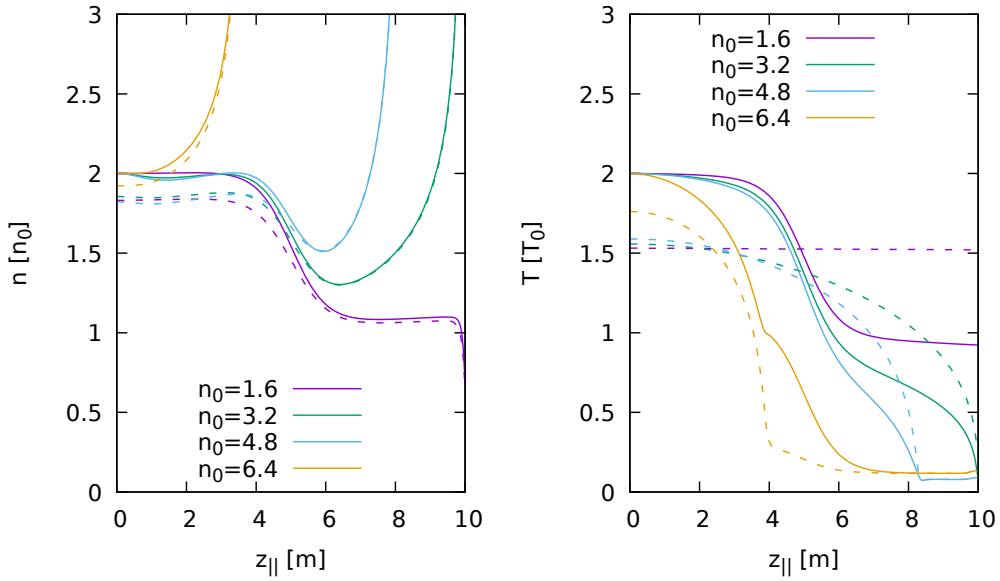

Figure 6.7: Density n and temperature T at the centre of the filament for different densities at an energy influx of $10\,\mathrm{MW/m^2}$. The values are measured within the centre of the filament and normalised to the background upstream value. Full lines show the initial condition just after the filament is seeded, and in dashed is the evolved profile as the filament reaches peak velocity.

duct efficient into the detached region. Similarly, for the deeply detached case, the density perturbation is much less drained than in the attached case.

Even though the drive is increased with increasing density, the velocities are significantly reduced. As the current contribution J_ω and the viscous contribution are strongly peaked, fig. 6.8 shows these two quantities cropped. Fig. 6.8 is also normalised to the upstream dipole contribution of the curvature drive $C_\omega(z = 0)$, unlike fig. 6.6. Note that this changes the sign of all quantities, however it allows one to determine more simply how much of the drive is sunk by which term. From fig. 6.8 it can be seen that viscosity is having an increasing impact as the density increases. While for $n_0 = 16 \cdot 10^{18}\,\mathrm{m}^{-3}$ the viscosity sink is compensating less than 20 % of the drive upstream, the changes to above 30 % for the $n_0 = 48 \cdot 10^{18}\,\mathrm{m}^{-3}$ case. While it might seem that this is reduced for the $n_0 = 64 \cdot 10^{18}\,\mathrm{m}^{-3}$ case as $B_\omega(z = 0)/C_\omega(z = 0)$ is above -0.3, the current J_ω is closing the drive mostly not via the sheath, but via viscosity at the detachment front. As such the 70 % of the upstream drive that is closed via currents, is also closed via viscosity, but at the detachment front. Thus while the resistivity is in general increased with detachment, currents are now more important than in the $n_0 = 16 \cdot 10^{18}\,\mathrm{m}^{-3}$ case, as they current only needs to go to the detachment front.

6.4 Dependence of critical size

The vorticity closing mechanism, and thus the dynamics of filaments strongly depends on the size of the filament with respect to the critical size δ^*. For small filaments, i.e. $\delta_\perp < \delta^*$, the vorticity is closed mostly in the drift

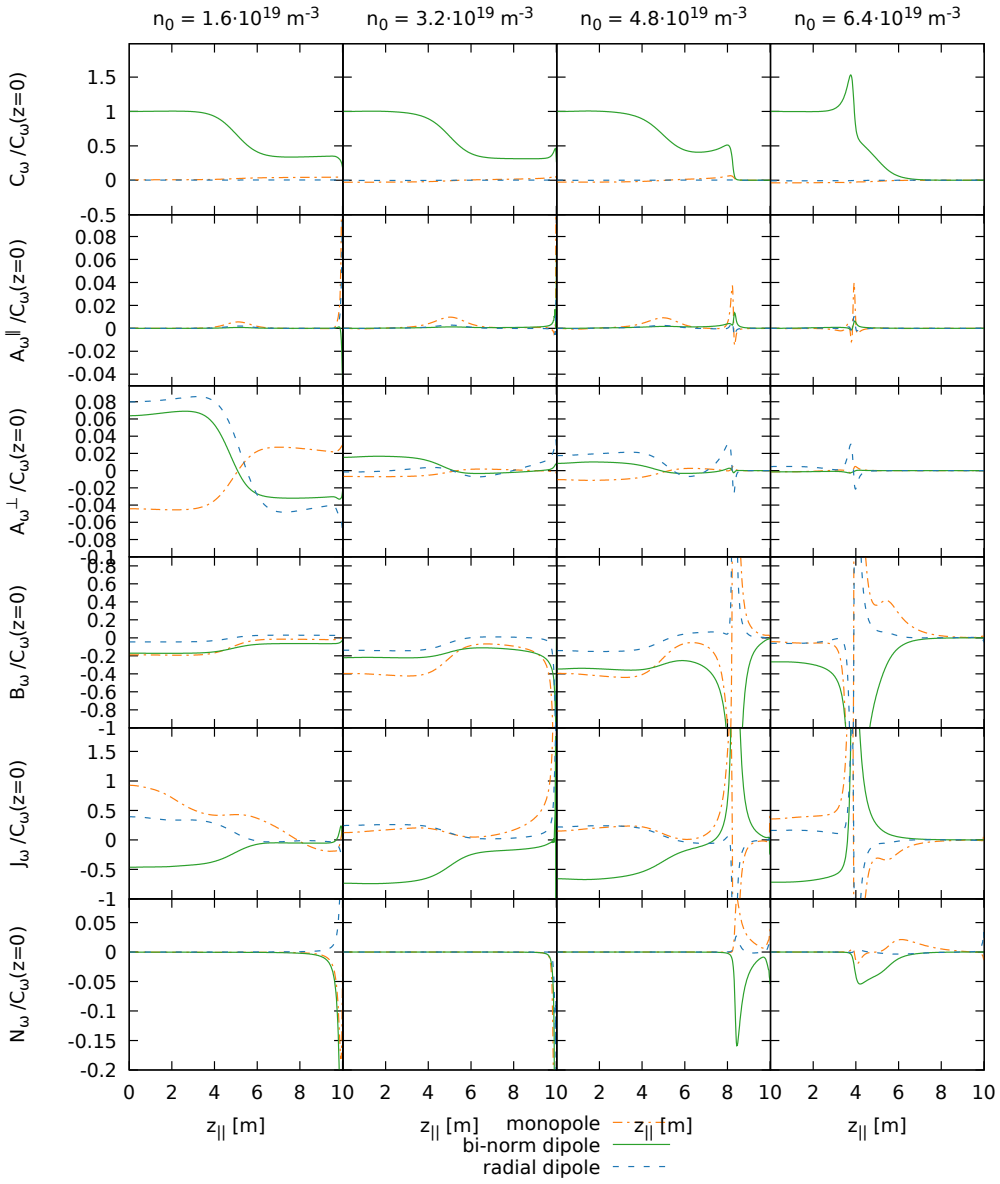

Figure 6.8: Contribution of the different terms in the vorticity equation (3.44). The different parts are decomposed as described in sec. 3.5.2. The contributions are analysed as the filament reaches peak velocity. Different densities are analysed with an energy influx of $10\,\mathrm{MW/m^2}$. All quantities are plotted on the same scale. Unlike fig. 6.6 the quantities are normalised by the upstream curvature drive dipole moment contribution $C_\omega(z=0)$, further B_ω, J_ω and N_ω are cropped.

plane, and the filament velocity increases monotonically with size. For large filaments, the vorticity is closed via parallel dynamics, and a monotonic decrease with filament size is expected, as discussed in sec. 2.2.4.

To further understand the influence of detachment on filament dynamics, different sized filaments where seeded on the background profiles. The results of the filament size scan is shown in fig. 6.9. Also shown is the critical size, as determined by fitting a quadratic function in log-space using gnuplot [155]. Additionally to the full model, a second case is run where the perpendicular viscosity is set to zero. While the perpendicular diffusion constants are physically motivated, the real value is not known. Some models do not include viscosity or diffusion at all [118, 157]. The previous study found a strong viscosity dependence of the filament dynamics, thus the viscosity dependence was once more investigated. The neo-classical viscosity values where assumed to be the upper bound and setting the viscosity to zero is a natural lower bound. Thus the resulting error of this uncertainty is expected to be bound by the full model on one hand, and by the no-viscosity case on the other hand.

In the filament size scan in attached conditions in sec. 5.2.3, the regime transitions from the viscous regime for small filaments to the sheath limited regime for large filaments, where sheath currents are the main current closing mechanism. In detached conditions, for small filaments, the vorticity is mainly closed by viscosity. For large filaments, sheath currents can no longer close the vorticity, as sheath currents are strongly suppressed, as shown in fig. 6.5. The filament scaling expected for neutrals does not have a size dependence. If we set $0 = C_\omega + N_\omega$ we get

$$0 = \frac{g}{n}\frac{\partial nT}{\partial y} - \frac{1}{n}\nabla_\perp^2\phi(\Gamma^{\mathrm{CX}} + \Gamma^{\mathrm{ion}}) - \frac{1}{n}\nabla_\perp\phi\cdot\nabla_\perp(\Gamma^{\mathrm{CX}} + \Gamma^{\mathrm{ion}}) \qquad (6.1)$$

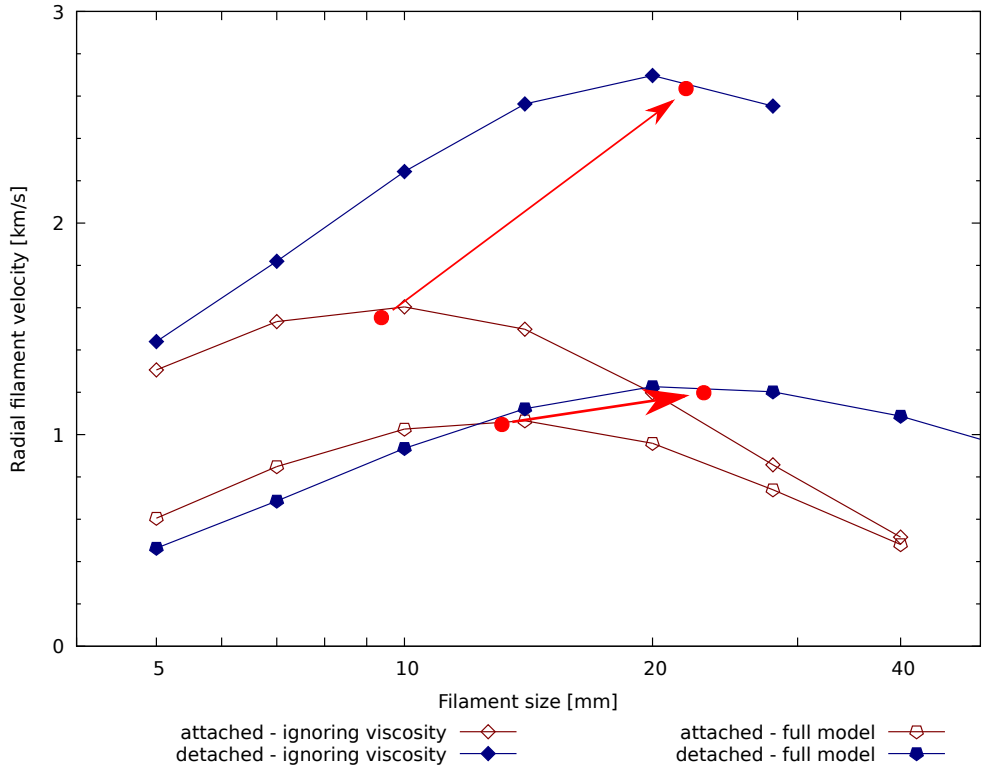

Figure 6.9: Peak radial filament velocity for different sized filaments. The blue, filled symbols are in detached conditions ($10\,\mathrm{MW/m^2}$, $n_0 = 32 \cdot 10^{18}\,\mathrm{m^{-3}}$, fig. 4.10(f)), while the red, open symbols are in attached conditions ($10\,\mathrm{MW/m^2}$, $n_0 = 48 \cdot 10^{18}\,\mathrm{m^{-3}}$, fig. 4.10(d)). The downward pointing triangles are from simulations using the full model, whereas the upward pointing triangles are from simulations ignoring the perpendicular viscosity. The fitted position of the critical sizes are shown as red dots.

we can replace the perpendicular derivatives by $\delta_\perp^{-1}$ and get

$$\approx \frac{gnT}{n\delta_\perp} - \frac{\phi(\Gamma^{\mathrm{CX}} + \Gamma^{\mathrm{ion}})}{n\delta_\perp^2} \tag{6.2}$$

which leads to the radial electric field $E_r \propto \frac{\phi}{\delta_\perp}$ be proportional to

$$\frac{\phi}{\delta_\perp} \approx \frac{gTn}{\Gamma^{\mathrm{CX}} + \Gamma^{\mathrm{ion}}} \tag{6.3}$$

And thus if neutrals are the main sink for the vorticity the velocity is not expected to decrease with increasing size. As with increasing size the monotonic decrease is retained, for filaments larger than the critical size δ^* sheath currents are still important. While the high resistivity strongly reduces sheath currents, sheath currents are not fully suppressed. Due to the increase of the critical size δ^* fewer filaments will be in the sheath limit regime, however the ones that are in this regime will still be able to prevent further acceleration via sheath currents.

The vorticity contributions of the different terms in the vorticity equation (3.44) has been analysed for different sized filament in detached conditions, namely the $n_0 = 48 \cdot 10^{18}\,\mathrm{m}^{-3}$ and $10\,\mathrm{MW/m^2}$ case. The different contributions have been analysed as described in section 3.5.2. The terms have been normalized by the size, as the drive decreases roughly as $\delta_\perp^{-1}$. Otherwise the terms of the large filaments would all be small, making a comparison more difficult. Fig. 6.11 shows the same data as fig. 6.10, but $A_\omega^\perp$, B_ω and J_ω have been cut off. This was done as near the detachment front $z \approx 8\,\mathrm{m}$ strongly peaked profiles are observed. Looking at the contributions of the vorticity equation shown in fig. 6.11, it can be seen that the viscosity contribution B_ω within the filament, i.e. for $z < 5\,\mathrm{m}$, is

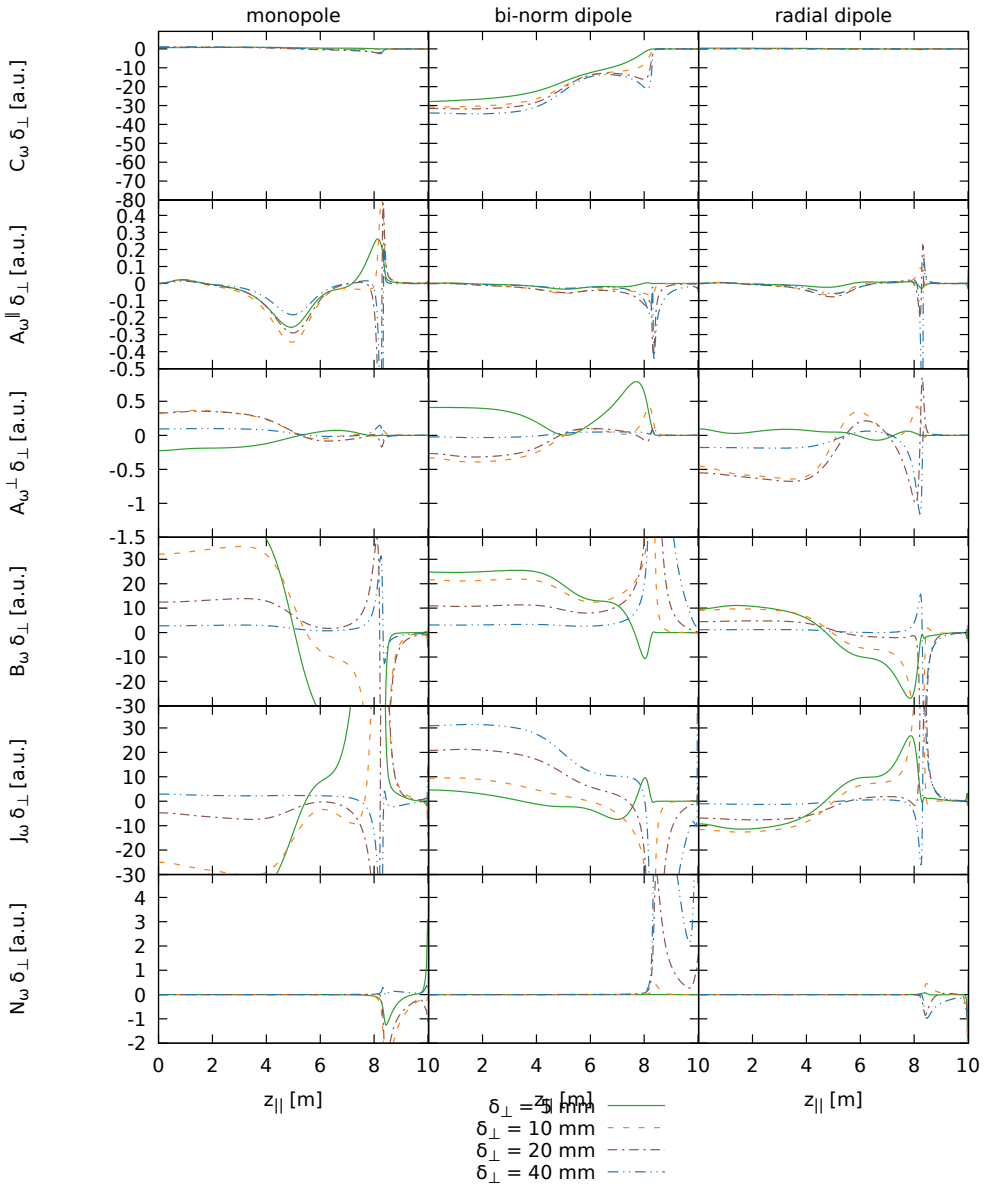

Figure 6.10: Contribution of the different terms in the vorticity equation (3.44). The different parts are decomposed as described in sec. 3.5.2. The contributions are analysed as the filament reaches peak velocity. Different sizes are analysed for the $n_0 = 48 \cdot 10^{18}\,\mathrm{m}^{-3}$ and $10\,\mathrm{MW/m^2}$ case. All quantities are plotted on the same scale, but have been normalised with the filament size $\delta_\perp$.

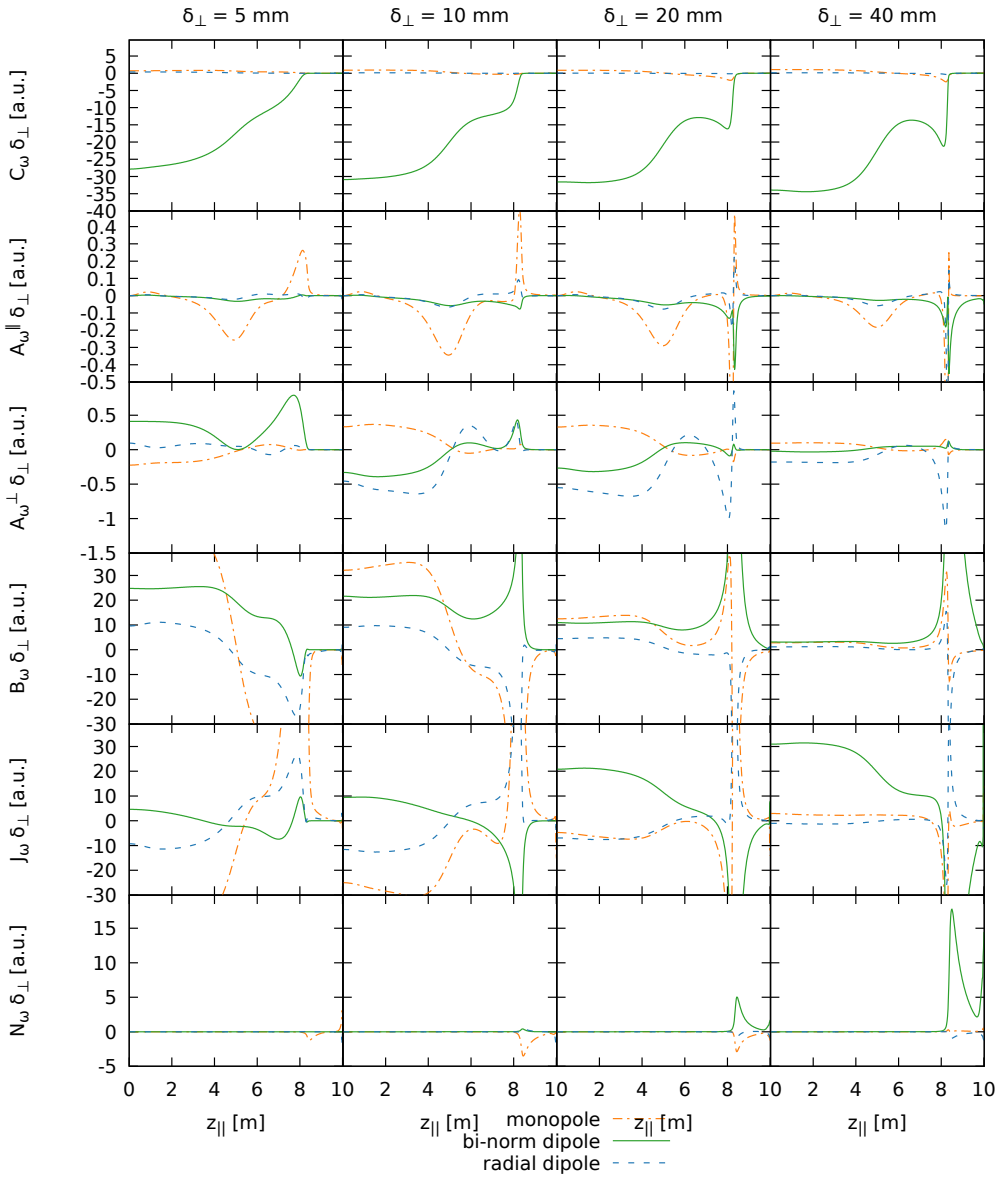

Figure 6.11: Contribution of the different terms in the vorticity equation (3.44). The different parts are decomposed as described in sec. 3.5.2. The contributions are analysed as the filament reaches peak velocity. Different sizes are analysed for the $n_0 = 48 \cdot 10^{18}\,\mathrm{m}^{-3}$ and $10\,\mathrm{MW/m^2}$ case. All quantities are plotted on the same scale, but have been normalised with the filament size $\delta_\perp$. Unlike in fig. 6.10 $A_\omega^\perp$, B_ω and J_ω have been cropped.

significantly decreased for $\delta_\perp \gtrapprox 20\,\mathrm{mm}$. While the viscosity contribution B_ω within the filament decreases with increasing size, the contribution B_ω at the detachment front increases with increasing size, and becomes much larger than the upstream contribution for filaments $\delta_\perp \lessapprox \delta^*$, as can be seen in fig. 6.10. For small filaments the vorticity is closed locally, via B_ω, and non-local effects namely J_ω is less important. For large filaments the vorticity is conducted via J_ω in the direction of the sheath, and as the viscosity is more effective at higher density and lower temperature, the viscosity still provides a significant closing mechanism. Note that rather than the peak magnitude of the contribution, the parallel integrated value represents how much of the vorticity can be sunk by the respective sink. Thus while for small filaments B_ω is rather small, is is extended along the magnetic field lines, and thus provides an comparable large sink, as the peaked contribution for larger filaments.

Note that the current contribution J_ω is not completely vanishing at the target, even though the contribution is decreasing roughly exponentially going further into the detached region, in the $\delta_\perp = 40\,\mathrm{mm}$ case the contribution is still finite at the target. In the attached conditions figs. 5.16 to 5.19 shown in the previous chapter the profiles were not peaked. Also the viscous contribution was mostly within the filament, and only a small peak for the $\delta_\perp = 40\,\mathrm{mm}$ filaments have been observed in some cases just in front of the target, but still smaller in magnitude than for smaller filaments. Whilst the effectiveness of the viscosity closure is decreasing with increasing size, the impact of the neutrals N_ω is increasing. This changes if we do not include viscosity in the model, as shown in fig. 6.12, which is the vorticity contribution analysis for the $n_0 = 48 \cdot 10^{18}\,\mathrm{m}^{-3}$ $10\,\mathrm{MW/m^2}$ case without vorticity. If viscosity is not included, significantly higher velocities

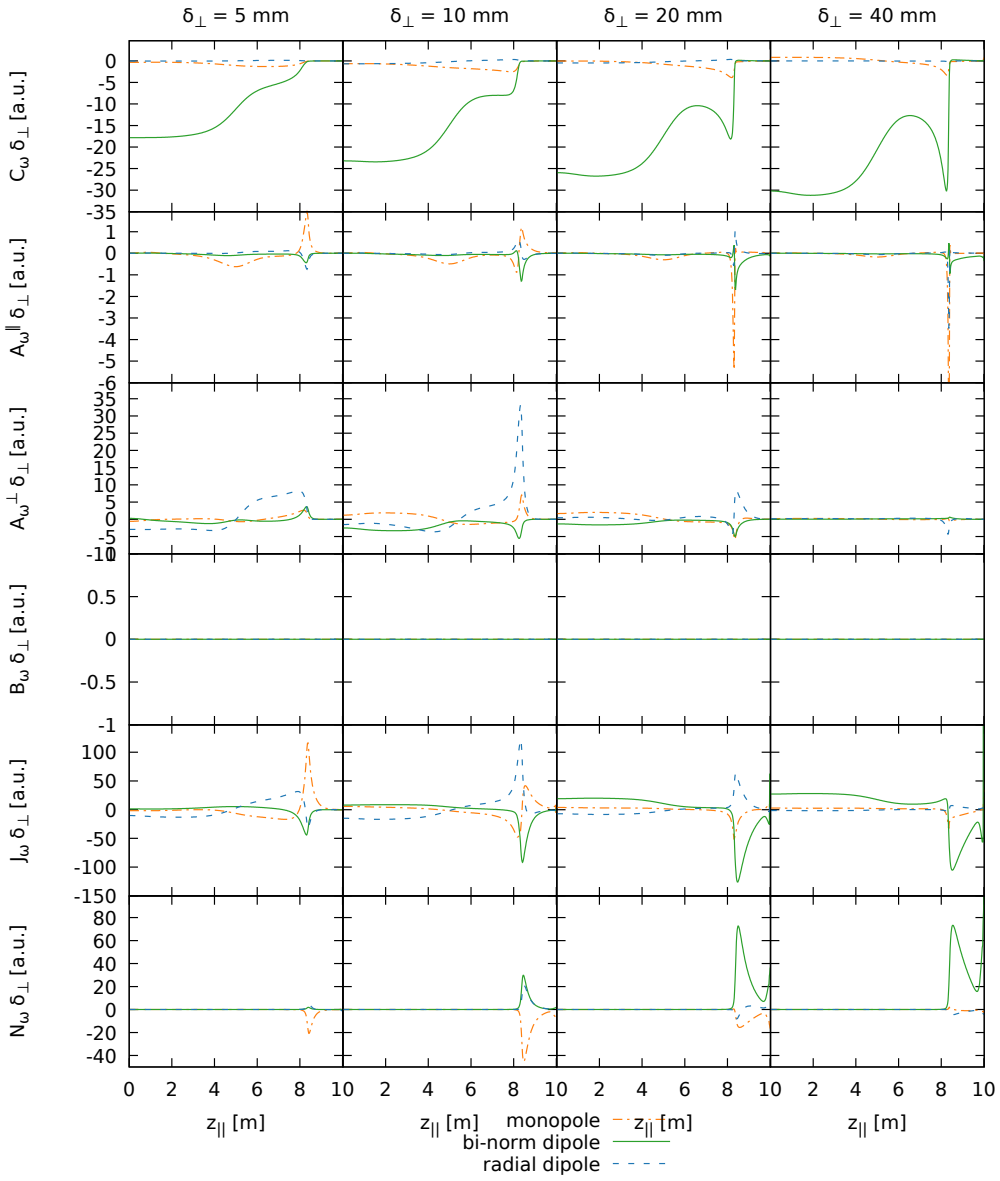

Figure 6.12: Contribution of the different terms in the vorticity equation (3.44). The different parts are decomposed as described in sec. 3.5.2. The contributions are analysed as the filament reaches peak velocity. Different sizes are analysed for the $n_0 = 48 \cdot 10^{18}\,\mathrm{m}^{-3}$ and $10\,\mathrm{MW/m^2}$ case without viscosity. All quantities are plotted on the same scale, but have been normalised with the filament size $\delta_\perp$. Unlike in fig. 6.10 the simulation did not include the viscous term B_ω.

are achieved by the filaments, as shown in fig. 6.9. Similar to the case including viscosity in fig. 6.10, the current term J_ω is conducting towards the detachment front, but unlike in the case with viscosity, where B_ω was the main sink at the detachment front, N_ω is providing the sink for the viscosity. Thus depending on the actual level of viscosity present in experiments, neutrals may be a significant mechanism for closing the current.

In the full model, i.e. with viscosity, the filaments of 14 mm and larger are faster in the detached condition than in attached conditions. This is expected, as small filaments are not influenced by sheath currents, and the increased viscosity, resulting from the higher density in detached state will thus reduce the velocity the filament achieves. For large filaments, the suppression of sheath currents is much more important and the effect of viscosity is weaker, thus they are faster in detached conditions. In the case without viscosity, the filaments of all sizes, down to 5 mm are faster in the detached condition than in the attached case. This indicates that even for the 5 mm filament, in the absence of perpendicular viscosity, parallel dynamics plays a role, as a significant part of the vorticity is advected towards the target. In the low resistivity, attached case, sheath currents provide a monopole contribution, and this $E \times B$ term causes a significant contribution to the vorticity sink. In the high resistivity case, the $E \times B$ contribution is significantly reduced. In that case parallel advection and diffusion are preventing further acceleration of the filament. Therefore in the absence of viscosity, even the small filaments are influenced by the sheath conditions, thus filaments of all sizes achieve higher velocities in detached conditions, where sheath effects are suppressed.

The full model as well as the no viscosity model, shows a higher increase in velocity with detachment for larger filaments. Further, the critical size

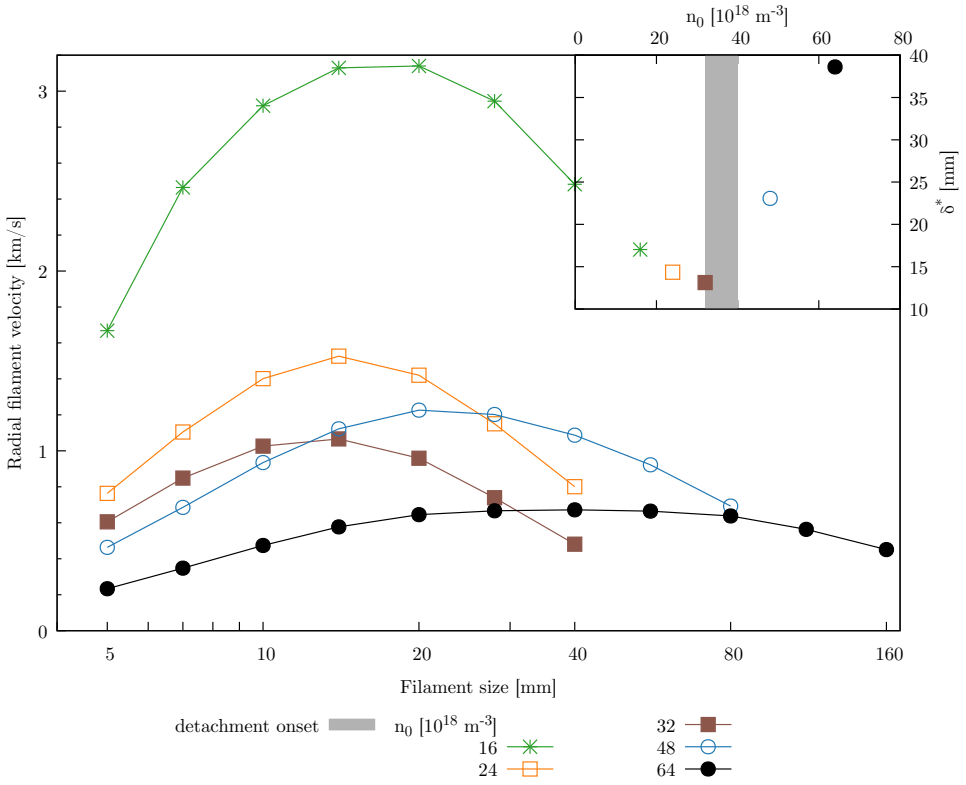

Figure 6.13: Peak radial filament velocity for different sized filaments for different backgrounds. The backgrounds have an energy influx of $10\,\mathrm{MW/m^2}$, and the densities range from $n_0 = 16 \cdot 10^{18}\,\mathrm{m^{-3}}$ to $n_0 = 64 \cdot 10^{18}\,\mathrm{m^{-3}}$. On the top right is the critical size of the different densities. The shaded region denotes the onset of detachment.

δ^* increases significantly with detachment. Note that δ^* is defined as the perpendicular size where filaments are fastest.

To put these results further into context, the scan has been extended to more densities, as shown in fig. 6.13 The density dependence of filaments of $\delta_\perp = 20\,\mathrm{mm}$ has already been discussed in section 6.3. The temporarily increase with detachment onset is the same for all filaments around the critical size and larger, i.e. $\delta_\perp \geq 14\,\mathrm{mm}$. Small filaments, i.e. 10 mm and smaller, show a monotonic decrease with increasing density. In attached

conditions the critical size δ^* decreases with increasing density. This is in contrast to the study presented in the previous chapter, where an increase with increasing density was observed. The main difference between the two studies is, that here the energy influx is kept constant, whereas in the previous chapter, the upstream temperature was kept constant. In the case of a fixed heat flux, an increased density results in an decreased temperature, due to pressure conservation. It seems thus that the decreasing temperature reduces the critical sizes stronger, than the density increases the critical size. As detachment is reached, the critical size δ^* shifts dramatically to larger sizes. This is in agreement with Easy et al. [121], where an increase in the resistivity suppresses sheath currents, as is here observed with detachment. The increase in resistivity reduces the impact of currents, which is especially important for larger filaments. This results in faster radial velocities for larger filaments. The reduced impact of sheath currents also changes the filament size where sheath currents or inertial currents are balanced by sheath currents to larger filament sizes. Fig. 6.13 contains also a plot of the critical size plotted against the respective density. The critical size was determined by fitting a quadratic function against the radial velocity versus logarithm of the perpendicular size using gnuplot [155]. In the $n_0 = 64 \cdot 10^{18}\,\mathrm{m}^{-3}$ case the critical size is further increased with respect to the $n_0 = 48 \cdot 10^{18}\,\mathrm{m}^{-3}$ case, which is already detached. This demonstrates the importance of how far the detachment has moved toward the X-point, which roughly linearly increases the collisionality integrated along the flux tube.

For experimentally observed filaments, it is expected that filaments in detached conditions are generally slower than in fully attached conditions, however not a simple relationship with detachment is expected, but rather

filament size $\delta_\perp$ with respect to the critical size δ^* needs to be taken into account. As filaments around the critical size are typically most stable and observed more frequently than other sizes, with detachment larger filaments are expected.

6.5 Rigidness of filaments

Filaments are typically assumed to be strongly magnetically aligned. This is assumption is for example used for the inversion of the fast imaging data of MAST camera data, to get a projection of the filament in the perpendicular plane. Filaments have been observed to bend in electro-magnetic models, where the pressure perturbation is on the same order as the magnetic pressure [157]. The model used here however uses the electrostatic assumption, and in previous studies, e.g. in the filaments studied in the previous chapter, the filaments have been observed to be rigid. The radial displacement of the filaments seeded on the backgrounds shown in fig. 4.10 has been computed for the different x-y-slices along $z_\parallel$ and is shown in fig. 6.14. The displacement has been normalised by the upstream ($z_\parallel = 0$) displacement. In attached conditions, the velocity has no $z_\parallel$ dependence, and the filament moves rigidly. Also in detached conditions, the filaments in $n_0 = 48 \cdot 10^{18}\,\mathrm{m}^{-3}$ $10\,\mathrm{MW/m^2}$ as well as $n_0 = 32 \cdot 10^{18}\,\mathrm{m}^{-3}$ $5\,\mathrm{MW/m^2}$ still move rigidly. Only the filaments in $n_0 = 64 \cdot 10^{18}\,\mathrm{m}^{-3}$ with $10\,\mathrm{MW/m^2}$ and $5\,\mathrm{MW/m^2}$ as well as $n_0 = 48 \cdot 10^{18}\,\mathrm{m}^{-3}$ $5\,\mathrm{MW/m^2}$ show significant bending. As well as showing a low radial velocity, the filaments that bend have in common that they were seeded partially within the detached region. As resistivity is increased with increasing density and decreasing temperature, the resistivity within the detached region is high. Also if the filament is

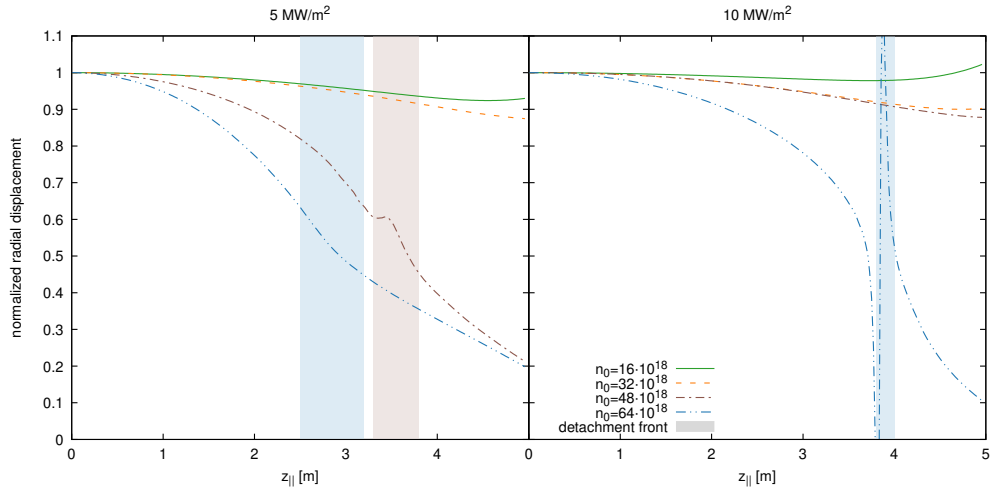

Figure 6.14: Dependence of the filaments radial displacement after 4 µs on the parallel direction $z_\parallel$ for the different backgrounds in fig. 4.10. The displacement was normalised to the displacement at $z_\parallel = 0$. Note that only the upper half of the domain is plotted, where the filament was seeded. The detachment front is represented by a shaded area. In the $n_0 = 64 \cdot 10^{18}\,\mathrm{m}^{-3}$ $10\,\mathrm{MW/m^2}$ case the detection did not work reliably around $z_\parallel \approx 4\,\mathrm{m}$, as the background density features strong parallel gradients, thus small movements of the detachment front making the detection of the centre of the filament unreliable.

seeded within the detached region, the temperature within the detached region quickly reduces, as shown in fig. 6.7, thus increasing resistivity and thus suppressing currents. On the other side, with low temperature and high density, viscosity is increased, resulting in an efficient vorticity sink. As shown in figs. 6.10 and 6.11 the current contribution J_ω is able to conduct vorticity into the detached region all the way to the front of the filament at $z \approx 5\,\mathrm{m}$, but J_ω decreases strongly from the detachment front $z \approx 4\,\mathrm{m}$ to $z \approx 5\,\mathrm{m}$, where the filament ends. As shown in fig. 6.14 the filament is bend not only within the detached region, but also upstream of the detachment front, as the temperature drops already in front of the detachment front. Bending has already been observed in the past, for sufficient low temperature by Walkden et al. [158] or for sufficient high resistivity by Easy et al. [121].

6.6 Discussion

Similar to the previous chapter, strictly in attached conditions, keeping the neutrals fixed at their background values has only a minor impact on the dynamics of filaments. If filaments are able to penetrate into a detached region, they can ionise significant amount of neutrals, which may be relevant to detachment burn-through studies, however [159]. Burn-through has not been studied as part of this thesis, as the neutral code was unstable close to re-attachment.

Easy et al. predicted that a cold divertor could increase the radial velocity of filaments, as well as the critical size δ^* due to a rise in collisional resistivity [121]. While both an increase in radial velocity as well as an increase of δ^* has been observed as detachment is reached, the increase of

the radial velocity is rather weak, and a hotter divertor yields higher radial velocities in general. It has been suggested that detachment, or more generally a high collisionality in the divertor could be the cause of SOL flattening, as the high resistivity could prevent sheath currents, and thus increase the radial filamentary transport [160]. This study shows that collisionality may be responsible for a change of filament dynamics, rather than e.g. the increased neutral density. However, the increase of filament velocities with detachment is well below the radial velocities in sheath limited conditions, so this study does not support the hypothesis that shoulder formation is the result of high divertor collisionality and increased filament transport fluxes. Experimentally also larger filaments have been observed. Assuming that filaments are distributed around δ^*, this is in agreement with this study, as with detachment δ^* is shifted to larger filament sizes.

Furthermore, as a high plasma density as well as a low plasma temperature is required to achieve a sufficiently high resistivity to prevent sheath currents from influencing the filament dynamics, this will most likely not be the case in the far SOL, thus even if the acceleration caused by detachment is higher than suggested by these simulations, the velocity should quickly drop, once the filament is connected to a lower density region and thus can connect to the target.

After detachment occurs, a strong increase of the critical filament size δ^* with increasing density is observed. In attached conditions a weak reduction of the critical size with increased density is observed, which is associated with a reduction of the temperature as the energy influx is kept constant. After detachment occurs, cold and dense plasma at the target is suppressing sheath currents, and with increasing density the detachment volume is increasing, thus increasing the total integrated parallel resistivity. This

shifts the critical size to larger values as predicted by Easy et al. [121]. While neutrals can partially compensate for the lack of sheath currents, the vorticity sink due to neutrals is over an order of magnitude smaller than the sink due to viscosity. The neutrals are acting as a frictional force on the vorticity, and thus providing a sink for the vorticity, similar to the viscosity, however unlike the viscosity without an explicit $\delta_\perp$ dependence. If the viscosity is not included in the simulations, neutrals are the main sink for vorticity, but as the neutrals are less effective at closing the vorticity, higher electric fields, and thus higher radial velocities are observed.

The observed filament bending agrees with Easy et al. [121] where bending was observed if the resistivity was uniformly enhanced, whereas a localised resistivity at the target resulted in a rigid filament [121]. Note that this bending mechanism would only be expected in experiments, if the filament is within the cold, dense plasma region. The bending was only observed in cases where the detachment front has moved quite far upstream, and the filament was within the detached plasma.

Easy et al. [121] increased the resistivity artificially by up to a factor of 10 000 and estimated that the temperature at the divertor would need to drop to 0.086 eV compared to the 40 eV reference case [121]. The estimates assumes that the resistivity has a temperature dependency $\nu_\parallel \propto T^{-3/2}$. However, the resistivity also has a density dependence i.e. $\nu_\parallel \propto n \cdot T^{-3/2}$. If we assume that the pressure $n \cdot T$ is preserved (same upstream conditions but colder divertor) the scaling can be expressed again in terms of the temperature: $\nu_\parallel \propto T^{-5/2}$. Thus achieving the 10 000 increase only requires 1 eV - which is much closer to the temperatures reached here and may explain why the bending effect is seen in the detached simulations.

While Easy et al. [121] predicted that the velocity will be increased

with increased resistivity, the self-consistent simulations conducted here show that the increase with detachment is significantly smaller, than the net decrease with respect to attached simulations, where target temperatures above 25 eV reach velocities exceeding 2 km/s - whereas in detached conditions only about 1 km/s was reached. However, a change in the transition of filament dynamics from inertial or viscous to sheath-limited is observed and the critical size of filaments δ^* increases dramatically after detachment.

6.7 Summary

This chapter presents the dynamic of filaments in detached plasma conditions, using simulations in a 3D slab geometry. The detachment features particle target flux roll over as well as a significant plasma pressure drop. Detachment was achieved by using a refined neutral model, which is able to capture and evolve steep gradients in the neutral density, which is observed near the target.

In terms of dependence of the filament dynamics on the background conditions, a general decreasing trend of radial filament velocity with increasing plasma density is observed. This trend is temporarily broken as detachment is reached, where especially filaments larger than the critical size $\delta^*_{\text{attached}}$ found in attached conditions are faster than before detachment. This is caused by the higher parallel resistivity, which prevents sheath currents, in agreement with Easy et al. [121]. This also causes an increase of the critical size, which further increases as the detachment front moves further upstream and the integrated resistivity increases.

While detachment can increase the radial velocity, the observed radial

filament velocities in hotter, attached plasmas are still faster than the ones observed in detachment, because the previously observed inverse temperature dependence is stronger than the impact of detachment.

CHAPTER 7

Conclusion and Future Work

7.1 Conclusions

Understanding and predicting the transport in the scrape-off layer of tokamaks is of major interest for the design and operation of future fusion devices with the goal to provide a sustainable and high density power source. As filaments are one of the major cross-field transport mechanisms at the plasma boundary, it is of interest to increase the understanding of their dynamics, especially with regard of the conditions expected for future devices, namely high density cases, including divertor detachment, which allows one to reduce parallel heat loads to levels sustainable by the divertor materials.

As part of this thesis, it has been shown that the neutrals do not impact the dynamics of filaments in a significant way in the studied conditions, which included detachment. The neutrals provide a sink for the vorticity,

thus they could reduce the filament velocity, however the plasma viscosity had a higher impact, but this is sensitive to the location of charge exchange with respect to the dense and cold plasma of the detachment front, thus a more accurate neutral model might change this outcome. Beyond the direct neutral-filament interaction, where the neutrals provide a sink for the vorticity, neutrals play a more important role for the dynamics of filaments via changes introduced in the background plasma conditions.

It has been observed that in attached conditions the filament radial velocity has a strong dependence on the target temperature, rather than the upstream temperature. As this was observed for critical sized filaments, this was not expected, as the vorticity is closed by several mechanisms. One of them are sheath currents, which are expected to depend on sheath conditions, and thus a dependence on the target temperature can be expected. Another mechanism, that was found to be important, were viscous currents. The viscosity has a temperature dependence, and is increased with decreasing temperature. While a decreased temperature at the target would allow a more effective vorticity reduction, only in the low density, low temperature case is the vorticity sink at the target due to viscosity comparable with the one upstream. Sheath currents provide in all cases a monopole contribution to the vorticity, which makes the dynamic inherently non-linear, and thus prevents the derivation of a simple scaling law for the target temperature dependence of the filaments radial velocity. The monopole in the vorticity causes a spinning motion of the filament, known as Boltzmann spinning.

This behaviour changes as detachment is reached. There the dependence on the target temperature breaks, and as detachment is reached, a temporary increase of the radial velocity with increasing density is observed, while

in general a decreasing trend with increasing plasma density is observed. The temporary increase is caused by the suppression of sheath currents, due to the high resistivity in the cold plasma adjacent to the sheath. Unlike the study of Easy et al. [121] where the resistivity was artificially increased, this self consistent model does not see an increase of the radial velocity, even though the resistivity is increased to similar levels studied by Easy et al. [121], as the temperature is significantly decreased, resulting in an increased plasma viscosity. This reduces the drive, and thus in general the filaments radial velocity is decreased with decreasing temperature, or with increasing density, which was the controlled parameter in this study.

The critical size of filaments gives insight into how the radial velocity of filaments changes with size. For smaller filaments, the radial velocity increases with size where viscous and/or polarization currents are closeure mechanism. The radial filaments velocity peaks at the critical size where parallel and perpendicular currents are balanced. The velocity decreases again for larger filaments, where currents into the sheath are the dominant closing mechanism. It gives additionally insight into closing mechanisms, and where different mechanisms are balanced. A thorough understanding of the main vorticity closing mechanisms and there dependence in different background conditions allows one to model filaments in stochastic SOL model such as proposed by Militello et al. [36], using only a minimal and computational efficient model to predict the dynamics of single filaments. In attached conditions the critical size of filaments increases slightly with density as well as temperature, where the density dependence is introduced from the density dependence of the viscosity. In the case of the detachment study the energy influx, rather than the upstream temperature was kept constant. In this case with increasing density the critical size δ^* decreased,

this suggests that the decrease caused by the decreasing temperature with increasing density has a stronger impact on the filament critical size δ^* than the increase caused by a decreasing density.

The decreasing trend is broken by detachment, where the critical size increases significantly. This is in agreement with the study from Easy et al. [121] where an increase of the critical size with increased resistivity is observed. As the detachment increases and the detached volume, i.e. cold and dense plasma in front of the target, increases, the critical size is increased to larger sizes. With detachment onset sheath currents are not immediately fully suppressed. As the detached volume increases, the integrated resistivity increases, and sheath currents are increasingly suppressed, and the critical size increases.

Filaments are often assumed to be field aligned. While it is known that this breaks down if the perturbation of the plasma pressure is a significant fraction of the magnetic field pressure, Easy et al. [121] showed that in the high resistivity case, if the high resistivity extends into the filament, the filament is no longer rigid, but moves faster upstream than downstream. This result has been reproduced in self-consistent conditions, where the filament is not any more field aligned if the filament extends into the detached plasma.

7.2 Future Work

The natural progression of this work is to include more realistic backgrounds. In addition to a realistic geometry, the inclusion of kinetic neutrals would be beneficial. Comparing with a kinetic neutrals code such as EIRENE would allow to verify the accuracy of the neutrals model used at

hand. While evolving EIRENE on the time scale of the filament dynamics is expensive, the current study suggests that this is not needed to capture the dynamics of filaments.

As MAST-Upgrade is expected to reach detachment, an experimental comparison would also be beneficial. While comparison of filament dynamics measured in experiments and SOL codes has been done in the past [96, 124], this has not been done for filaments in detached conditions.

Besides increasing the understanding of filament dynamics via increasing the model complexity, the model results can be applied to the stochastic SOL model to compare to experimental measurements of SOL profiles in detached conditions, which would allow an indirect comparison with experiments.

Bibliography

[1] Gian-Reto Walther, Eric Post, Peter Convey, Annette Menzel, Camille Parmesan, Trevor J. C. Beebee, Jean-Marc Fromentin, Ove Hoegh-Guldberg, and Franz Bairlein. Ecological responses to recent climate change. *Nature*, 416:389 EP –, Mar 2002. doi: 10.1038/416389a. Review Article.

[2] Peter M. Cox, Richard A. Betts, Chris D. Jones, Steven A. Spall, and Ian J. Totterdell. Acceleration of global warming due to carbon-cycle feedbacks in a coupled climate model. *Nature*, 408:184 EP –, Nov 2000. URL `http://dx.doi.org/10.1038/35041539`.

[3] Lesley Hughes. Biological consequences of global warming: is the signal already apparent? *Trends in Ecology & Evolution*, 15(2):56 – 61, 2000. ISSN 0169-5347. doi: https://doi.org/10.1016/S0169-5347(99)01764-4. URL `http://www.sciencedirect.com/science/article/pii/S0169534799017644`.

[4] IEA. Key world energy statistics 2017. doi: http://dx.doi.org/10.1787/key_energ_stat-2017-en.

[5] Jef Ongena. nuka. 61:425, 2017 2016. doi: 10.1515/nuka-2016-0070. URL `https://www.degruyter.com/view/j/nuka.2016.61.issue-4/nuka-2016-0070/nuka-2016-0070.xml`. 4.

[6] Anya Castillo and Dennice F. Gayme. Grid-scale energy storage applications in renewable energy integration: A survey. *Energy Conversion and Management*, 87(Supplement C):885 – 894, 2014.

ISSN 0196-8904. doi: https://doi.org/10.1016/j.enconman.2014.07.063. URL http://www.sciencedirect.com/science/article/pii/S0196890414007018.

[7] Tessa Morris-Suzuki. Touching the grass: Science, uncertainty and everyday life from chernobyl to fukushima. *Science, Technology and Society*, 19(3):331–362, 2014. doi: 10.1177/0971721814548115.

[8] Katharina Gerstenberger. Störfälle: Literary accounts from chernobyl to fukushima. *German Studies Review*, 37(1), 2014. doi: 10.1353/gsr.2014.0026. URL https://muse.jhu.edu/article/542059.

[9] John P. Holdren, D. H. Berwald, Robert J. Budnitz, Jimmy G. Crocker, J. G. Delene, Ron D. Endicott, Mujid S. Kazimi, R. A. Krakowski, B. Grant Logan, and Kenneth R. Schultz. Exploring the competitive potential of magnetic fusion energy: The interaction of economics with safety and environmental characteristics. *Fusion Technology*, 13(1):7–56, 1988. doi: 10.13182/FST88-A25084.

[10] J Wesson, DJ Campbell, JW Connor, RD Gill, J Hugill, CN Lashmore-Davies, GM McCracken, HR Wilson, et al. Tokamaks. 2004.

[11] Alan Turnbull and John Ferron. URL https://www.wou.edu/las/physci/GS361/Energy_From_Fossil_Fuels.htm. Accessed 06 dec 2017.

[12] Dale Meade. 50 years of fusion research. *Nuclear Fusion*, 50(1):014004, 2010. URL http://stacks.iop.org/0029-5515/50/i=1/a=014004.

[13] J D Lawson. Some criteria for a power producing thermonuclear reactor. *Proceedings of the Physical Society. Section B*, 70(1):6, 1957. URL http://stacks.iop.org/0370-1301/70/i=1/a=303.

[14] O. Kaneko, H. Yamada, S. Inagaki, M. Jakubowski, S. Kajita, S. Kitajima, Kobayashi, K. Koga, et al. Extension of operation regimes and investigation of three-dimensional currentless plasmas in the large helical device. *Nuclear Fusion*, 53(10):104015, 2013. URL http://stacks.iop.org/0029-5515/53/i=10/a=104015.

[15] R.C. Wolf, A. Ali, A. Alonso, J. Baldzuhn, C. Beidler, M. Beurskens, C. Biedermann, H.-S. Bosch, et al. Major results from the first plasma campaign of the wendelstein 7-x stellarator. *Nuclear Fusion*, 57(10):

102020, 2017. URL http://stacks.iop.org/0029-5515/57/i=10/a=102020.

[16] G. Grieger and I. Milch. Das Fusionsexperiment WENDELSTEIN 7-X. *Physik Journal*, 49(11):1001–1005, 1993. ISSN 1521-3722. doi: 10.1002/phbl.19930491106. URL http://dx.doi.org/10.1002/phbl.19930491106.

[17] Atsuo Iiyoshi, Masami Fujiwara, Osamu Motojima, Nobuyoshi Ohyabu, and Kozo Yamazaki. Design study for the large helical device. *Fusion Technology*, 17(1):169–187, 1990. doi: 10.13182/FST90-A29179.

[18] Yuhong Xu. A general comparison between tokamak and stellarator plasmas. *Matter and Radiation at Extremes*, 1(4):192 – 200, 2016. ISSN 2468-080X. doi: https://doi.org/10.1016/j.mre.2016.07.001. URL http://www.sciencedirect.com/science/article/pii/S2468080X16300322.

[19] M. Keilhacker, A. Gibson, C. Gormezano, P.J. Lomas, P.R. Thomas, M.L. Watkins, P. Andrew, B. Balet, et al. High fusion performance from deuterium-tritium plasmas in jet. *Nuclear Fusion*, 39(2):209, 1999. URL http://stacks.iop.org/0029-5515/39/i=2/a=306.

[20] Francis F Chen. *Introduction to plasma physics and controlled fusion*, volume 1. Springer, 1984.

[21] Vincent P. Idone, Richard E. Orville, Douglas M. Mach, and W. David Rust. The propagation speed of a positive lightning return stroke. *Geophysical Research Letters*, 14(11):1150–1153, 1987. doi: 10.1029/GL014i011p01150. URL https://agupubs.onlinelibrary.wiley.com/doi/abs/10.1029/GL014i011p01150.

[22] L. Easy, F. Militello, J. Omotani, B. Dudson, E. Havlíčková, P. Tamain, V. Naulin, and A. H. Nielsen. Three dimensional simulations of plasma filaments in the scrape off layer: A comparison with models of reduced dimensionality. *Physics of Plasmas*, 21(12):122515, 2014. doi: http://dx.doi.org/10.1063/1.4904207. URL http://scitation.aip.org/content/aip/journal/pop/21/12/10.1063/1.4904207.

[23] F.D. Halpern, P. Ricci, S. Jolliet, J. Loizu, J. Morales, A. Mosetto, F. Musil, F. Riva, T.M. Tran, and C. Wersal. The GBS code for tokamak scrape-off layer simulations. *Journal of Computational Physics*,

315:388 – 408, 2016. ISSN 0021-9991. doi: https://doi.org/10.1016/j.jcp.2016.03.040. URL http://www.sciencedirect.com/science/article/pii/S0021999116001923.

[24] NJ Peacock, DC Robinson, MJ Forrest, PD Wilcock, and VV Sannikov. Measurement of the electron temperature by thomson scattering in tokamak t3. *Nature*, 224(5218):488–490, 1969.

[25] James Robert Harrison. *Characterisation of detached plasmas on the MAST tokamak*. PhD thesis, University of York, 2010.

[26] Nicholas Ross Walkden. *Properties of Intermittent Transport in the Mega Ampére Spherical Tokamak*. PhD thesis, University of York, 2014.

[27] S. Li, H. Jiang, Z. Ren, and C. Xu. Optimal tracking for a divergent-type parabolic pde system in current profile control. *Abstract and Applied Analysis*, page 940965, 2014. doi: 10.1155/2014/940965.

[28] M Keilhacker, K Lackner, K Behringer, H Murmann, and H Niedermeyer. Plasma boundary layer in limiter and divertor tokamaks. *Physica Scripta*, 1982(T2B):443, 1982. URL http://stacks.iop.org/1402-4896/1982/i=T2B/a=022.

[29] H. Meyer, T. Eich, M. Beurskens, S. Coda, A. Hakola, P. Martin, J. Adamek, M. Agostini, et al. Overview of progress in european medium sized tokamaks towards an integrated plasma-edge/wall solution. *Nuclear Fusion*, 57(10):102014, jun 2017. doi: 10.1088/1741-4326/aa6084. URL https://doi.org/10.1088%2F1741-4326%2Faa6084.

[30] Joachim Roth, E. Tsitrone, A. Loarte, Th. Loarer, G. Counsell, R. Neu, V. Philipps, S. Brezinsek, et al. Recent analysis of key plasma wall interactions issues for ITER. *Journal of Nuclear Materials*, 390–391:1 – 9, 2009. ISSN 0022-3115. doi: http://dx.doi.org/10.1016/j.jnucmat.2009.01.037. URL http://www.sciencedirect.com/science/article/pii/S0022311509000506.

[31] J. A. Boedo, D. Rudakov, R. Moyer, S. Krasheninnikov, D. Whyte, G. McKee, G. Tynan, M. Schaffer, et al. *Physics of Plasmas*, 8(11):4826–4833, 2001. doi: 10.1063/1.1406940.

[32] DA D'Ippolito, JR Myra, and SJ Zweben. Convective transport by intermittent blob-filaments: Comparison of theory and experiment. *Physics of Plasmas (1994-present)*, 18(6):060501, 2011.

[33] *SOLPS 5.0*.

[34] N. Vianello, C. Tsui, C. Theiler, S. Allan, J. Boedo, B. Labit, H. Reimerdes, K. Verhaegh, et al. Modification of sol profiles and fluctuations with line-average density and divertor flux expansion in tcv. *Nuclear Fusion*, 57(11):116014, 2017. URL http://stacks.iop.org/0029-5515/57/i=11/a=116014.

[35] D.L. Rudakov, J.A. Boedo, R.A. Moyer, P.C. Stangeby, J.G. Watkins, D.G. Whyte, L. Zeng, N.H. Brooks, et al. Far sol transport and main wall plasma interaction in diii-d. *Nuclear Fusion*, 45(12):1589, 2005. URL http://stacks.iop.org/0029-5515/45/i=12/a=014.

[36] F. Militello and J.T. Omotani. Scrape off layer profiles interpreted with filament dynamics. *Nuclear Fusion*, 56(10):104004, 2016. URL http://stacks.iop.org/0029-5515/56/i=10/a=104004.

[37] F Militello and J T Omotani. On the relation between non-exponential scrape off layer profiles and the dynamics of filaments. *Plasma Physics and Controlled Fusion*, 58(12):125004, 2016. URL http://stacks.iop.org/0741-3335/58/i=12/a=125004.

[38] ASDEX Team. The h-mode of asdex. *Nuclear Fusion*, 29(11):1959, 1989. URL http://stacks.iop.org/0029-5515/29/i=11/a=010.

[39] F. Wagner, G. Becker, K. Behringer, D. Campbell, A. Eberhagen, W. Engelhardt, G. Fussmann, O. Gehre, et al. Regime of improved confinement and high beta in neutral-beam-heated divertor discharges of the asdex tokamak. *Phys. Rev. Lett.*, 49:1408–1412, Nov 1982. doi: 10.1103/PhysRevLett.49.1408. URL https://link.aps.org/doi/10.1103/PhysRevLett.49.1408.

[40] J W Connor and H R Wilson. A review of theories of the l-h transition. *Plasma Physics and Controlled Fusion*, 42(1):R1, 2000. URL http://stacks.iop.org/0741-3335/42/i=1/a=201.

[41] B. Lipschultz, X. Bonnin, G. Counsell, A. Kallenbach, A. Kukushkin, K. Krieger, A. Leonard, A. Loarte, et al. Plasma–surface interaction, scrape-off layer and divertor physics: implications for ITER. *Nuclear Fusion*, 47(9):1189–1205, aug 2007. doi: 10.1088/0029-5515/47/

9/016. URL https://doi.org/10.1088%2F0029-5515%2F47%2F9%2F016.

[42] C S Pitcher and P C Stangeby. Experimental divertor physics. *Plasma Physics and Controlled Fusion*, 39(6):779, 1997. URL http://stacks.iop.org/0741-3335/39/i=6/a=001.

[43] K. Borrass. Disruptive tokamak density limit as scrape-off layer/divertor phenomenon. *Nuclear Fusion*, 31(6):1035, 1991. URL http://stacks.iop.org/0029-5515/31/i=6/a=003.

[44] Peter C Stangeby et al. *The plasma boundary of magnetic fusion devices*, volume 224. Institute of Physics Publishing Bristol, 2000.

[45] D. A. D'Ippolito, J. R. Myra, and S. I. Krasheninnikov. Cross-field blob transport in tokamak scrape-off-layer plasmas. *Physics of Plasmas*, 9(1):222–233, 2002. doi: http://dx.doi.org/10.1063/1.1426394. URL http://scitation.aip.org/content/aip/journal/pop/9/1/10.1063/1.1426394.

[46] B. LaBombard, R. L. Boivin, M. Greenwald, J. Hughes, B. Lipschultz, D. Mossessian, C. S. Pitcher, J. L. Terry, S. J. Zweben, and Alcator Group. Particle transport in the scrape-off layer and its relationship to discharge density limit in alcator c-mod. *Physics of Plasmas*, 8(5):2107–2117, 2001. doi: 10.1063/1.1352596. URL https://doi.org/10.1063/1.1352596.

[47] T H Stix. Heating of toroidal plasmas by neutral injection. *Plasma Physics*, 14(4):367, 1972. URL http://stacks.iop.org/0032-1028/14/i=4/a=002.

[48] DP Coster, X Bonnin, and B Braams. Further developments of the edge transport simulation package, SOLPS. Technical report, ASDEX Upgrade Team, 2003.

[49] AV Chankin, DP Coster, R Dux, Ch Fuchs, G Haas, A Herrmann, LD Horton, A Kallenbach, et al. SOLPS modelling of ASDEX upgrade H-mode plasma. *Plasma physics and controlled fusion*, 48(6):839, 2006.

[50] S. Wiesen, D. Reiter, V. Kotov, M. Baelmans, W. Dekeyser, A.S. Kukushkin, S.W. Lisgo, R.A. Pitts, et al. The new solps-iter code package. *Journal of Nuclear Materials*, 463:480 – 484, 2015. ISSN 0022-3115. doi: https://doi.org/10.1016/j.jnucmat.2014.10.

012. URL http://www.sciencedirect.com/science/article/pii/S0022311514006965. PLASMA-SURFACE INTERACTIONS 21.

[51] Gary D. Porter, S. L. Allen, M. Brown, M. E. Fenstermacher, D. N. Hill, R. A. Jong, A. W. Leonard, D. Nilson, et al. Simulation of experimentally achieved diii-d detached plasmas using the uedge code. *Physics of Plasmas*, 3(5):1967–1975, 1996. doi: 10.1063/1.871993. URL https://doi.org/10.1063/1.871993.

[52] T. Lunt, Y. Feng, M. Bernert, A. Herrmann, P. de Marné, R. McDermott, H.W. Müller, S. Potzel, et al. First emc3-eirene simulations of the impact of the edge magnetic perturbations at asdex upgrade compared with the experiment. *Nuclear Fusion*, 52(5):054013, 2012. URL http://stacks.iop.org/0029-5515/52/i=5/a=054013.

[53] Y. Feng, H. Frerichs, M. Kobayashi, A. Bader, F. Effenberg, D. Harting, H. Hoelbe, J. Huang, et al. Recent improvements in the emc3-eirene code. *Contributions to Plasma Physics*, 54(4-6):426–431, 2014. ISSN 1521-3986. doi: 10.1002/ctpp.201410092. URL http://dx.doi.org/10.1002/ctpp.201410092.

[54] A Kallenbach, M Bernert, R Dux, L Casali, T Eich, L Giannone, A Herrmann, R McDermott, et al. Impurity seeding for tokamak power exhaust: from present devices via iter to demo. *Plasma Physics and Controlled Fusion*, 55(12):124041, 2013. URL http://stacks.iop.org/0741-3335/55/i=12/a=124041.

[55] F. Wising, D. A. Knoll, S. I. Krasheninnikov, T. D. Rognlien, and D. J. Sigmar. Simulation of detachment in iter-geometry using the uedge code and a fluid neutral model. *Contributions to Plasma Physics*, 36(2?3):309–313. doi: 10.1002/ctpp.2150360238. URL https://onlinelibrary.wiley.com/doi/abs/10.1002/ctpp.2150360238.

[56] X. Litaudon, S. Abduallev, M. Abhangi, P. Abreu, M. Afzal, K.M. Aggarwal, T. Ahlgren, J.H. Ahn, et al. Overview of the JET results in support to ITER. *Nuclear Fusion*, 57(10):102001, 2017. URL http://stacks.iop.org/0029-5515/57/i=10/a=102001.

[57] D Moulton, B Lipschultz, and J Harrison. Detachment onset in mast-u according to solps-iter. In *Proceedings of the 44th EPS Conference on Plasma Physics*, volume 41F. European Physical Society, June 2017. ISBN: 979-10-96389-07.

[58] Jarrod Leddy, Hannah Victoria Willett, and Benjamin Daniel Dudson. Simulation of the interaction between plasma turbulence and neutrals in linear devices. *Nuclear Materials and Energy*, October 2016. URL http://eprints.whiterose.ac.uk/106046/.

[59] N Bisai and PK Kaw. Role of neutral gas in scrape-off layer of tokamak plasma in the presence of finite electron temperature and its gradient. *Physics of Plasmas (1994-present)*, 23(9):092509, 2016.

[60] C Wersal and P Ricci. A first-principles self-consistent model of plasma turbulence and kinetic neutral dynamics in the tokamak scrape-off layer. *Nuclear Fusion*, 55(12):123014, 2015.

[61] B. D. Dudson, M. V. Umansky, X. Q. Xu, P. B. Snyder, and H. R. Wilson. BOUT++: A framework for parallel plasma fluid simulations. *Computer Physics Communications*, 180(9):1467 – 1480, 2009. ISSN 0010-4655. doi: http://dx.doi.org/10.1016/j.cpc.2009.03.008. URL http://www.sciencedirect.com/science/article/pii/S0010465509001040.

[62] Alexander S Thrysøe, Laust E H Tophøj, Volker Naulin, Jens Juul Rasmussen, Jens Madsen, and Anders H Nielsen. The influence of blobs on neutral particles in the scrape-off layer. *Plasma Physics and Controlled Fusion*, 58(4):044010, 2016. URL http://stacks.iop.org/0741-3335/58/i=4/a=044010.

[63] S. Potzel, M. Wischmeier, M. Bernert, R. Dux, H.W. Müller, A. Scarabosio, and the ASDEX Upgrade Team. A new experimental classification of divertor detachment in asdex upgrade. *Nuclear Fusion*, 54(1):013001, 2014. URL http://stacks.iop.org/0029-5515/54/i=1/a=013001.

[64] A.S. Kukushkin, H.D. Pacher, and R.A. Pitts. Characteristics of divertor detachment for iter conditions. *Journal of Nuclear Materials*, 463:586 – 590, 2015. ISSN 0022-3115. doi: https://doi.org/10.1016/j.jnucmat.2014.10.042. URL http://www.sciencedirect.com/science/article/pii/S0022311514007260. PLASMA-SURFACE INTERACTIONS 21.

[65] C. Guillemaut, R.A. Pitts, J. Bucalossi, G. Corrigan, A.S. Kukushkin, D. Harting, A. Huber, M. Wischmeier, et al. Edge2d-eirene modelling of divertor detachment in jet high triangularity l-mode plasmas in carbon and be/w environment. *Journal of Nuclear Materials*, 438:S638 – S642, 2013. ISSN 0022-3115. doi: https://doi.org/

10.1016/j.jnucmat.2013.01.134. URL http://www.sciencedirect.com/science/article/pii/S0022311513001426. Proceedings of the 20th International Conference on Plasma-Surface Interactions in Controlled Fusion Devices.

[66] I.T. Chapman, J. Adamek, R.J. Akers, S. Allan, L. Appel, O. Asunta, M. Barnes, N. Ben Ayed, et al. Overview of mast results. *Nuclear Fusion*, 55(10):104008, 2015. URL http://stacks.iop.org/0029-5515/55/i=10/a=104008.

[67] A. Kirk, J. Adamek, R.J. Akers, S. Allan, L. Appel, F. Arese Lucini, M. Barnes, T. Barrett, et al. Overview of recent physics results from mast. *Nuclear Fusion*, 57(10):102007, 2017. URL http://stacks.iop.org/0029-5515/57/i=10/a=102007.

[68] A Sykes, R Akers, L Appel, P G Carolan, N J Conway, M Cox, A R Field, D A Gates, et al. High-β performance of the start spherical tokamak. *Plasma Physics and Controlled Fusion*, 39(12B):B247, 1997. URL http://stacks.iop.org/0741-3335/39/i=12B/a=019.

[69] M. Gryaznevich, R. Akers, P. G. Carolan, N. J. Conway, D. Gates, A. R. Field, T. C. Hender, I. Jenkins, et al. Achievement of record β in the start spherical tokamak. *Phys. Rev. Lett.*, 80:3972–3975, May 1998. doi: 10.1103/PhysRevLett.80.3972. URL https://link.aps.org/doi/10.1103/PhysRevLett.80.3972.

[70] G.F. Counsell, J.-W. Ahn, R. Akers, E. Arends, S.J. Fielding, P. Helander, A. Kirk, H. Meyer, et al. A review of plasma boundary phenomena in the mega ampere spherical tokamak. *Journal of Nuclear Materials*, 313-316:804 – 812, 2003. ISSN 0022-3115. doi: https://doi.org/10.1016/S0022-3115(02)01439-3. URL http://www.sciencedirect.com/science/article/pii/S0022311502014393. Plasma-Surface Interactions in Controlled Fusion Devices 15.

[71] F Militello, P Tamain, W Fundamenski, A Kirk, V Naulin, A H Nielsen, and the MAST team. Experimental and numerical characterization of the turbulence in the scrape-off layer of mast. *Plasma Physics and Controlled Fusion*, 55(2):025005, 2013. URL http://stacks.iop.org/0741-3335/55/i=2/a=025005.

[72] A Kirk, N Ben Ayed, G Counsell, B Dudson, T Eich, A Herrmann, B Koch, R Martin, et al. Filament structures at the plasma edge on

MAST. *Plasma Physics and Controlled Fusion*, 48(12B):B433, 2006. URL http://stacks.iop.org/0741-3335/48/i=12B/a=S41.

[73] N.R. Walkden, F. Militello, J. Harrison, T. Farley, S. Silburn, and J. Young. Identification of intermittent transport in the scrape-off layer of mast through high speed imaging. *Nuclear Materials and Energy*, 12(Supplement C):175 – 180, 2017. ISSN 2352-1791. doi: https://doi.org/10.1016/j.nme.2016.10.024. URL http://www.sciencedirect.com/science/article/pii/S2352179116300667. Proceedings of the 22nd International Conference on Plasma Surface Interactions 2016, 22nd PSI.

[74] N.R. Walkden, J. Harrison, S.A. Silburn, T. Farley, S.S. Henderson, A. Kirk, F. Militello, A. Thornton, and The MAST Team. Quiescence near the x-point of mast measured by high speed visible imaging. *Nuclear Fusion*, 57(12):126028, 2017. URL http://stacks.iop.org/0029-5515/57/i=12/a=126028.

[75] H. Meyer, M.F.M. De Bock, N.J. Conway, S.J. Freethy, K. Gibson, J. Hiratsuka, A. Kirk, C.A. Michael, et al. L–h transition and pedestal studies on mast. *Nuclear Fusion*, 51(11):113011, 2011. URL http://stacks.iop.org/0029-5515/51/i=11/a=113011.

[76] G. Fishpool, J. Canik, G. Cunningham, J. Harrison, I. Katramados, A. Kirk, M. Kovari, H. Meyer, and R. Scannell. Mast-upgrade divertor facility and assessing performance of long-legged divertors. *Journal of Nuclear Materials*, 438:S356 – S359, 2013. ISSN 0022-3115. doi: https://doi.org/10.1016/j.jnucmat.2013.01.067. URL http://www.sciencedirect.com/science/article/pii/S0022311513000755. Proceedings of the 20th International Conference on Plasma-Surface Interactions in Controlled Fusion Devices.

[77] J. A. Boedo, D. L. Rudakov, R. A. Moyer, G. R. McKee, R. J. Colchin, M. J. Schaffer, P. G. Stangeby, W. P. West, et al. Transport by intermittency in the boundary of the diii-d tokamak. *Physics of Plasmas*, 10(5):1670–1677, 2003. doi: 10.1063/1.1563259. URL https://doi.org/10.1063/1.1563259.

[78] P. Zou, C. Fang, P. F. Chen, K. Yang, and Wenda Cao. Magnetic separatrix as the source region of the plasma supply for an active-region filament. *The Astrophysical Journal*, 836(1):122, 2017. URL http://stacks.iop.org/0004-637X/836/i=1/a=122.

[79] O. E. Garcia, R. Kube, A. Theodorsen, B. LaBombard, and J. L. Terry. Intermittent fluctuations in the alcator c-mod scrape-off layer for ohmic and high confinement mode plasmas. *Physics of Plasmas*, 25(5):056103, 2018. doi: 10.1063/1.5018709. URL https://doi.org/10.1063/1.5018709.

[80] C. Silva, B. Gonçalves, C. Hidalgo, M.A. Pedrosa, W. Fundamenski, M. Stamp, and R.A. Pitts. Intermittent transport in the jet far-sol. *Journal of Nuclear Materials*, 390-391:355 – 358, 2009. ISSN 0022-3115. doi: https://doi.org/10.1016/j.jnucmat.2009.01.068. URL http://www.sciencedirect.com/science/article/pii/S0022311509001317. Proceedings of the 18th International Conference on Plasma-Surface Interactions in Controlled Fusion Device.

[81] J Neuhauser, D Coster, H U Fahrbach, J C Fuchs, G Haas, A Herrmann, L Horton, M Jakobi, et al. Transport into and across the scrape-off layer in the ASDEX upgrade divertor tokamak. *Plasma Physics and Controlled Fusion*, 44(6):855–869, may 2002. doi: 10.1088/0741-3335/44/6/316. URL https://doi.org/10.1088%2F0741-3335%2F44%2F6%2F316.

[82] D. Carralero, S. Artene, M. Bernert, G. Birkenmeier, M. Faitsch, P. Manz, P. de Marne, U. Stroth, et al. On the role of filaments in perpendicular heat transport at the scrape-off layer. *Nuclear Fusion*, 58(9):096015, jul 2018. doi: 10.1088/1741-4326/aacb04. URL https://doi.org/10.1088%2F1741-4326%2Faacb04.

[83] A. Herrmann, A. Kirk, A. Schmid, B. Koch, M. Laux, M. Maraschek, H.W. Mueller, J. Neuhauser, et al. The filamentary structure of elms in the scrape-off layer in asdex upgrade. *Journal of Nuclear Materials*, 363-365:528 – 533, 2007. ISSN 0022-3115. doi: https://doi.org/10.1016/j.jnucmat.2006.12.041. URL http://www.sciencedirect.com/science/article/pii/S0022311506006507. Plasma-Surface Interactions-17.

[84] O E Garcia, J Horacek, R A Pitts, A H Nielsen, W Fundamenski, J P Graves, V Naulin, and J Juul Rasmussen. Interchange turbulence in the TCV scrape-off layer. *Plasma Physics and Controlled Fusion*, 48 (1):L1–L10, dec 2005. doi: 10.1088/0741-3335/48/1/l01. URL https://doi.org/10.1088%2F0741-3335%2F48%2F1%2Fl01.

[85] O.E Garcia, J Horacek, R.A Pitts, A.H Nielsen, W Fundamenski, V Naulin, and J. Juul Rasmussen. Fluctuations and transport in

the TCV scrape-off layer. *Nuclear Fusion*, 47(7):667–676, jun 2007. doi: 10.1088/0029-5515/47/7/017. URL https://doi.org/10.1088%2F0029-5515%2F47%2F7%2F017.

[86] A Theodorsen, O E Garcia, J Horacek, R Kube, and R A Pitts. Scrape-off layer turbulence in TCV: evidence in support of stochastic modelling. *Plasma Physics and Controlled Fusion*, 58(4):044006, jan 2016. doi: 10.1088/0741-3335/58/4/044006. URL https://doi.org/10.1088%2F0741-3335%2F58%2F4%2F044006.

[87] D L Rudakov, J A Boedo, R A Moyer, S Krasheninnikov, A W Leonard, M A Mahdavi, G R McKee, G D Porter, et al. Fluctuation-driven transport in the diii-d boundary. *Plasma Physics and Controlled Fusion*, 44(6):717, 2002. URL http://stacks.iop.org/0741-3335/44/i=6/a=308.

[88] S.J. Zweben, R.J. Maqueda, D.P. Stotler, A. Keesee, J. Boedo, C.E. Bush, S.M. Kaye, B. LeBlanc, et al. High-speed imaging of edge turbulence in nstx. *Nuclear Fusion*, 44(1):134, 2004. URL http://stacks.iop.org/0029-5515/44/i=1/a=016.

[89] J. R. Myra, D. A. D'Ippolito, D. P. Stotler, S. J. Zweben, B. P. LeBlanc, J. E. Menard, R. J. Maqueda, and J. Boedo. Blob birth and transport in the tokamak edge plasma: Analysis of imaging data. *Physics of Plasmas*, 13(9):092509, 2006. doi: http://dx.doi.org/10.1063/1.2355668. URL http://scitation.aip.org/content/aip/journal/pop/13/9/10.1063/1.2355668.

[90] T Klinger, A Alonso, S Bozhenkov, R Burhenn, A Dinklage, G Fuchert, J Geiger, O Grulke, et al. Performance and properties of the first plasmas of wendelstein 7-x. *Plasma Physics and Controlled Fusion*, 59(1):014018, 2017. URL http://stacks.iop.org/0741-3335/59/i=1/a=014018.

[91] J M Dewhurst, B Hnat, N Ohno, R O Dendy, S Masuzaki, T Morisaki, and A Komori. Statistical properties of edge plasma turbulence in the large helical device. *Plasma Physics and Controlled Fusion*, 50 (9):095013, aug 2008. doi: 10.1088/0741-3335/50/9/095013. URL https://doi.org/10.1088%2F0741-3335%2F50%2F9%2F095013.

[92] C. Theiler, I. Furno, P. Ricci, A. Fasoli, B. Labit, S. H. Müller, and G. Plyushchev. Cross-field motion of plasma blobs in an open magnetic field line configuration. *Phys. Rev. Lett.*, 103:065001, Aug 2009.

doi: 10.1103/PhysRevLett.103.065001. URL http://link.aps.org/doi/10.1103/PhysRevLett.103.065001.

[93] R Kube, A Theodorsen, O E Garcia, B LaBombard, and J L Terry. Fluctuation statistics in the scrape-off layer of alcator c-mod. *Plasma Physics and Controlled Fusion*, 58(5):054001, mar 2016. doi: 10.1088/0741-3335/58/5/054001. URL https://doi.org/10.1088%2F0741-3335%2F58%2F5%2F054001.

[94] A. V. Filippas, Roger D. Bengston, G.ž2010X. Li, Mark Meier, Ch. P. Ritz, and E. J. Powers. Conditional analysis of floating potential fluctuations at the edge of the texas experimental tokamak upgrade (textž2010u). *Physics of Plasmas*, 2(3):839–845, 1995. doi: 10.1063/1.871435. URL https://doi.org/10.1063/1.871435.

[95] David Schwörer. Einfluss der magnetfeldverscherung auf die dynamik turbulenter strukturen. Bachelor thesis, Universität Stuttgart, 2012.

[96] F Militello, N R Walkden, T Farley, W A Gracias, J Olsen, F Riva, L Easy, N Fedorczak, et al. Multi-code analysis of scrape-off layer filament dynamics in mast. *Plasma Physics and Controlled Fusion*, 58(10):105002, 2016. URL http://stacks.iop.org/0741-3335/58/i=10/a=105002.

[97] J.L. Terry, S.J. Zweben, M.V. Umansky, I. Cziegler, O. Grulke, B. LaBombard, and D.P. Stotler. Spatial structure of scrape-off-layer filaments near the midplane and x-point regions of alcator-c-mod. *Journal of Nuclear Materials*, 390-391:339 – 342, 2009. ISSN 0022-3115. doi: https://doi.org/10.1016/j.jnucmat.2009.01.152. URL http://www.sciencedirect.com/science/article/pii/S0022311509001275. Proceedings of the 18th International Conference on Plasma-Surface Interactions in Controlled Fusion Device.

[98] S. J. Zweben, D. P. Stotler, J. L. Terry, B. LaBombard, M. Greenwald, M. Muterspaugh, C. S. Pitcher, Alcator C-Mod Group, et al. Edge turbulence imaging in the alcator c-mod tokamak. *Physics of Plasmas*, 9(5):1981–1989, 2002. doi: 10.1063/1.1445179. URL https://doi.org/10.1063/1.1445179.

[99] S J Zweben, J R Myra, W M Davis, D A D'Ippolito, T K Gray, S M Kaye, B P LeBlanc, R J Maqueda, D A Russell, and D P Stotler and. Blob structure and motion in the edge and SOL of NSTX. *Plasma Physics and Controlled Fusion*, 58(4):044007, jan 2016. doi:

10.1088/0741-3335/58/4/044007. URL https://doi.org/10.1088/0741-3335/58/4/044007.

[100] G Fuchert, G Birkenmeier, D Carralero, T Lunt, P Manz, H W Müller, B Nold, M Ramisch, V Rohde, and U Stroth. Blob properties in l- and h-mode from gas-puff imaging in ASDEX upgrade. *Plasma Physics and Controlled Fusion*, 56(12):125001, oct 2014. doi: 10.1088/0741-3335/56/12/125001. URL https://doi.org/10.1088%2F0741-3335%2F56%2F12%2F125001.

[101] Y. Sechrest, D. Smith, D. P. Stotler, T. Munsat, and S. J. Zweben. Comparison of beam emission spectroscopy and gas puff imaging edge fluctuation measurements in national spherical torus experiment. *Physics of Plasmas*, 22(5):052310, 2015. doi: 10.1063/1.4921215.

[102] B. A. Carreras, V. E. Lynch, and B. LaBombard. Structure and properties of the electrostatic fluctuations in the far scrape-off layer region of alcator c-mod. *Physics of Plasmas*, 8(8):3702–3707, 2001. doi: 10.1063/1.1387266. URL https://doi.org/10.1063/1.1387266.

[103] D. Carralero, M. Siccinio, M. Komm, S.A. Artene, F.A. D'Isa, J. Adamek, L. Aho-Mantila, G. Birkenmeier, et al. Recent progress towards a quantitative description of filamentary SOL transport. *Nuclear Fusion*, 57(5):056044, apr 2017. doi: 10.1088/1741-4326/aa64b3. URL https://doi.org/10.1088%2F1741-4326%2Faa64b3.

[104] G.S. Xu, V. Naulin, W. Fundamenski, C. Hidalgo, J.A. Alonso, C. Silva, B. Gonçalves, A.H. Nielsen, et al. Blob/hole formation and zonal-flow generation in the edge plasma of the jet tokamak. *Nuclear Fusion*, 49(9):092002, 2009. URL http://stacks.iop.org/0029-5515/49/i=9/a=092002.

[105] A Kirk, A J Thornton, J R Harrison, F Militello, and N R Walkden and. L-mode filament characteristics on MAST as a function of plasma current measured using visible imaging. *Plasma Physics and Controlled Fusion*, 58(8):085008, jul 2016. doi: 10.1088/0741-3335/58/8/085008. URL https://doi.org/10.1088%2F0741-3335%2F58%2F8%2F085008.

[106] Noam Katz, Jan Egedal, Will Fox, Ari Le, and Miklos Porkolab. Experiments on the propagation of plasma filaments. *Phys. Rev. Lett.*, 101:015003, Jul 2008. doi: 10.1103/PhysRevLett.101.015003. URL https://link.aps.org/doi/10.1103/PhysRevLett.101.015003.

[107] F Militello, T Farley, K Mukhi, N Walkden, and JT Omotani. A two-dimensional statistical framework connecting thermodynamic profiles with filaments in the scrape off layer and application to experiments. *Physics of Plasmas*, 25(5):056112, 2018.

[108] N R Walkden, A Wynn, F Militello, B Lipschultz, G Matthews, C Guillemaut, J Harrison, and D Moulton and. Interpretation of scrape-off layer profile evolution and first-wall ion flux statistics on JET using a stochastic framework based on fillamentary motion. *Plasma Physics and Controlled Fusion*, 59(8):085009, jun 2017. doi: 10.1088/1361-6587/aa7365. URL https://doi.org/10.1088%2F1361-6587%2Faa7365.

[109] N. Fedorczak, M. Peret, H. Bufferand, G. Ciraolo, Ph. Ghendrih, and P. Tamain. A spectral filament model for turbulent transport and scrape off layer width in circular geometry. *Nuclear Materials and Energy*, 19:433 – 439, 2019. ISSN 2352-1791. doi: https://doi.org/10.1016/j.nme.2019.03.025. URL http://www.sciencedirect.com/science/article/pii/S2352179118301339.

[110] Paola Paruta, C. Beadle, P. Ricci, and C. Theiler. Blob velocity scaling in diverted tokamaks: A comparison between theory and simulation. *Physics of Plasmas*, 26(3):032302, 2019. doi: 10.1063/1.5080675. URL https://doi.org/10.1063/1.5080675.

[111] J T Omotani, F Militello, L Easy, and N R Walkden. The effects of shape and amplitude on the velocity of scrape-off layer filaments. *Plasma Physics and Controlled Fusion*, 58(1):014030, nov 2015. doi: 10.1088/0741-3335/58/1/014030. URL https://doi.org/10.1088%2F0741-3335%2F58%2F1%2F014030.

[112] N. Vianello, C. Tsui, C. Theiler, S. Allan, J. Boedo, B. Labit, H. Reimerdes, K. Verhaegh, et al. Modification of SOL profiles and fluctuations with line-average density and divertor flux expansion in TCV. *Nuclear Fusion*, 57(11):116014, aug 2017. doi: 10.1088/1741-4326/aa7db3. URL https://doi.org/10.1088%2F1741-4326%2Faa7db3.

[113] N R Walkden, L Easy, F Militello, and J T Omotani. Dynamics of 3d isolated thermal filaments. *Plasma Physics and Controlled Fusion*, 58(11):115010, 2016. URL http://stacks.iop.org/0741-3335/58/i=11/a=115010.

[114] A. Dempsey, H. Leggate, B. D. Dudson, D. Schwörer, and M. M. Turner. Finite larmor radius effects on filament dynamics. *Plasma Physics and Controlled Fusion*, in prep.

[115] R. Kube and O. E. Garcia. Velocity scaling for filament motion in scrape-off layer plasmas. *Physics of Plasmas*, 18(10):102314, 2011. doi: 10.1063/1.3647553. URL https://doi.org/10.1063/1.3647553.

[116] J T Omotani, F Militello, L Easy, and N R Walkden. The effects of shape and amplitude on the velocity of scrape-off layer filaments. *Plasma Physics and Controlled Fusion*, 58(1):014030, 2016. URL http://stacks.iop.org/0741-3335/58/i=1/a=014030.

[117] Justin R. Angus and Maxim V. Umansky. Modeling of large amplitude plasma blobs in three-dimensions. *Physics of Plasmas*, 21(1): 012514, 2014. doi: 10.1063/1.4863503.

[118] Justin R. Angus, Maxim V. Umansky, and Sergei I. Krasheninnikov. Effect of drift waves on plasma blob dynamics. *Phys. Rev. Lett.*, 108:215002, May 2012. doi: 10.1103/PhysRevLett.108.215002. URL http://link.aps.org/doi/10.1103/PhysRevLett.108.215002.

[119] OE Garcia, NH Bian, and W Fundamenski. Radial interchange motions of plasma filaments. *Physics of Plasmas (1994-present)*, 13(8): 082309, 2006.

[120] G. Q. Yu and S. I. Krasheninnikov. Dynamics of blobs in scrape-off-layer/shadow regions of tokamaks and linear devices. *Physics of Plasmas*, 10(11):4413–4418, 2003. doi: http://dx.doi.org/10.1063/1.1616937. URL http://scitation.aip.org/content/aip/journal/pop/10/11/10.1063/1.1616937.

[121] Luke Easy, Fulvio Militello, John Omotani, NR Walkden, and Benjamin Dudson. Investigation of the effect of resistivity on scrape off layer filaments using three-dimensional simulations. *Physics of Plasmas (1994-present)*, 23(1):012512, 2016.

[122] R. Kube and O. E. Garcia. Effect of dynamical friction on interchange motion of plasma filaments. *Physics of Plasmas*, 19(4):042305, 2012. doi: 10.1063/1.4704793. URL https://doi.org/10.1063/1.4704793.

[123] F Militello, B Dudson, L Easy, A Kirk, and P Naylor. On the interaction of scrape off layer filaments. *Plasma Physics and Controlled Fusion*, 59(12):125013, nov 2017. doi: 10.1088/1361-6587/aa9252. URL https://doi.org/10.1088%2F1361-6587%2Faa9252.

[124] Fabio Riva, Clothilde Colin, Julien Denis, Luke Easy, Ivo Furno, Jens Madsen, Fulvio Militello, Volker Naulin, et al. Blob dynamics in the torpex experiment: a multi-code validation. *Plasma Physics and Controlled Fusion*, 58(4):044005, 2016.

[125] D. Schwörer, N.R. Walkden, H. Leggate, B.D. Dudson, F. Militello, T. Downes, and M.M. Turner. Influence of plasma background including neutrals on scrape-off layer filaments using 3D simulations. *Nuclear Materials and Energy*, 12:825 – 830, 2017. ISSN 2352-1791. doi: 10.1016/j.nme.2017.02.016. URL http://www.sciencedirect.com/science/article/pii/S2352179116301648.

[126] D. Schwörer, N.R. Walkden, H. Leggate, B.D. Dudson, F. Militello, T. Downes, and M.M. Turner. Influence of plasma background on 3D scrape-off layer filaments. *Plasma Physics and Controlled Fusion*, 61(2):025008, December 2018. doi: 10.1088/1361-6587/aae8fe. URL https://doi.org/10.1088/1361-6587/aae8fe.

[127] P Hill, B Dudson, J T Parker, and D Schwörer. URL https://boutproject.github.io/. Accessed 11 Jan 2018.

[128] X. Q. Xu and R. H. Cohen. Scrape-off layer turbulence theory and simulations. *Contributions to Plasma Physics*, 38(1-2):158–170, 1998. ISSN 1521-3986. doi: 10.1002/ctpp.2150380124. URL http://dx.doi.org/10.1002/ctpp.2150380124.

[129] T.D. Rognlien, J.L. Milovich, M.E. Rensink, and G.D. Porter. A fully implicit, time dependent 2-d fluid code for modeling tokamak edge plasmas. *Journal of Nuclear Materials*, 196–198:347 – 351, 1992. ISSN 0022-3115. doi: http://dx.doi.org/10.1016/S0022-3115(06)80058-9. URL http://www.sciencedirect.com/science/article/pii/S0022311506800589. Plasma-Surface Interactions in Controlled Fusion DevicesProceedings of the Tenth International Conference on Plasma-Surface Interactions in Controlled Fusion Devices.

[130] B Dudson, P Hill, D Schwörer, D Dickinson, and M Loiten and. URL https://github.com/boutproject/BOUT-dev. Accessed 11 Jan 2018.

[131] Free Software Foundation, 2007. URL https://www.gnu.org/licenses/lgpl-3.0.html. Accessed 11 Jan 2018.

[132] Mark Ainsworth and Bill Senior. An adaptive refinement strategy for hp-finite element computations. *Applied Numerical Mathematics*, 26(1):165 – 178, 1998. ISSN 0168-9274. doi: https://doi.org/10.1016/S0168-9274(97)00083-4. URL http://www.sciencedirect.com/science/article/pii/S0168927497000834.

[133] Tao Pang. *An Introduction to Computational Physics*. Cambridge University Press, 2006.

[134] Andreas Meister. *Numerik linearer gleichungssysteme*, volume 3. Springer, 2008.

[135] George D Byrne and Alan C Hindmarsh. Pvode, an ode solver for parallel computers. *The International Journal of High Performance Computing Applications*, 13(4):354–365, 1999.

[136] Guang-Shan Jiang and Danping Peng. Weighted eno schemes for hamilton–jacobi equations. *SIAM Journal on Scientific computing*, 21(6):2126–2143, 2000.

[137] Luke Easy. *Three Dimensional Simulations of Scrape-Off Layer Filaments*. PhD thesis, University of York, 2016.

[138] B. D. Dudson, A. Allen, G. Breyiannis, E. Brugger, J. Buchanan, L. Easy, S. Farley, I. Joseph, et al. BOUT++: Recent and current developments. *Journal of Plasma Physics*, 81, 1 2015. ISSN 1469-7807. doi: 10.1017/S0022377814000816. URL http://journals.cambridge.org/article_S0022377814000816.

[139] S Balay, S Abhyankar, M Adams, J Brown, P Brune, K Buschelman, L Dalcin, A Dener, et al. Petsc users manual. Technical report, 2019.

[140] Alan C. Hindmarsh, Peter N. Brown, Keith E. Grant, Steven L. Lee, Radu Serban, Dan E. Shumaker, and Carol S. Woodward. Sundials: Suite of nonlinear and differential/algebraic equation solvers. *ACM Trans. Math. Softw.*, 31(3):363–396, September 2005. ISSN 0098-3500. doi: 10.1145/1089014.1089020. URL http://doi.acm.org/10.1145/1089014.1089020.

[141] Kambiz Salari and Patrick Knupp. Code verification by the method of manufactured solutions. Technical report, Sandia National Labs., Albuquerque, NM (US); Sandia National Labs ..., 2000.

[142] Andrei N. Simakov and Peter J. Catto. Drift-ordered fluid equations for field-aligned modes in low-β collisional plasma with equilibrium pressure pedestals. *Physics of Plasmas*, 10(12):4744–4757, 2003. doi: http://dx.doi.org/10.1063/1.1623492. URL http://scitation.aip.org/content/aip/journal/pop/10/12/10.1063/1.1623492.

[143] Andrei N. Simakov and Peter J. Catto. Erratum: "drift-ordered fluid equations for field-aligned modes in low-β collisional plasma with equilibrium pressure pedestals" [phys. plasmas 10, 4744 (2003)]. *Physics of Plasmas*, 11(5):2326–2326, 2004. doi: http://dx.doi.org/10.1063/1.1703527. URL http://scitation.aip.org/content/aip/journal/pop/11/5/10.1063/1.1703527.

[144] W. Fundamenski, O.E. Garcia, V. Naulin, R.A. Pitts, A.H. Nielsen, J. Juul Rasmussen, J. Horacek, J.P. Graves, and JET EFDA contributors. Dissipative processes in interchange driven scrape-off layer turbulence. *Nuclear Fusion*, 47(5):417, 2007. URL http://stacks.iop.org/0029-5515/47/i=5/a=006.

[145] B D Dudson, 2017. URL https://github.com/boutproject/SD1D/tree/master/doc. Version 1538638; Accessed Sept 2018.

[146] B D Dudson, 2017. URL https://github.com/boutproject/SD1D/blob/ea352250b3b6b5c9566098e204e45b54e987caa5/doc/sd1d-manual.tex. Version ea35225; Accessed Sept 2020.

[147] I.H. Hutchinson. Thermal front analysis of detached divertors and MARFEs. *Nuclear Fusion*, 34(10):1337, 1994. URL http://stacks.iop.org/0029-5515/34/i=10/a=I04.

[148] S. I. Krasheninnikov and A. I. Smolyakov. On neutral wind and blob motion in linear devices. *Physics of Plasmas*, 10(7):3020–3021, 2003. doi: 10.1063/1.1579692. URL https://doi.org/10.1063/1.1579692.

[149] B D Dudson, 2018. URL https://github.com/boutproject/SD1D/blob/master/sd1d.cxx#L524. Version 004381b; Accessed Sept 2020.

[150] B D Dudson, J Allen, T Body, B Chapman, C Lau, L Townley, D Moulton, J Harrison, and B Lipschultz. The role of particle, energy and momentum losses in 1d simulations of divertor detachment. *Plasma Physics and Controlled Fusion*, 61(6):065008, may 2019. doi: 10.1088/1361-6587/ab1321. URL https://doi.org/10.1088%2F1361-6587%2Fab1321.

[151] D. Schwörer, N.R. Walkden, H. Leggate, B.D. Dudson, F. Militello, T. Downes, and M.M. Turner. On the dynamics of 3D scrape-off layer filaments in detached conditions. *Nuclear Fusion*, submitted.

[152] S.I. Krasheninnikov, M. Rensink, T.D. Rognlien, A.S. Kukushkin, J.A. Goetz, B. LaBombard, B. Lipschultz, J.L. Terry, and M. Umansky. Stability of the detachment front in a tokamak divertor. *Journal of Nuclear Materials*, 266-269:251 – 257, 1999. ISSN 0022-3115. doi: https://doi.org/10.1016/S0022-3115(98)00577-7. URL http://www.sciencedirect.com/science/article/pii/S0022311598005777.

[153] JR Myra, DA D'ippolito, SI Krasheninnikov, and GQ Yu. Convective transport in the scrape-off-layer by nonthermalized spinning blobs. *Physics of Plasmas (1994-present)*, 11(9):4267–4274, 2004.

[154] A.S. Thrysøe, J. Madsen, V. Naulin, and J. Juul Rasmussen. Influence of molecular dissociation on blob-induced atom density perturbations. *Nuclear Fusion*, 58(9):096005, 2018. URL http://stacks.iop.org/0029-5515/58/i=9/a=096005.

[155] Thomas Williams, Colin Kelley, and many others. Gnuplot 5.0: an interactive plotting program. http://gnuplot.sourceforge.net/, Feb 2016.

[156] M. Wischmeier, M. Groth, A. Kallenbach, A.V. Chankin, D.P. Coster, R. Dux, A. Herrmann, H.W. Müller, et al. Current understanding of divertor detachment: Experiments and modelling. *Journal of Nuclear Materials*, 390–391(0):250 – 254, 2009. ISSN 0022-3115. doi: http://dx.doi.org/10.1016/j.jnucmat.2009.01.081. URL http://www.sciencedirect.com/science/article/pii/S002231150900107X. Proceedings of the 18th International Conference on Plasma-Surface Interactions in Controlled Fusion Device Proceedings of the 18th International Conference on Plasma-Surface Interactions in Controlled Fusion Device.

[157] Wonjae Lee, J.R. Angus, Maxim V. Umansky, and Sergei I. Krasheninnikov. Electromagnetic effects on plasma blob-filament transport. *Journal of Nuclear Materials*, 463:765 – 768, 2015. ISSN 0022-3115. doi: https://doi.org/10.1016/j.jnucmat.2014.09.083. URL http://www.sciencedirect.com/science/article/pii/S0022311514006837. PLASMA-SURFACE INTERACTIONS 21.

[158] N R Walkden, B D Dudson, and G Fishpool. Characterization of 3d filament dynamics in a MAST SOL flux tube geometry. *Plasma Physics and Controlled Fusion*, 55(10):105005, 2013. URL http://stacks.iop.org/0741-3335/55/i=10/a=105005.

[159] SF Smith, SJP Pamela, A Fil, M Hölzl, GTA Huijsmans, A Kirk, D Moulton, O Myatra, AJ Thornton, and HR Wilson. Elm burn-through predictions for mast-u super-x plasmas. In *46th European Physical Society Conference on Plasma Physics, EPS 2019*, 2019.

[160] D. Carralero, J. Madsen, S.A. Artene, M. Bernert, G. Birkenmeier, T. Eich, G. Fuchert, F. Laggner, et al. A study on the density shoulder formation in the sol of h-mode plasmas. *Nuclear Materials and Energy*, 12:1189 – 1193, 2017. ISSN 2352-1791. doi: https://doi.org/10.1016/j.nme.2016.11.016. URL http://www.sciencedirect.com/science/article/pii/S2352179116301715. Proceedings of the 22nd International Conference on Plasma Surface Interactions 2016, 22nd PSI.

[161] Ole Tange. *GNU Parallel 2018*. Ole Tange, April 2018. doi: 10.5281/zenodo.1146014. URL https://doi.org/10.5281/zenodo.1146014.

[162] S. Behnel, R. Bradshaw, C. Citro, L. Dalcin, D.S. Seljebotn, and K. Smith. Cython: The best of both worlds. *Computing in Science Engineering*, 13(2):31 –39, 2011. ISSN 1521-9615. doi: 10.1109/MCSE.2010.118.

[163] Bradley M. Kuhn et al. , 12 2019. URL https://copyleft.org. Accessed 13 Dec 2019.

[164] Free Software Foundation, 11 2016. URL https://www.gnu.org/licenses/why-not-lgpl.html. Accessed 11 Jan 2018.

[165] Free Software Foundation, 1 2018. URL https://www.gnu.org/philosophy/free-sw.html. Version 1.153; Accessed 11 Jan 2018.

[166] Free Software Foundation, 11 2016. URL https://www.gnu.org/licenses/licenses.html. Accessed 11 Jan 2018.

[167] Free Software Foundation, 11 2016. URL https://www.gnu.org/education/edu-why.html. Accessed 11 Jan 2018.

APPENDIX B

API and implementation details

The neutrals model was designed to simplify the usage in codes beyond the STORM version used here. In order to minimise the changes required in the physics model, the neutrals model is implemented as a class.

The base class provides methods for the interaction terms in the plasma model. Further, the version of the neutrals model can be switched using the input file described in section 3.1. As such the neutrals model can be chosen at run time, without any modifications of the code.

During initialisation of the physics model, a neutrals objects need to be created. The factory expects a pointer to the solver, the mesh, and either absolute name of the section from the input file where the for the neutrals are, or a pointer to that section:

```
auto neutrals = NeutralsFactory::create(solver,mesh,"neutrals");
```

Thereby the factory reads the value of the `type` field to determine the

requested model.

Besides the `diffusion` neutrals model, described in sec. 3.4.1 and the `parallel` neutral model, described in sec. 3.4.2, the `none` neutrals model is available, which can be used so switch of the neutrals in a convenient way.

The neutral model needs to know various plasma quantities. Setters are available to provide the references to the fields, such that the neutrals has access to the current values. The following functions are available, which can be used to set the respective values:

```
neutrals->setPlasmaDensity(const Field3D &n);
neutrals->setPlasmaDensityStag(const Field3D &n_stag);
neutrals->setElectronTemperature(const Field3D &Te);
neutrals->setIonTemperature(const Field3D &Ti);
neutrals->setElectronVelocity(const Field3D &U);
neutrals->setIonVelocity(const Field3D &U);
neutrals->setPotential(const Field3D &phi);
```

Further the function `neutrals->setUnit(const Unit &unit);` is available, which needs to be called to set the unit system. While internally the same of units is used as in the plasma equations, the units are needed, as the cross section is a non-linear function, thus e.g. temperatures and velocities are needed in SI base units. Initialisation is completed by calling `neutrals->init()`.

The neutrals terms have also to be added to the influenced evolving plasma equations. For example in the plasma density equation, the `neutrals->getDensitySource()` call needs to be added to the density equation:

```
ddt(n)+=neutrals->getDensitySource();
```

Similar source terms are available for the vorticity, ion and electron parallel velocity, electron temperature and energy source.

APPENDIX C

BOUT++ contributions

BOUT++ has been used for the simulations presented in this thesis. As part of the PhD, several contributions have been made to BOUT++.

C.1 BOUT++ for python

In order to allow the vorticity contibution analysis presented in section 3.5, as part of this PhD a python interface for BOUT++ was developed. This allows one to use the BOUT++ features in a python code. The benefit of such an interface has already been discussed in the past [138]. The motivation for implementing this as part of this PhD was to recompute the derivatives to analyze the contributions of time derivatives, mostly of the vorticity terms in equation (3.44) in a post processing style. Previously this would require to rerun the code, and dump the derivatives addition-

ally. Another option would have been to reimplement the used derivative schemes and bracket operators in python. While this has been done in the past, porting all the features that BOUT++ supports and that where needed, would not only lead to code duplication and thus an increased risk of bugs.

The python interface for BOUT++ is written mostly in Cython [162], which can be used as a wrapper language for C and python. Cython also support C++ to some extend. Technically a bash script generates the cython code, which allows one to generate similar code for the different derivatives or fields, while avoiding repeatition of boilerplate code.

Initially only the set of functions for computing the derivatives of the vorticity equation where implemented. By now the interface exposes most of the C++ API, for example the different Fields, Field operations, the Mesh, Options as well as most differential operators and vectors. Instead of relying only on positional arguments, the python interface often provides named arguments, allowing to write clearer code.

The `Field3D` can be created by using the `FieldFactory` of BOUT++ to create fields using arithmetic expressions. Further it can be generated using boutdata's `collect`. The `collect` function is part of BOUT++'s post processing python library that can assemble the non-parallel dump files written by BOUT++. `Field3D.fromCollect()` function returns a `Field3D` object from an arbitrary time-point in the dump file. All the options that `collect` supports can be used, as they are forwarded to `collect`. This function is mostly useful for post processing. It is also MPI aware, which allows one to do post processing calculations in parallel, however as typically only a single calculation is done, reading in the data from disk is often the slowest part of the post processing. Further it is also possible to set the

values of a `Field3D` with either another `Field3D`, a numpy-array object or from scalar values. As the `Field3D` object supports slicing, it is possible to get a 2D cross section of the 3D domain for example.

Previously most MMS tests required to start a new binary for each iteration. With the BOUT++ interface the handling for several meshes was also improved. Thus rather than relying on the global mesh, each mesh now knows its mesh, allowing to do a full parameter scan within a single instance of BOUT++. This can reduce the time required to run tests, thus making it more convenient to run many tests frequently to verify that everything works as expected and notice regressions early in the development cycle.

Further the Solver class is exposed. This allows one to implement the equations of a physics model directly in python. The performance penalty for the additional wrapper is in the few percent range, at least for the blob2d example. While the current benefits are rather small, it allows one to run BOUT++ simulations without having to compile BOUT++, as pre compiled python binaries are available for Fedora.

An example simulation of a plasma physics problem using the python interface can be found as part of BOUT++ located at 'examples/boutcore/blob2d.py'.

Further documentation on the interface is available after running `make doc`, after installing the manual on fedora with `sudo dnf install bout++-doc` or online at `https://omadesala.physics.dcu.ie/bout/user_docs/python_boutcore.html` A simplified example is shown below:

```
#!/bin/python3
import boutcore as bc

bc.init("mesh:n=48")
```

```
class Model(bc.PhysicsModel):
  def init(self,restart):
    self.dens = bc.create3D("sin(x)")
    self.solve_for(n=self.dens)

  def rhs(self,time):
    self.dens.ddt(bc.DDX(self.dens))



model = Model()
model.solve()
```

The blob2d model has been converted to python:

```
#!/bin/python3
# -*- coding: utf-8

#!######################################################################
#
#       2D blob simulations
#
#  Copyright:   NR Walkden, B Dudson, D Schwörer;  2012, 2017, 2018
#
#######################################################################

import boutcore as bc
from numpy import sqrt
from boutcore import bracket, DDZ, Delp2, PhysicsModel
import sys
```

```
bc.init("-d blob".split(" ") + sys.argv[1:])


class Blob2D(PhysicsModel):

    def init(self, restart):
        self.mesh = bc.Mesh.getGlobal()
        self.n = bc.Field3D.fromMesh(self.mesh)
        self.omega = bc.Field3D.fromMesh(self.mesh)

        self.phiSolver = bc.Laplacian()

        options = bc.Options("model")
        # Temperature in eV
        Te0 = options.get("Te0", 30)
        e = options.get("e", 1.602e-19)
        m_i = options.get("m_i", 2 * 1.667e-27)
        m_e = options.get("m_e", 9.11e-31)

        # Viscous diffusion coefficient
        self.D_vort = options.get("D_vort", 0)
        # Density diffusion coefficient
        self.D_n = options.get("D_n", 0)

        # Radius of curvature [m]
        self.R_c = options.get("R_c",   1.5)
        # Parallel connection length [m]
```

```
        self.L_par = options.get("L_par", 10)

        # Value of magnetic field strength [T]
        B0 = options.get("B0", 0.35)

        # System option switches

        # Include compressible ExB term in density equation
        self.compressible = options.get("compressible", False)
        # Use Boussinesq approximation in vorticity
        self.boussinesq = options.get("boussinesq", True)
        # Sheath closure
        self.sheath = options.get("sheath", True)

        Omega_i = e * B0 / m_i           # Cyclotron Frequency
        c_s = sqrt(e * Te0 / m_i)      # Bohm sound speed
        self.rho_s = c_s / Omega_i          # Bohm gyro-radius

        print("\n\n\t----------Parameters: ------------ \n\tOmega_i = %e /s
              "c_s = %e m/s,\n\trho_s = %e m\n" % (Omega_i, c_s, self.rho_s)

        # Calculate delta_*, blob size scaling
        print("\tdelta_* = rho_s * (dn/n) * %e "
              % (pow(self.L_par * self.L_par / (self.R_c * self.rho_s), 1. /

        # /************ Create a solver for potential ********/
```

```
        if self.boussinesq:
            # BOUT.inp section "phiBoussinesq"
            self.phiSolver = bc.Laplacian(bc.Options("phiBoussinesq"))
        else:
            # BOUT.inp section "phiSolver"
            self.phiSolver = bc.Laplacian(bc.Options("phiSolver"))

        # Starting guess for first solve (if iterative)
        self.phi = bc.create3D("0")

        # /************* Tell BOUT++ what to solve ************/

        self.solve_for(n=self.n, omega=self.omega)
        # model.save_repeat(phi=phi)
        # model.save_once(rho_s=rho_s,c_s=c_s,Omega_i=Omega_i)

    def rhs(self, time):
        # Run communications
        ######################################
        self.mesh.communicate(self.n, self.omega)

        # Invert div(n grad(phi)) = grad(n) grad(phi) + n Delp_perp^2(phi) =
        ######################################
        # Set the time derivative by adding/... to it
        # make sure to never overwrite it
        # ddt_n = bla does NOT set the time derivative
        ddt_n = self.n.ddt()
```

```
ddt_n.set(0)
if not self.boussinesq:
    # Including full density in vorticit inversion
    # Update the 'C' coefficient. See invert_laplace.hxx
    self.phiSolver.setCoefC(n)
    # Use previous solution as guess
    self.phi = self.phiSolver.solve(omega / n, self.phi)
else:
    # Background density only (1 in normalised units)
    self.phi = self.phiSolver.solve(self.omega, self.phi)

self.mesh.communicate(self.phi)

# Density Evolution
# /

# ExB term
ddt_n += -bracket(self.phi, self.n, "BRACKET_SIMPLE")
# Curvature term
ddt_n += 2 * DDZ(self.n) * (self.rho_s / self.R_c)
# Diffusion term
ddt_n += self.D_n * Delp2(self.n)

if self.compressible:
    # ExB Compression term
    ddt_n -= 2 * self.n * DDZ(self.phi) * (self.rho_s / self.R_c)
```

```
        if self.sheath:
            # Sheath closure
            ddt_n += self.n * self.phi * \
                (self.rho_s / self.L_par)  # - (n - 1)*(rho_s/L_par)

        # Vorticity evolution
        # /
        # ExB term
        ddt_omega = -bracket(self.phi, self.omega, "BRACKET_SIMPLE")
        ddt_omega += 2 * DDZ(self.n) * (self.rho_s / self.R_c) / self.n
        # Viscous diffusion term
        ddt_omega += self.D_vort * Delp2(self.omega) / self.n

        if self.sheath:
            ddt_omega += self.phi * (self.rho_s / self.L_par)
        # other option to set time derivaitve:
        # create a field and set it in the end
        self.omega.ddt(ddt_omega)


# Create an instance
blob2d = Blob2D()
# Start the simulation
blob2d.solve()
```

C.2 Physics based monitors

BOUT++ uses monitors to be called after the system has been evolved for a certain amount of simulated time. The time was fixed to the output time, but in some cases it may be required that some code is called at a different frequency than the frequency at which all the fields are saved. This allows one to define the time interval at which a monitor is called in the physics code. This may be useful if for example the neutrals are update by an external code, e.g. EIRENE, as updating in every evaluation of the time derivative would be expensive. This way the output frequency can be chosen without influencing the physics. Another use case is the PID controller, that is used in the previously presented STORM code. Without a different output frequency for the PID controller, BOUT++ would generate far to large output files, as the PID controller needs to be updated quite often and writing a full dump file every time.

This can also be used to sub-sample the data and measure just one or few points in space, but with a much higher frequency. A synthetic diagnostic can be implemented this way, in order to compare simulation data with probe data, which acquires data at a high temporal resolution.

C.3 BOUT++ for Fedora

BOUT++ has also been packaged for fedora[1]. This increases the availability of BOUT++, as it simplifies getting BOUT++ including the required dependencies. Thus installing BOUT++ is as simple as

```
sudo dnf install bout++-mpich-devel bout++-openmpi-devel
```

[1] `https://getfedora.org`

to get bout++ precompiled for both MPI implementations present in fedora. In combination with the python interface, it allows to implement physics modules or work in general with BOUT++ without having to even have a compiler on the system. The python interface for BOUT++ can be installed with

```
sudo dnf install python3-bout++-mpich python3-bout++-openmpi
```

After that a MPI module needs to be loaded with

```
module load mpi
```

and then `boutcore` can be used from within python.

C.4 Other changes

Besides the above listed changes various other bug fixes, performance improvements, tests, documentation and examples have been contributed to the BOUT++ code base. In total over 250 pull requests have been made and merged, resulting in over 850 changes in terms of git commits, that have been introduced to BOUT++ as part of this PhD.

APPENDIX D

GNU Lesser General Public License

BOUT++ is licensed under the Lesser General Public License version 3 or later (LGPLv3+) license [130, 131]. The GPL license, on which the LGPL is based, is a copyleft license. Copyleft is described on the `https://copyleft.org` website as [163]:

> Copyleft is a strategy of utilizing copyright law to pursue the policy goal of fostering and encouraging the equal and inalienable right to copy, share, modify and improve creative works of authorship. Copyleft (as a general term) describes any method that utilizes the copyright system to achieve the aforementioned goal. Copyleft as a concept is usually implemented in the details of a specific copyright license, such as the GNU General Public License (GPL) and the Creative Commons Attribution Share Alike License. Copyright holders of creative works can

unilaterally choose these licenses for their own works to build communities that collaboratively share and improve those copylefted creative works.

The LGPL (Lesser General Public License) license does not guarantee a strong copyleft, and therefore potentially limits the freedom of researches, however this license provides a compromise between the strong copyleft GPL license and a less free license as the MIT license [164]. Free software is not free as in "free beer", but rather as in "free speech" [165]. It does not limit its use, as it guarantees four essential freedoms (taken from [165]:

- The freedom to run the program as you wish, for any purpose (freedom 0).
- The freedom to study how the program works, and change it so it does your computing as you wish (freedom 1). Access to the source code is a precondition for this.
- The freedom to redistribute copies so you can help your neighbour (freedom 2).
- The freedom to distribute copies of your modified versions to others (freedom 3). By doing this you can give the whole community a chance to benefit from your changes. Access to the source code is a precondition for this.

A strong copyleft license guarantees that future researches can use the software without limitations. The advantage of a strong copyleft over a permissive license is, that derived work is guaranteed to stay free [166]. Especially as most research is publicly funded, the thereby needed and developed software should be in the public domain. Further having free

software is also important, as not being free, can prevent or restrict the changing of the software. This limits the reuse for new use cases, and time has to be wasted to re-write written software. Further advantage such as cost savings and software quality are also good reasons for using free software, but not main advantages of free software [167]. As a compromise for being able to link the BOUT++ library with non-free or non GPL compatible licenses, the LGPL with its weak copyleft was chosen. If BOUT++ is compiled against a library licensed under a strong copyleft license, such as the GPL license, the license of the resulting binary BOUT++ library is GPL, due to the GPL license of the other library. BOUT++ compiles by default against fftw and gettext, both released under the GPL. Unless the support is disabled, the resulting BOUT++ library is also bound by the GPL, rather than the LGPL license.